Astronomy & Astrophysics manuscript no. casagrande˙teff
January 18, 2010
© ESO 2010

arXiv:1001.3142v1 [astro-ph.SR] 18 Jan 2010

An absolutely calibrated $T_{\rm eff}$ scale from the Infrared Flux Method

Dwarfs and subgiants

L. Casagrande[1], I. Ramírez[1], J. Meléndez[2], M. Bessell[3], and M. Asplund[1]

[1] Max Planck Institute for Astrophysics, Postfach 1317, 85741 Garching, Germany
[2] Centro de Astrofísica da Universidade do Porto, Rua das Estrelas 4150-762 Porto, Portugal
[3] Research School of Astronomy and Astrophysics, Mount Stromlo Observatory, Cotter Rd, ACT 2611, Australia

Received; accepted

ABSTRACT

Various effective temperature scales have been proposed over the years. Despite much work and the high internal precision usually achieved, systematic differences of order 100 K (or more) among various scales are still present. We present an investigation based on the Infrared Flux Method aimed at assessing the source of such discrepancies and pin down their origin. We break the impasse among different scales by using a large set of solar twins, stars which are spectroscopically and photometrically identical to the Sun, to set the absolute zero point of the effective temperature scale to within few degrees. Our newly calibrated, accurate and precise temperature scale applies to dwarfs and subgiants, from super-solar metallicities to the most metal-poor stars currently known. At solar metallicities our results validate spectroscopic effective temperature scales, whereas for [Fe/H] $\lesssim -2.5$ our temperatures are roughly 100 K hotter than those determined from model fits to the Balmer lines and 200 K hotter than those obtained from the excitation equilibrium of Fe lines. Empirical bolometric corrections and useful relations linking photometric indices to effective temperatures and angular diameters have been derived. Our results take full advantage of the high accuracy reached in absolute calibration in recent years and are further validated by interferometric angular diameters and space based spectrophotometry over a wide range of effective temperatures and metallicities.

Key words. Stars: fundamental parameters – Stars: abundances – Stars: atmospheres – Infrared: stars – Techniques: photometric

1. Introduction

The determination of effective temperatures ($T_{\rm eff}$) in F, G and K type stars has a long and notable history. Because of their long lifetimes these stars retain in their atmospheres a fossil record of the chemical elements in the interstellar medium at the time of their formation. The stellar effective temperature is of paramount importance for reliable abundance analyses and thus for improving our understanding of Galactic chemical evolution.

Stellar abundances are now routinely derived from high resolution spectra, model atmospheres, and spectrum synthesis. While each of these ingredients have their own issues regarding systematic uncertainties, the dominant source of error is in many cases the adopted $T_{\rm eff}$ of the star. Several indirect methods of $T_{\rm eff}$ determination have been devised to avoid the complications introduced by the measurement of stellar angular diameters, which are necessary to derive $T_{\rm eff}$ from basic principles (e.g. Hanbury Brown et al. 1974; van Belle & von Braun 2009). Thus, most published values of $T_{\rm eff}$ are model-dependent or based on empirical calibrations that are not free from systematics themselves.

It is therefore not surprising to find discrepancies among published $T_{\rm eff}$ values. The ionization and excitation balance of iron lines in a 1D LTE analysis is routinely used to derive effective temperatures as well as $\log g$ and [Fe/H]. While for a sample of stars with similar properties this method can yield highly precise relative physical parameters (Meléndez et al. 2009a; Ramírez et al. 2009, see Section 3 for its use on solar twins), non-LTE effects and departures from homogeneity can seriously undermine effective temperature determinations, especially in metal-poor stars (e.g. Asplund 2005). Similarly, the line-depth ratio technique has high internal precision, claiming to resolve temperature differences of order 10 K (e.g. Gray & Johanson 1991; Gray 1994; Kovtyukh et al. 2003) but it is not entirely model independent (e.g. Caccin et al. 2002; Biazzo et al. 2007) and the uncertainty on its zero point can be considerably large. Another popular method for deriving $T_{\rm eff}$ in late-type stars is provided by the study of the hydrogen Balmer lines, in particular Hα and Hβ (e.g. Nissen et al. 2007; Fuhrmann 2008). For H lines uncertainties related to observations and line broadening (Barklem et al. 2002), non-LTE (Barklem 2007) and granulation effects (Asplund 2005; Ludwig et al. 2009; Pereira et al. 2009) all influence the estimation of effective temperatures.

In such a scenario, an almost model independent and elegant technique for determining effective temperatures was introduced in the late 70's by D. E. Blackwell and collaborators (Blackwell & Shallis 1977; Blackwell et al. 1979, 1980) under the name of InfraRed Flux Method (hereafter IRFM). Since then, a number of authors have applied the IRFM to determine effective temperatures in stars with different spectral types and metallicities (e.g. Bell & Gustafsson 1989; Alonso et al. 1996a; Ramírez & Meléndez 2005a; Casagrande et al. 2006; González Hernández & Bonifacio 2009). The main ingredient of the IRFM is infrared photometry, with the homogeneous and all–sky coverage provided by 2MASS being the *de facto* choice nowadays. As such, the IRFM can now be readily applied to many stars, making it ideal to determine colour–temperature–metallicity relations spanning a wide range of parameters. The effective temperatures determined via IRFM are often regarded as a standard benchmark for other techniques. Whilst they have

high internal accuracy and are essentially free from non-LTE and granulation effects (Asplund & García Pérez 2001; Casagrande 2009, Ramirez et al. in prep.), the reddening and absolute flux calibration adopted in such a technique can easily introduce a systematic error as large as 100 K (Casagrande et al. 2006).

The effective temperatures of dwarfs and subgiants are still heavily debated with various $T_{\rm eff}$ scales behaving very differently depending on colours and metallicities. One of the most critical discrepancies occur at the metal-poor end, for [Fe/H] $\lesssim -2.5$. In their work on the determination of effective temperatures via IRFM, Ramírez & Meléndez (2005a) found temperatures significantly hotter than those previously published, in particular those determined using the excitation equilibrium method. Differences up to 500 K for the hottest ($T_{\rm eff} \simeq 6500$ K) most metal-poor ([Fe/H] $\lesssim -3.0$) stars were reported (e.g., Meléndez & Ramírez 2004; Meléndez et al. 2006b). In this regime, the recent IRFM investigation by González Hernández & Bonifacio (2009) still supports a temperature scale significantly hotter than excitation equilibrium and Balmer lines, but $\sim$ 90 K cooler than Ramírez & Meléndez (2005a).

The abundance pattern measured in metal-poor stars is important for our quest to understand Galactic chemical evolution and Big Bang nucleosynthesis: two notable examples are the oxygen abundance and the lithium trend with metallicity, both of which crucially depend on the adopted $T_{\rm eff}$ scale. For example, a change of +100 K in $T_{\rm eff}$ would decrease the [O/Fe] ratio in turn-off metal-poor stars by $\sim$0.08 dex when using the OI triplet and FeII lines (Meléndez et al. 2006a), while the same change in $T_{\rm eff}$ would increase the Li abundance by $\sim$ 0.07 dex (e.g. Meléndez & Ramírez 2004; Meléndez et al. 2009c,b).

At higher metallicities, which encompass most of the stars in the solar neighbourhood, the situation is also uncertain, with spectroscopic effective temperatures in rough agreement with the IRFM scale of Casagrande et al. (2006). The latter is then about 100 K hotter than the IRFM temperatures of Ramírez & Meléndez (2005b) whilst the recent implementation of González Hernández & Bonifacio (2009) falls in between these two extremes. These differences are somewhat puzzling considering that all recent works on the IRFM have used 2MASS photometry. Effective temperature calibrations are also crucial in the context of deriving reliable colours for theoretical stellar models, which apart from few notable exceptions (e.g. VandenBerg & Clem 2003) have to resort entirely to theoretical flux libraries.

The aim of this work is to uncover the reason(s) behind such a confusing scenario and provide a solution to different IRFM effective temperature scales currently available in literature. As we discuss throughout the paper, this ambitious task is accomplished by using solar twins which allow us to set the absolute zero point of the $T_{\rm eff}$ scale. This result is further validated using interferometric angular diameters and space-based spectrophotometry.

The paper is organized as follows. In Section 2 we compare the results obtained from different authors, focusing in particular on two independent implementations of the IRFM (Ramírez & Meléndez 2005a; Casagrande et al. 2006) when the same input data are used. This approach allows us to precisely identify where different $T_{\rm eff}$ scales originate from. A cure to such an impasse is then provided in Section 3. The validation of our results, together with the new both precise and accurate effective temperature scale are presented in Section 4 to 6. We finally conclude in Section 7.

2. Comparing different versions

In this paper we use an updated version the IRFM implementation described in Casagrande et al. (2006) to nail down the reasons behind different $T_{\rm eff}$ scales. Our implementation works in the 2MASS system and fully exploits its high internal consistency thus making it well suited to the purpose of the present investigation. The core of the present study is to carry out a detailed comparison with the Ramírez & Meléndez (2005a) implementation when the same input data are used. For the sake of precision, notice that hereafter, when we refer to a $T_{\rm eff}$ determined by Ramírez & Meléndez (2005a) we are referring to the effective temperatures determined using that implementation and not the original values given in that paper. This is because of the updated (and more consistent) input data used here and also because some of the stars presented in this work do not have IRFM $T_{\rm eff}$ values published yet. In fact, in order to reveal trends with metallicity and/or effective temperature, our sample is specifically built to cover as wide a range as possible in those parameters (Figure 1).

2.1. Input sample

The main ingredient of the IRFM is optical and infrared photometry. The technique depends very mildly on other stellar parameters, such as metallicity and surface gravity, which are needed to interpolate on a grid of model atmospheres (see Section 2.2). Below we present the papers from which we gathered [Fe/H] and $\log g$ for all our stars and we also give references to the photometric sources.

The metal-rich dwarfs come from Casagrande et al. (2006) who also provide homogeneous and accurate $BV(RI)_C$ photometry while additional metal-rich dwarfs and subgiants are from Ramírez & Meléndez (2005a). We complement the sample with a number of moderately metal-poor stars from the study of Fabbian et al. (2009) and metal-poor turn off stars from Hosford et al. (2009). To investigate the metal-poor end of the $T_{\rm eff}$ scale in more detail, stars with reliable input data from Ramírez & Meléndez (2005a), Bonifacio et al. (2007) and Aoki et al. (2009) were added. Finally, to explore for the first time the hyper-metal-poor regime via IRFM the subgiants HE0233-0343 ([Fe/H] $\lesssim -4$ García Pérez et al. 2008) and HE1327-2326 ([Fe/H] ≤ -5 Frebel et al. 2005; Aoki et al. 2006; Frebel et al. 2008; Korn et al. 2009) were included.

New $UBV(RI)_C$ photometric observations for some of the metal-poor stars in the aforementioned papers were conducted by Shobbrook & Bessell (1999; private communication) and are given in Table 1. For the remaining stars, optical Johnson-Cousins photometry was taken either from Beers et al. (2007) or the General Catalogue of Photometric Data (Mermilliod et al. 1997).

Infrared JHK_S photometry for the entire sample is available from the 2MASS catalogue (Skrutskie et al. 2006) which also includes the uncertainty for each observed magnitude ("j_", "h_" and "k_msigcom"). The infrared median total photometric error of our sample is 0.07 mag. (i.e. "j_"+"h_"+"k_msigcom"= 0.07) and never exceeds 0.14 mag. Such an accuracy in the infrared photometry implies a mean (maximum) internal error in $T_{\rm eff}$ of 25 K (50 K). Notice that the effective internal accuracy is slightly worse because of additional uncertainties stemming from the optical photometry, [Fe/H] and $\log g$. Altogether our final sample

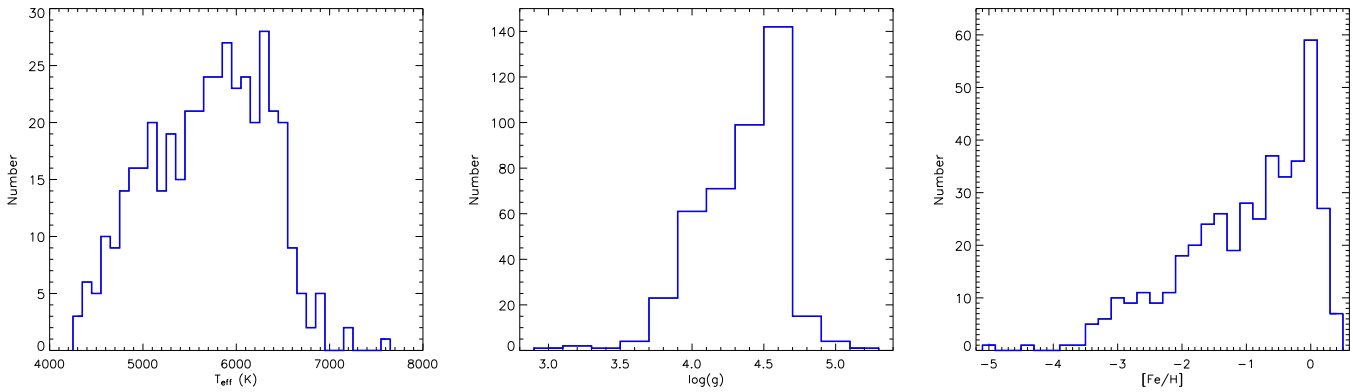

Fig. 1. Distribution of $T_{\rm eff}$, $\log g$ and [Fe/H] for the 423 stars in our sample.

Table 1. New Johnson-Cousins photoelectric photometry obtained for some of the metal-poor stars in the sample. Each measurement comprises an average of 4 observations per star. The rms of individual observations are 0.02 for the V magnitude, 0.015 for the U-B colour and 0.008 mags for B-V, V-R, R-I, V-I colours.

Name	U	B	V	R_C	I_C
HD3567	9.556	9.695	9.240	8.941	8.631
HD16031	10.004	10.197	9.770	9.484	9.184
HD19445	8.207	8.503	8.026	7.737	7.394
HD34328	9.683	9.903	9.416	9.106	8.773
HD45282	8.659	8.672	8.010	7.610	7.196
HD59392	10.048	10.217	9.761	9.457	9.142
HD64090	8.762	8.951	8.295	7.935	7.536
HD64606	8.277	8.140	7.412	6.994	6.561
HD74000	9.880	10.071	9.656	9.381	9.080
HD84937	8.485	8.702	8.306	8.047	7.759
HD94028	8.421	8.640	8.202	7.917	7.585
HD102200	9.009	9.189	8.739	8.449	8.141
HD106038	10.431	10.627	10.153	9.857	9.529
HD108177	9.874	10.082	9.647	9.362	9.052
HD110621	10.230	10.385	9.932	9.628	9.313
HD114762	7.738	7.833	7.283	6.967	6.629
HD116064	9.099	9.282	8.833	8.520	8.189
HD122196	9.055	9.212	8.753	8.444	8.112
HD132475	8.983	9.100	8.563	8.216	7.855
HD134169	8.115	8.193	7.663	7.342	7.011
HD134439	10.033	9.881	9.118	8.661	8.220
HD140283	7.502	7.692	7.205	6.876	6.522
HD160617	9.014	9.188	8.740	8.431	8.108
HD163810	10.185	10.272	9.660	9.280	8.897
HD179626	9.601	9.710	9.188	8.849	8.502
HD181743	9.911	10.140	9.683	9.375	9.062
HD188510	9.303	9.452	8.851	8.486	8.100
HD189558	8.214	8.299	7.740	7.392	7.034
HD193901	9.049	9.183	8.644	8.307	7.964
HD194598	8.666	8.844	8.356	8.055	7.739
HD199289	8.660	8.803	8.287	7.972	7.643
HD201891	7.740	7.908	7.390	7.081	6.737
HD213657	9.869	10.063	9.646	9.368	9.068
HD215801	10.272	10.471	10.038	9.732	9.418
HD219617	8.425	8.621	8.153	7.845	7.525
HD284248	9.407	9.650	9.208	8.927	8.608
HD298986	10.316	10.506	10.062	9.774	9.470
BD+17 4708	9.718	9.922	9.476	9.183	8.854
BD+02 3375	10.174	10.414	9.944	9.635	9.297
BD-04 3208	10.203	10.375	9.977	9.709	9.417
BD-13 3442	10.529	10.655	10.266	9.994	9.704
CD-30 18140	10.155	10.365	9.946	9.663	9.353
CD-33 3337	9.436	9.581	9.109	8.814	8.490

consists of 423 stars: all have $BVJHK_S$ photometry while more than half have also $(RI)_C$ magnitudes available[1].

Proper reddening corrections are crucial to determine $T_{\rm eff}$ via IRFM. We have tested that 0.01 mag. in $E(B-V)$ translates into an IRFM effective temperature roughly 50 K hotter. Reddening is usually zero for stars lying within the local bubble $\lesssim$ 70 pc from the Sun (e.g. Leroy 1993; Lallement et al. 2003) and so we have adopted $E(B-V) = 0$ for all stars having *Hipparcos* parallaxes (van Leeuwen 2007) and satisfying this requirement on the distance. For the remaining stars we updated the reddening corrections in Ramírez & Meléndez (2005a) based on various extinction maps and, in particular for metal-poor stars when archive high resolution spectra were available, using interstellar NaD absorption lines Meléndez et al. (2009b). In broad-band photometry the definition of the effective wavelength of a filter ($\lambda_{\rm eff}$) shifts with the colour of the star (e.g. Bessell et al. 1998; Casagrande et al. 2006). Therefore a given $E(B-V)$ colour excess must be scaled according to the intrinsic colour of the source under investigation. From the reddening $E(B-V)$, we computed the extinction in each band adopting the reddening law of O'Donnell (1994) for the optical and Cardelli et al. (1989) for the infrared, using the improved estimation of the stellar intrinsic flux obtained at each iteration to bootstrap the computation of the correct $\lambda_{\rm eff}$ in our IRFM code.

2.2. The IRFM: pros and cons

The basic idea of the IRFM is to compare the ratio between the bolometric flux $\mathcal{F}_{Bol}$(Earth) and the infrared monochromatic flux $\mathcal{F}_{\lambda_{IR}}$(Earth), both measured at the top of Earth's atmosphere (the so-called observational R_{obs} factor) to the ratio between the surface bolometric flux ($\sigma T_{\rm eff}^4$) and the surface infrared monochromatic flux $\mathcal{F}_{\lambda_{IR}}(T_{\rm eff}, [{\rm Fe/H}], \log g)$ determined theoretically for any given set of stellar parameters. The latter is called the theoretical R_{theo} factor. For stars hotter than about 4200 K, infrared photometry longward of $\sim 1.2\,\mu$m ensures we are working in the Rayleigh-Jeans part of a stellar spectral energy distribution, a region largely dominated by the continuum which linearly depends on $T_{\rm eff}$ and thus only mildly on model atmospheres (Figure 2). An extension of the technique to cooler effective temperatures using near-infrared photometry is possible, as shown by

[1] Other than being available only for a limited number of stars, we did not use U magnitudes because of the little flux emitted in this region and the high uncertainties related to the absolute calibration and standardization of this passband in both observed and synthetic photometry (e.g. Bessell 2005, and references therein).

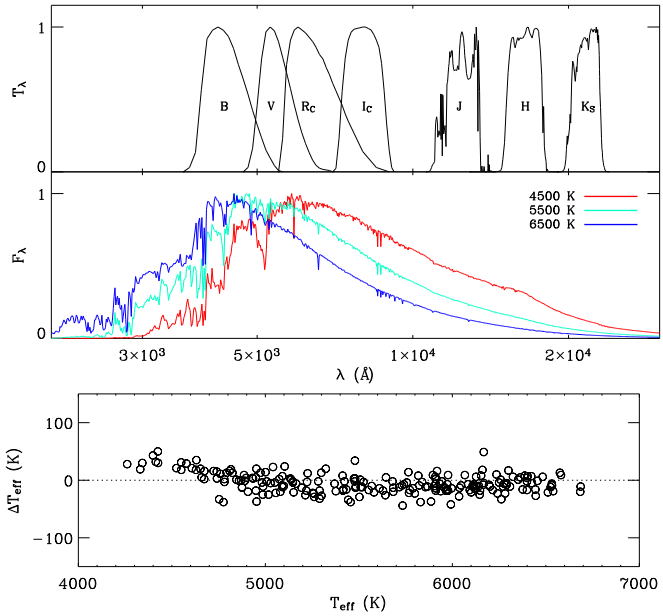

Fig. 2. Top panel: Johnson-Cousins-2MASS filter sets used in this work. Middle panel: synthetic solar metallicity spectra at different $T_{\rm eff}$. For the sake of comparison all curves have been normalized to unit. Bottom panel: difference in effective temperatures with – without using $(RI)_C$ magnitudes to recover the bolometric flux.

Casagrande et al. (2008), but this is outside the purpose of the present paper.

R_{obs} and R_{theo} can be immediately rearranged to determine $T_{\rm eff}$, effectively reducing the entire problem to properly recover $\mathcal{F}_{Bol}$(Earth) and $\mathcal{F}_{\lambda_{IR}}$(Earth). Both quantities are determined from photometric observations, but an iterative procedure is adopted to cope with the mildly model dependent nature of the bolometric correction. In our case we use the fluxes predicted by the Castelli & Kurucz (2004) grid of model atmospheres starting with an initial estimate of the effective temperature and interpolating at the appropriate [Fe/H] and $\log g$ until convergence in $T_{\rm eff}$ is reached within 1 K. By doing so, we also obtain a synthetic spectrum tailored to the effective temperature empirically determined via IRFM.

Though we interpolate at the proper [Fe/H] and $\log g$ of each star, the dependence of the technique on such parameters is minor (e.g. Ramírez & Meléndez 2005a; Casagrande et al. 2006). This feature makes the IRFM superior to any spectroscopic methods to determine $T_{\rm eff}$ –provided the reddening is accurately known– since in the latter the effects of $T_{\rm eff}$, $\log g$ and [Fe/H] are usually strongly coupled and the model dependence is much more important.

The errors are estimated using realistic observational uncertainties in a Monte Carlo simulation plus the systematics arising from the adopted absolute calibration, as described in Casagrande et al. (2006). With the improved absolute calibration used in this paper, systematics amount to 15 K in $T_{\rm eff}$ and 0.3% in bolometric flux (Section 3.2). For stars approximately cooler than 5000 K, $(RI)_C$ photometry is crucial to properly compute the bolometric flux. This can be appreciated in the lower panel of Figure 2: below this temperature a trend appears using $BVJHK_S$ magnitudes only. Missing the peak of the energy distribution clearly leads one to underestimate the bolometric flux thus returning cooler effective temperatures. We have linearly fitted the trend below 5000 K to remove such differences in both $T_{\rm eff}$ and $\mathcal{F}_{Bol}$ when $(RI)_C$ photometry was not available. For $T_{\rm eff} > 5000$ K no obvious trend appears: constant offsets of merely 7 K in $T_{\rm eff}$ and 0.15% in bolometric flux have been found, consistent with the effect that the absolute calibration in $(RI)_C$ can introduce. For the sake of homogenizing the stellar parameters derived in this work, also these small offsets have been corrected for stars with no $(RI)_C$ photometry.

The effective temperature can be determined from any infrared photometric band, in our case JHK_S from 2MASS. Ideally all bands should return the same $T_{\rm eff}$, but photometric errors and zero point uncertainties in the absolute calibration of each band introduce random plus systematic differences. In the case of 2MASS, those amount to few tens of K as we show later.

The magnitude in a given band ζ is converted into a physical flux (i.e. erg cm^{-2} s^{-1} Å^{-1}) via

$$\mathcal{F}_\zeta(\text{Earth}) = \mathcal{F}_\zeta^{\rm std}(\text{Earth})10^{-0.4(m_\zeta - m_\zeta^{\rm std})} \quad (1)$$

which depends on the zero point ($m_\zeta^{\rm std}$) and the absolute flux calibration ($\mathcal{F}_\zeta^{\rm std}$) of the standard star defining the photometric system under use[2].

Most of the photometric systems, including Johnson-Cousins and 2MASS, use Vega as the zero point standard. Vega's flux and magnitudes in different bands have been notoriously difficult to measure with sufficient accuracy (e.g. Gray 2007, and references therein). The problem is only apparently resolved when resorting to R_{obs}: in the ideal case of a unique template spectrum for Vega the choice of its absolute calibration would cancel out in the ratio. In practice, the situation is far from this since the pole-on and rapidly rotating nature of this star imposes the use of a composite absolute calibrated spectrum for different wavelength regions (e.g. Casagrande et al. 2006, and references therein). Such complication does not disqualify Vega as a spectrophotometric standard, but it makes its use more problematic. From Eq. (1) it can be immediately noticed that a change of 0.01 mag. corresponds to a change of about 1% in flux. Since it is possible to interchangeably operate on both zero points and fluxes, for the sake of our discussion it is their composite effect that must be considered, though in the following we shall usually refer to fluxes.

Recently, HST spectrophotometry for Vega has provided a unique calibrated spectrum extending from 3200 to 10000 Å with 1 – 2% accuracy (Bohlin 2007). In the infrared, once the zero points newly determined from Maíz-Apellániz (2007) are used, this result is also in broad agreement with the 2MASS absolute calibration provided by Cohen et al. (2003). Rieke et al. (2008) have also recently reviewed the absolute physical calibration in the infrared, substantially validating the accuracy of 2MASS: their recommended 2% increase of flux in K_S band is in fact compensated by their newly determined zero point for Vega, thus implying an effective change in the overall K_S calibration of only 0.2%. We have tested all these different possibilities; with respect to the HST and 2MASS calibration adopted in Casagrande et al. (2006) the derived $T_{\rm eff}$ are affected at most by 20 K. Such difference is thus within the aforementioned global 2% uncertainty which allows for systematics in $T_{\rm eff}$ of order

[2] We point out that Eq. (1) holds exactly for a heterochromatic measurement, while for computing a monochromatic flux from the observed photometry, an additional correction (the so called q-factor) must be introduced to account for the fact that the zero point of the photometric system is defined by a standard star, which usually has a different spectral energy distribution across the filter window with respect to the problem star (e.g. Alonso et al. 1996a; Casagrande et al. 2006).

40 K. Our zero points and absolute fluxes are essentially identical to those adopted in Casagrande et al. (2006) except for a small fine-tuning which will be further discussed in Section 3.

Despite the recent increasing concordance in establishing absolute fluxes, the uncertainties which have historically plagued Vega are crucial in the context of understanding the effective temperatures determined via IRFM by various authors. We have tested that uncorrelated changes of a few percent in the absolute calibration of optical bands (needed to recover the bolometric flux) can introduce spurious trends with $T_{\rm eff}$ and [Fe/H] up to few tens of K. Similar changes in the absolute calibration of infrared bands have only minor impact on the bolometric flux, but as already mentioned, $T_{\rm eff}$ is very sensitive to them since they enter explicitly in the definition of R_{obs}: increasing all of them by 2% translates into a decrease of approximately 40 K in $T_{\rm eff}$. Considering that differences of few percent in the adopted zero points and fluxes are commonly present among various IRFM implementations, it can be immediately realized that they are responsible for systematic differences among various authors.

2.3. Alonso et al. (1996) scale

One of the most extensive applications of the IRFM to Pop I and II dwarfs is that of Alonso et al. (1996a), which was based on the infrared photometry collected at the TCS (Telescopio Carlos Sanchez, Alonso et al. 1994b) and absolutely calibrated using a semi-empirical approach relying on (mostly) giant stars with measured angular diameters to determine the reference absolute fluxes (Alonso et al. 1994a). The comparison between our $T_{\rm eff}$ and those by Alonso et al. (1996a) is shown in Figure 3. Despite the scatter arising from the different input data we used, there is a clear offset with our scale being systematically hotter. No obvious trends in $T_{\rm eff}$ and [Fe/H] appear. This offset is easily explained in terms of the absolute calibration underlying the two different photometric systems adopted. This involves the transformation from TCS to 2MASS system (see also the discussion in Casagrande et al. 2006), which could in principle introduce additional noise (see Section 2.4). A more detailed description of the absolute calibration (and angular diameters) employed by Alonso and a comparison with our own is presented in Appendix A.

An area of particular interest is the determination of effective temperatures in very metal-poor, turn-off stars. We have tested the effect of using the new Castelli & Kurucz (2004) model atmospheres in the IRFM instead of the Kurucz (1993) adopted by Alonso et al. (1996a). The IRFM is known to be little model dependent (e.g. Asplund & García Pérez 2001; Casagrande 2009) and in fact there are no big differences except at the lowest metallicities, where Castelli & Kurucz (2004) support effective temperatures hotter by $\sim$ 40 K. The reason for such a discrepancy stems from the new models returning higher flux below $\sim$ 4000 Å, a region where the most metal-poor, turn-off stars commence emitting non negligible amounts of energy. Since we do not have UV photometry (and its standardization would be uncertain), we must rely on model atmospheres to determine the flux over this region (Figure 4). The latest model atmosphere calculations show excellent agreement as we checked that nearly identical $T_{\rm eff}$ are obtained when the new MARCS models (Gustafsson et al. 2008) are used instead of those by Castelli & Kurucz (2004) (also Section 5.3.1), but see Edvardsson (2008) for a discussion of the performance of model atmospheres in the blue and ultraviolet.

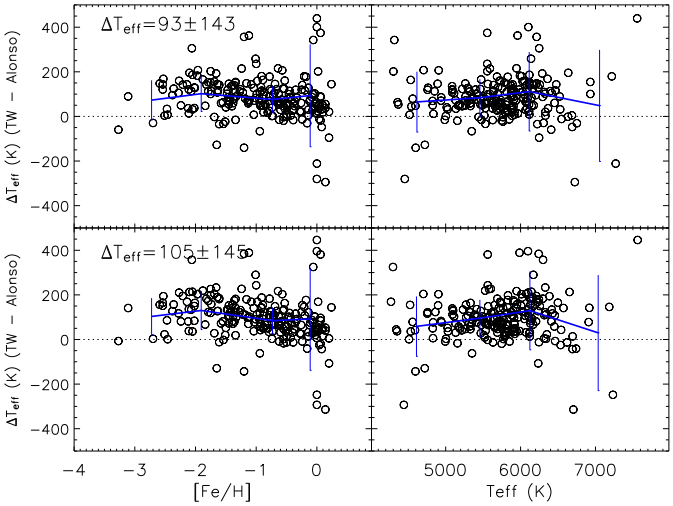

Fig. 3. Difference between the effective temperatures obtained in this work (TW) and those reported in Alonso et al. (1996a) for 220 stars in common. In case of reddening, only stars with values of $E(B-V)$ equal to within 0.02 mag. have been plotted. Thick continuous lines connect the means computed in equally spaced bins of [Fe/H] and $T_{\rm eff}$. Error bars are the standard deviation in each bin. Top panels: when Kurucz (1993) models are used in our version of the IRFM. Bottom panels: when the new Castelli & Kurucz (2004) models are used instead. Below [Fe/H] = −1.5 the new models support $T_{\rm eff}$ hotter by 20 to 40 K.

2.4. Ramírez & Meléndez (2005) scale

A revision of the Alonso et al. (1996a) implementation of the IRFM was carried out by Ramírez & Meléndez (2005a) based on the TCS (for the computation of R_{theo}) and Johnson's (for the computation of the bolometric fluxes) *JHK* photometric systems (Alonso et al. 1994b; Bessell & Brett 1988). Here we replicate the $T_{\rm eff}$ determination by Ramírez & Meléndez (2005a) for comparison purposes. When running their implementation, we transformed the 2MASS photometry into TCS using their equations. However, when comparing the transformed and original *JHK* values for these stars we found zero point differences at the level of 0.01 magnitudes: these offsets are within the photometric uncertainties and smaller than the scatter in the fits leading to the transformation equations, but they introduce changes in the derived $T_{\rm eff}$ values up to few tens of K (see Section 2.2). Therefore we took those into account to precisely transform 2MASS data into the TCS system.

The Ramírez & Meléndez (2005a) bolometric fluxes were determined using the K-band bolometric correction calibration by Alonso et al. (1995), which depends only on the Johnson $(V-K)$ colour index and the stellar metallicity.[3] This calibration is internally accurate within its ranges of applicability and one would expect that extrapolations slightly outside these ranges would still provide reliable results at low metallicities. This approach was followed by Ramírez & Meléndez (2005a). With regards to the absolute flux calibration in the infrared, Ramírez & Meléndez (2005a) adopted that of Alonso et al. (1994a), which is valid for TCS *JHK* photometry while we use

[3] We have also tested that in the context of computing bolometric fluxes for this work, the updated J. Carpenter transformations from 2MASS to Johnson available online at: http://www.astro.caltech.edu/~jmc/2mass/v3/transformations are instead accurate enough and insensitive to small zero point changes.

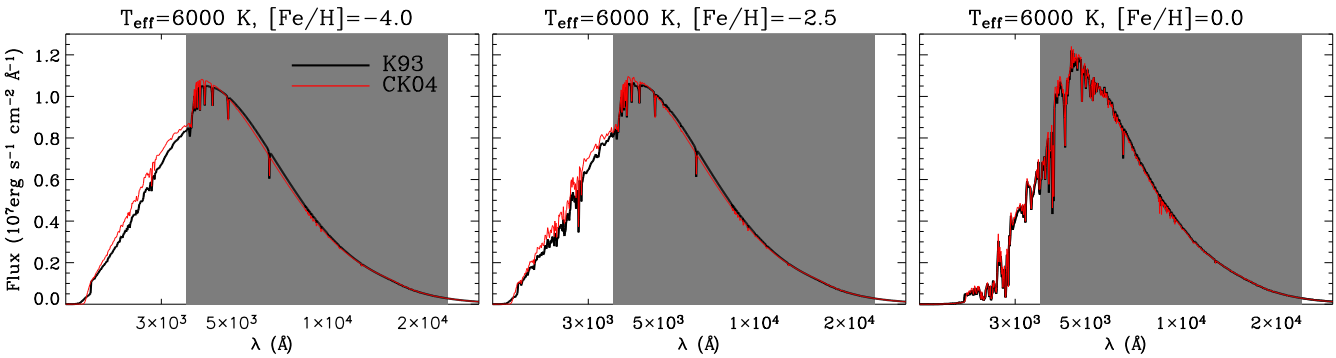

Fig. 4. Comparison between Kurucz (1993) (thick line) and Castelli & Kurucz (2004) (thin line) synthetic spectra at different metallicities for an assumed $\log g = 4.0$. Shaded area is the wavelength region covered by our multiband photometry. The difference in the UV flux gets more prominent when going to more metal-poor stars, but for the sake of the IRFM is entirely negligible at solar metallicity.

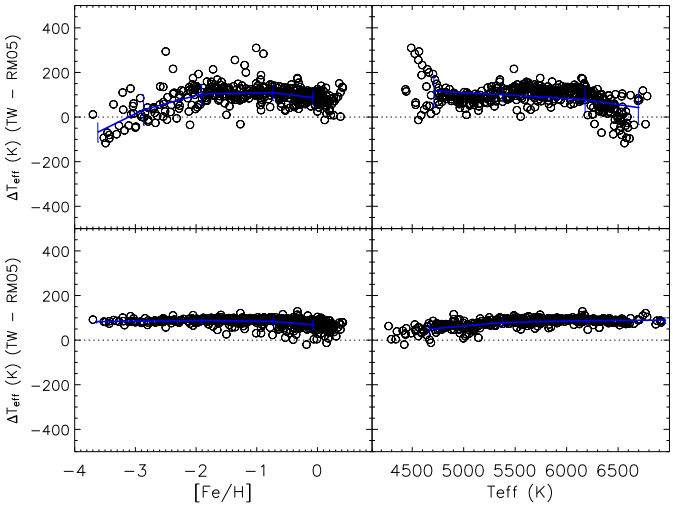

Fig. 5. Top panels: difference between the effective temperatures of this work (TW) and those obtained when the same input data are used in the Ramírez & Meléndez (2005a) implementation (RM05). Bottom panels: as in the top panels but for the Ramírez & Meléndez (2005a) temperatures re-determined using the bolometric fluxes obtained in this work.

an update of Cohen et al. (2003) for the JHK_S 2MASS system (see also Section 3).

The difference between our results and Ramírez & Meléndez (2005a) when the same input data and reddening values are adopted is illustrated in the top panels of Fig. 5. Some of the scatter arise from transforming 2MASS magnitudes into TCS, but clear trends with both with $T_{\rm eff}$ and [Fe/H] are present. For the bulk of the stars with [Fe/H] > -2.0 and $4800 < T_{\rm eff} < 6200$ K a roughly constant offset of about 100 K is observed, our stars being hotter. In the metal-rich regime such an offset is present also for hotter stars ($T_{\rm eff} > 6200$ K), but reduces somewhat for the coolest metal-rich dwarfs, reaching a minimum of about 50 K at $T_{\rm eff} \simeq 4500$ K. A steep trend is seen for moderately metal-poor dwarfs ($-2.0 <$ [Fe/H] < -1.0) below 4800 K, a region with few or no calibrating stars in Alonso et al. (1995). For the warmer, most metal-poor stars in the sample, the differences decrease sharply with increasing $T_{\rm eff}$ and decreasing [Fe/H], quickly becoming negative i.e., Ramírez & Meléndez (2005a) temperatures become warmer, reaching a maximum value of about -100 K at $T_{\rm eff} \simeq 6500$ K and [Fe/H] $\simeq -3.5$.

To investigate the source of these differences, we recalculated the IRFM temperatures of Ramírez & Meléndez (2005a) using our bolometric fluxes instead of the calibration formulae adopted by Ramírez & Meléndez (2005a). This choice is perfectly legitimate, since what is crucial in the IRFM are the infrared fluxes which appear explicitly in the definition of R_{obs}, while $T_{\rm eff}$ depends only mildly on the bolometric flux (Section 2.2). Therefore, adopting our bolometric fluxes is substantially independent of the underlying temperature scale, i.e. the Ramírez & Meléndez (2005a) scale is still recovered despite now using the new bolometric fluxes determined in the present work. The result of this exercise is shown in the bottom panels of Fig. 5. The major trends caused from extrapolating the Alonso et al. (1995) bolometric formulae now disappear with a constant offset $\Delta T_{\rm eff} = 85 \pm 13$ K above 5000 K. The small trend that remains below this temperature corresponds to the threshold where Ramírez & Meléndez (2005a) stop using the J band to determine $T_{\rm eff}$, which in the TCS system usually returns slightly cooler $T_{\rm eff}$ than H and K bands.

From this comparison it is clear that Ramírez & Meléndez (2005a) temperatures for the metal-poor turn-off stars are warmer due to the use of a photometric calibration to derive the bolometric fluxes. In fact, we realize that the Alonso et al. (1995) formula is robust down to [Fe/H] $\simeq -2.5$ and up to $T_{\rm eff} \simeq 6500$ K but only a few calibrating stars more metal-poor or warmer exist in their sample. Ramírez & Meléndez (2005a) use of this formula in regions where the calibration is uncertain (and in some cases outside of the ranges of applicability) has resulted in the very high temperatures of the more metal-poor turn-off stars. The extrapolation is, of course, not a valid procedure, even though one might expect the [Fe/H] dependence of the calibration not to be so important at low metallicity. However, as can be seen from Fig. 4 in Alonso et al. (1995), at these relatively high temperatures, the effect of [Fe/H] is very important and such extrapolations should not be performed.

The difference that remains after adopting consistent bolometric fluxes between this work and Ramírez & Meléndez (2005a) (lower panels of Fig. 5) is mostly due to the use of different infrared absolute flux calibrations. In fact, by lowering the absolute fluxes adopted by Ramírez & Meléndez (2005a) by about 4%, the mean difference reduces to almost zero. We thus conclude that our and Ramírez & Meléndez (2005a) IRFM implementations can be made perfectly compatible if the same input parameters and flux calibration are used.

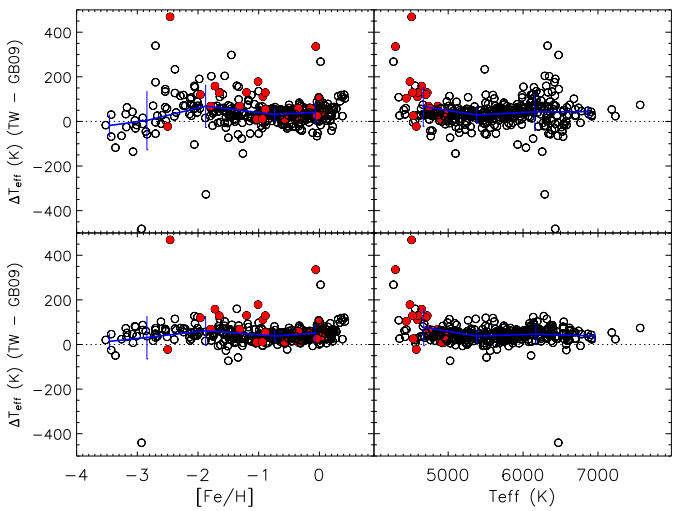

Fig. 6. Top panels: difference between the effective temperatures of this work (TW) and those in González Hernández & Bonifacio (2009) (GB09) for 380 stars in common. Filled circles are stars with $T_{\rm eff} < 5000$ K without $(RI)_C$ photometry in GB09. Bottom panels: as in the top panels, but when the same reddening corrections are used.

2.5. González Hernández & Bonifacio (2009) scale

The most recent work on the IRFM is that by González Hernández & Bonifacio (2009), which is also based on 2MASS photometry. The main difference between theirs and our implementation is the different absolute calibration and zero points adopted for Vega. They based their work on the Castelli & Kurucz (1994) model and McCall (2004) magnitudes instead of the HST (Bohlin & Gilliland 2004; Bohlin 2007) and 2MASS (Cohen et al. 2003) values that we use. Although such differences are within the current observational errors, in the infrared the combined effect of their fluxes and zero points is on average 1.5 – 2.0% higher than ours, implying effective temperatures cooler by 30 – 40 K (see Appendix A). This can be immediately appreciated in Figure 6, which indeed shows a constant offset of this magnitude for stars in common, thus confirming the offset noticed by González Hernández & Bonifacio (2009) for stars in common with Casagrande et al. (2006).

The very steep trend at the lowest metallicities is due to the different reddening corrections we adopt with respect to theirs. When the same $E(B-V)$ values are adopted (bottom panels in Figure 6), the offset remains constant throughout the entire [Fe/H] and $T_{\rm eff}$ range, except for few outliers due to the different input data (mostly optical photometry) adopted. This clearly stresses the importance of proper reddening correction for determining effective temperatures via IRFM in stars outside of the local bubble. For the most metal-poor stars in the sample, we use interstellar NaD lines to achieve higher precision (Section 2.1) while González Hernández & Bonifacio (2009) resorted to reddening maps scaled by the distance and the galactic latitude of the star and scale height of the dust layer. The trend towards cooler effective temperatures that we obtain in this regime thus stem entirely from better reddening corrections. Finally, we suspect that the trend for $T_{\rm eff} < 5000$ K is due to the absence of $(RI)_C$ colours in González Hernández & Bonifacio (2009) (Section 2.2, bottom panel of Figure 2).

3. Resolving different versions

It is clear from the discussion above that we now understand where different $T_{\rm eff}$ scales originate from and the crucial role played by the absolute calibration. Our approach has been to adopt the latest calibration available for each photometric system: currently those are accurate at the 2% level, implying possible systematic uncertainties of order 40 K. Here we want to improve upon this uncertainty using an independent verification of the absolute calibration adopted.

3.1. Solar twins

The use of solar-type stars to calibrate photometric systems has a long and noble history, which relies on taking absolutely calibrated measurements of the Sun and computing synthetic colours to compare with other solar-type stars (e.g. Johnson 1965; Campins et al. 1985; Rieke et al. 2008). This rationale can be extended to other physical properties, namely using the solar effective temperature $T_{\rm eff,\odot} = 5777$ K as the average value for solar-type stars (e.g. Masana et al. 2006). This technique is well established and goes under the name of solar analogs method, but there is some sort of *petitio principii* in the underlying $T_{\rm eff}$ scale adopted and/or the solar colours assumed to select solar analogs in first instance.

A way to break such a degeneracy is provided by solar twins, i.e. stars with spectra indistinguishable from the Sun (Cayrel de Strobel & Bentolila 1989; Porto de Mello & da Silva 1997). Our twins were drawn from an initial sample of about 100 stars broadly selected to be solar like: the identification of the best ones was based on a strictly differential analysis of high-resolution ($R \sim 60000$) and high signal-to-noise ($S/N \gtrsim 150$) spectra with respect to the solar one reflected from an asteroid and observed with the same instrument. Within this initial sample, the selection criterion adopted to identify the best twins did not assume any *a priori* effective temperature or colour, but was based on the measured relative difference in equivalent widths and equivalent widths vs. excitation potential relations with respect to the observed solar reference spectrum and thus entirely model independent (Meléndez et al. 2006a; Meléndez & Ramírez 2007). Since the spectra of the solar twins match so closely the solar one, exceedingly accurate differential spectroscopic analysis with respect to $T_{\rm eff,\odot}$, $[{\rm Fe/H}]_\odot$ and $\log g_\odot$ is possible (Meléndez et al. 2009a; Ramírez et al. 2009).

Ten stars were identified as most closely resembling the Sun and are given in Table 2, including HIP56948, the best solar twin currently known (Meléndez & Ramírez 2007; Takeda & Tajitsu 2009). A crucial requirement for these stars is to have accurate and homogeneous photometry in order to derive reliable $T_{\rm eff}$ via IRFM. While this is possible in the infrared because of 2MASS[4], optical photometry is also important to properly recover the bolometric flux where these stars emit most of their energy. Johnson-Cousins photometry would be the ideal choice, but unfortunately is not available for all these targets. To overcome this limitation, in the optical we used the Tycho2 B_TV_T system which uniformly and precisely covers the entire sky in the magnitude range of our interest (Høg et al. 2000). Notice that we did not transform B_TV_T into BV but instead implemented our IRFM code to work directly on the Tycho2 system. Also, as discussed in Section 2.2 the absence of $(RI)_C$ photometry is not relevant for stars hotter than 5000 K. All twins are closer

[4] In fact, the other well known solar twin 18 Sco (Porto de Mello & da Silva 1997) has saturated 2MASS colours.

than 72 pc, where reddening is expected to be zero or negligible: nearly all of them have Strömgren photometry (Meléndez et al. in prep.) and the Schuster & Nissen (1989) reddening calibration confirms indeed such a conclusion.

3.2. A finely tuned absolute calibration

As for the Johnson-Cousins system, we based the absolute calibration of the Tycho2 system on Vega (Bohlin & Gilliland 2004; Bohlin 2007), adopting the $B_T V_T$ zero points of Maíz-Apellániz (2007) and the corresponding filter transmission curves of Bessell (2000).

The first instance, we determined $T_{\rm eff}$ via IRFM for each of the twins in Table 2: their average effective temperature turned out to be 5782 K, remarkably close to $T_{\rm eff,\odot}$, thus confirming the high accuracy achieved using the HST and 2MASS absolute calibration. Based on Monte Carlo simulations with the photometric errors in Table 2, the uncertainty in $T_{\rm eff}$ determined via IRFM is of order 30 K for single stars. Imposing the mean effective temperature of all solar twins to equal $T_{\rm eff,\odot}$ we estimate the uncertainty on the zero point of our temperature scale to be 15 K based on a bootstrap procedure with one million re-samples. At the same time, for HIP56948 we also recover $T_{\rm eff,\odot}$ within 1σ.

Though the solar twins test confirms the global reliability of the adopted absolute calibration, for all stars in Section 2.1 having Tycho2 photometry and $T_{\rm eff} > 5000$ K we further required each infrared band to return on average the same $T_{\rm eff}$ as the others (Figure 7). By imposing such a consistency we improve upon small systematic trends which could arise when determining effective temperatures in stars with $T_{\rm eff}$ and [Fe/H] very different from our solar twins. This led to a decrease of the absolute calibration by 1.6% in the J band and an increase by 1.5 and 0.3% in the H and K_S bands, respectively (see also Appendix A). In terms of synthetic magnitudes these differences make H and K_S redder by 0.016 and 0.003 and J bluer by 0.017, thus removing almost entirely the infrared colour offsets found by Casagrande et al. (2006) when comparing observed and synthetic photometry. We cannot entirely rule out whether these systematic differences arise from the adopted synthetic library or the absolute calibration, but since the IRFM depends only marginally on model atmospheres and the infrared spectral region is relatively easy to model, we are strongly in favour of the second possibility. From a pragmatic point of view, this improves the consistency in determining $T_{\rm eff}$. Also, such changes are within the 2MASS quoted errors and for the K_S band we remark the agreement with the 0.2% increase found by Rieke et al. (2008) and discussed in Section 2.2. As expected, stars with the best 2MASS pedigree also return better agreement in all bands (full circles in Figure 7). We have also checked that the increasing scatter in Figure 7 is primarily due to photometric errors. We recall that Rieke et al. (2008) found a 2% offset between Read 1 and Read 2 mode in 2MASS[5], though they were not able to derive a universal correction for this effect. All our solar twins have Read 1 mode and the absence of a universal correction suggests that while Read mode 2 can decrease the precision of $T_{\rm eff}$ the overall accuracy of our calibration remains valid.

With the fine-tuning discussed above, the median (mean) effective temperature of our solar twins is 5777 (5779) K. Restricting only to the twins having $T_{\rm eff,\odot}$ within the observational errors, still confirm such conclusion. As a further independent test, we applied our IRFM to the list of solar analogs used by Rieke et al. (2008) and determined their median (mean) $T_{\rm eff}$ to be 5791 (5786) K, thus confirming the reliability of the zero point of our temperature scale, which has an uncertainty of 15 K. Such a value implies possible systematics in the absolute calibration at the 1% level. The systematic error in recovering the bolometric luminosity is however smaller since infrared fluxes enter twice in R_{obs}, thus partly compensating their uncertainty.

The corrections in the infrared absolute calibration discussed here have been used also in determining $T_{\rm eff}$ for stars in Section 2.1. Since for those stars we are using Johnson-Cousins photometry, there could still be small differences arising from the absolute calibration in the optical: for stars in common a mean systematic of 8 K in $T_{\rm eff}$ and 0.15% in bolometric flux was found and corrected.

4. Validating the proposed temperature scale

The IRFM determines $T_{\rm eff}$ in an almost model independent way, primarily recovering the bolometric flux $\mathcal{F}_{Bol}$(Earth) of the star under investigation. From the basic definition linking those two quantities the stellar angular diameter $\theta_{\rm IRFM}$ can be obtained self-consistently and this was actually one of the driving reasons for developing the technique (Blackwell & Shallis 1977). In what follows, we use this information to further validate our results.

4.1. Interferometric angular diameters

An independent test of accuracy for the zero point of our effective temperature scale involves the comparison with the angular diameters measured using interferometric techniques (corrected for limb-darkening, hereafter denoted by $\theta_{\rm LD}$). In our case, angular diameters are a natural consequence of the $T_{\rm eff}$ determination procedure and for each star the $T_{\rm eff}, \mathcal{F}_{Bol}, \theta_{\rm IRFM}$ values are self-consistent, i.e., they represent a unique solution for a given set of input data. We also prefer to compare angular diameters directly (i.e. $\theta_{\rm IRFM}$ vs. $\theta_{\rm LD}$) since the effective temperatures reported in various interferometric works would be more heterogeneous because of the adopted bolometric corrections.

Given the difficulties involved in the measurement of the small angular diameters of dwarfs and subgiants (even the nearest ones have angular diameters below 10 milli-arcseconds), only a relatively small group of such stars has been observed to date for that purpose (see also Appendix A for a discussion of the angular diameters used by Alonso et al. 1994a). We performed a literature search for interferometrically determined angular diameters with precision better than 5 % (which corresponds to an accuracy of 2.5% in effective temperatures, roughly 150 K at solar temperature, assuming no error in the bolometric flux) and found data for 28 stars, 16 of which have $\theta_{\rm LD}$ measured to better than 2 % (Table 3). The efforts made by the interferometry community in the last few years are commendable given that the number of stars with reliable $\theta_{\rm LD}$ has nearly doubled since 2005 (cf. Ramírez & Meléndez 2005a).

Unfortunately, all dwarfs and subgiants with reliable $\theta_{\rm LD}$ are brighter than $V \simeq 6$, implying infrared magnitudes $\lesssim 5$ where 2MASS photometry has large observational errors and starts to saturate[6]. Therefore we cannot apply our IRFM directly on them to get $\theta_{\rm IRFM}$. Instead, we adopt an indirect approach using the photometric $T_{\rm eff}$:colour and $\mathcal{F}_{Bol}$:colour relations presented in Section 6. Using the photometry of our sample stars (i.e. those used in the construction of the calibrations and therefore with $T_{\rm eff}$ directly determined via IRFM), we checked that the zero

[5] This mode indicates which readout is used to derive photometry http://www.ipac.caltech.edu/2mass/releases/allsky/doc/sec3_1b.html

[6] www.ipac.caltech.edu/2mass/releases/allsky/doc/sec2_2.html#pscphotprop

Table 2. Tycho2 and 2MASS photometry for our solar twins sample, together with the spectroscopic parameters and the effective temperatures determined via IRFM. For the latter, the errors are those arising from the photometry alone, not including the 15 K uncertainty in the zero point of our temperature scale. All twins have "A" quality flag and Read 1 mode in all 2MASS bands.

HIP	B_T	σ_B	V_T	σ_V	J	σ_J	H	σ_H	K_S	σ_K	$T_{\rm eff}^{\rm spec}$ ±20 K	$\log g$ ±0.04 dex	[Fe/H] ±0.022 dex	$T_{\rm eff}^{\rm IRFM}$ (K)
30502	9.483	0.019	8.706	0.013	7.474	0.029	7.139	0.029	7.069	0.024	5745	4.47	−0.01	5760 ± 28
36512	8.498	0.015	7.786	0.011	6.517	0.020	6.213	0.027	6.154	0.024	5755	4.53	−0.08	5763 ± 26
41317	8.613	0.015	7.868	0.010	6.610	0.023	6.289	0.038	6.206	0.024	5740	4.49	−0.02	5739 ± 27
44935	9.522	0.021	8.783	0.015	7.548	0.019	7.260	0.034	7.171	0.024	5800	4.41	0.07	5803 ± 30
44997	9.122	0.017	8.378	0.012	7.107	0.021	6.888	0.051	6.764	0.026	5790	4.52	0.03	5791 ± 30
55409	8.793	0.017	8.066	0.011	6.811	0.019	6.493	0.042	6.419	0.021	5760	4.52	−0.01	5758 ± 26
56948	9.462	0.017	8.748	0.012	7.477	0.019	7.202	0.026	7.158	0.018	5782	4.38	0.01	5801 ± 25
64713	10.048	0.029	9.280	0.021	8.086	0.018	7.771	0.026	7.707	0.034	5815	4.52	−0.01	5853 ± 36
77883	9.532	0.023	8.820	0.018	7.476	0.021	7.176	0.038	7.125	0.034	5695	4.39	0.04	5660 ± 35
89650	9.708	0.023	8.996	0.017	7.781	0.029	7.506	0.034	7.431	0.033	5855	4.48	0.02	5864 ± 35

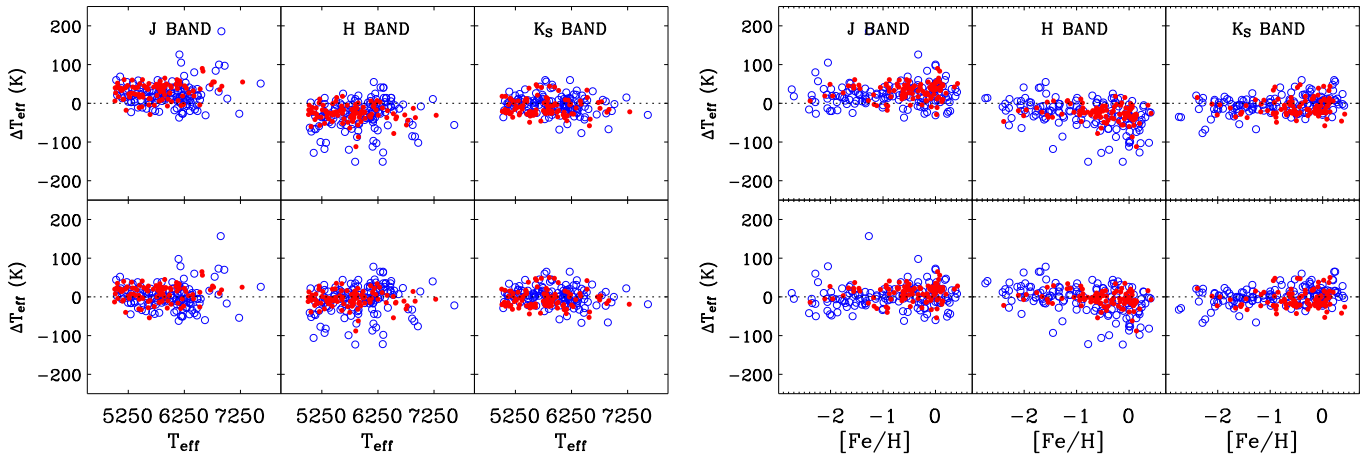

Fig. 7. Top panels: difference between $T_{\rm eff}$ and the effective temperature determined in each infrared band before tuning the absolute calibration. Full circles are stars with quality flag "A", Read 1 mode and total 2MASS photometric errors < 0.07 mag. while open circles are for all other stars. Bottom panels: as in the top panels, but with the adjusted absolute calibration. H band photometry has usually slightly higher error than J and K_S and the final temperature is the weighted average of that obtained in each band.

point of our $T_{\rm eff}$ and $\mathcal{F}_{Bol}$ scales is correctly reproduced by the calibration formulae presented in Section 6, independently of the apparent magnitudes of the stars. Also, for the two stars having HST spectrophotometry (next Section) we checked that our calibration formulae reproduce nearly the same results as directly applying the IRFM. We were careful about propagating all possible sources of random error such as uncertainties in the input photometry, metallicity, and the reliability of the colour calibrations, as quantified by the standard deviation of each polynomial fit (Tables 4 and 5). For most of the stars with reliable $\theta_{\rm LD}$ (i.e. better than 2%), only BV photometry was available, while for the remaining $BV(RI)_C$ was used. Metallicities were adopted from the updated version of the Cayrel de Strobel et al. (2001) [Fe/H] catalog by Meléndez (in prep.), which nearly triples the number of entries in the original catalog.

The comparison of the angular diameters measured interferometrically with those derived using our IRFM colour calibrations is shown in Fig. 8 (see also Table 3). Stars that have $\theta_{\rm LD}$ determined with accuracy better than 2 % are shown with full symbols. Using only the latter, the average difference in angular diameter (IRFM-LD) is −0.62 ± 1.70 % which corresponds to a zero point difference in the effective temperature scale of only +18 ± 50 K at solar temperature. This is also in agreement with the uncertainty on the zero point of our temperature scale discussed in Section 3.2. No obvious trends are seen with [Fe/H] (from about −0.8 to +0.3) or $T_{\rm eff}$ (from 4400 to 6600 K). Note, however, that if we exclude the two coolest stars (from the group of those having errors smaller than 2 %), a small trend is seen with $T_{\rm eff}$. The trend –if real– appears more clearly for early type stars, with $\theta_{\rm IRFM}$ being underestimated (and therefore the IRFM effective temperatures overestimated) with respect to the interferometric measurements. Interferometry resorts on 1D model atmospheres to correct from the measured uniform-disk angular diameter to the physical limb-darkened disk to which we compare with. Interestingly, 3D models predict less center-to-limb variation than 1D models as moving from K to F type stars (Allende Prieto et al. 2002; Bigot et al. 2006). Reduced limb-darkening corrections imply smaller $\theta_{\rm LD}$: the trend discussed above qualitatively fit into this picture. How well our result agrees quantitatively with this picture we leave to future studies.

Interestingly, Ramírez & Meléndez (2005a) made a similar comparison of angular diameters and also found good agreement with their IRFM $T_{\rm eff}$ scale, which is, however, systematically cooler (by ≃ 100 K) than the present one for [Fe/H] ≳ −2 (see also Casagrande 2008). We compared the stars with angular diameters in common between table 4 of Ramírez & Meléndez (2005a, RM05) and the present study (C09, Table 3) and found an average difference (C09-RM05) of 0.1 ± 2.2 % in angular diameters, 3.0 ± 3.0 % in bolometric fluxes and 40 ± 37 K

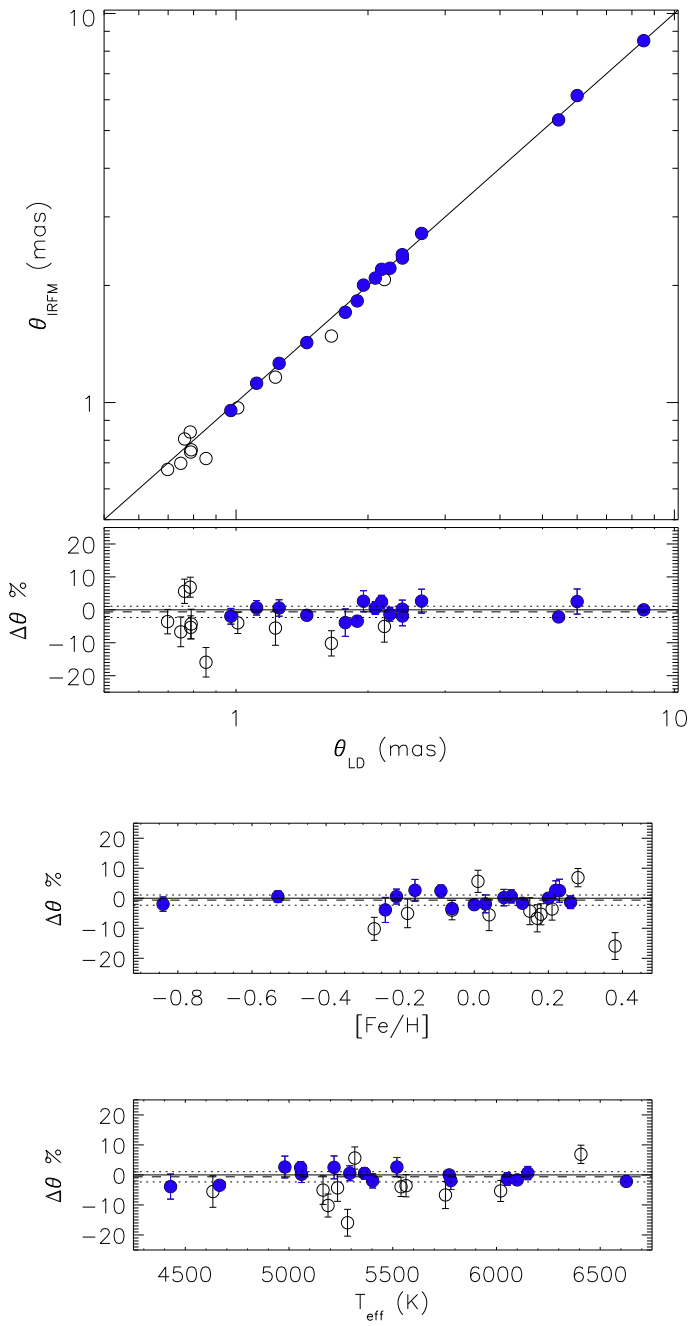

Fig. 8. Top two panels: Comparison of angular diameters measured interferometrically ($\theta_{\rm LD}$) and via our IRFM photometric calibrations ($\theta_{\rm IRFM}$). Full symbols represent stars that have $\theta_{\rm LD}$ measured with accuracy better than 2 %. Bottom two panels: Difference (in %) between $\theta_{\rm LD}$ and $\theta_{\rm IRFM}$ as a function of stellar parameters. Solid lines represent 1-to-1 correspondence, dashed and dotted lines are the average difference and 1-σ error for the full data point, respectively.

in $T_{\rm eff}$. Given the large scatter, these numbers are still consistent with the mean differences in $T_{\rm eff}$ and $\mathcal{F}_{Bol}$ from these two studies (Section 2.4), however, we would expect our diameters to be roughly smaller by 3 %, our fluxes brighter by 1 % and our $T_{\rm eff}$ hotter by 100 K (see also Casagrande et al. 2006). While $\mathcal{F}_{Bol}$ and $T_{\rm eff}$ compensate to give almost exactly the same angular diameters, the 40 K offset might be more representative of the difference with the TCS magnitudes used in Ramírez & Meléndez (2005a) (see the discussion on the small zero point differences to convert 2MASS into TCS presented in Section 2.4). To gauge further insights, we redetermined the temperatures used by Ramírez & Meléndez (2005a) using their colour calibrations for the same $BV(RI)_C$ input data we adopted in this section and found $\Delta T_{\rm eff} = 72 \pm 52$ K. In addition, we adopted our bolometric fluxes lowered by 1 %, which corresponds to the average difference we find for our complete sample. In this case the difference in angular diameters sets to -2.4 ± 2.1 %, much closer to the expected -3 %, offsetting the Ramírez & Meléndez (2005a) scale with respect to interferometric measurements. Since the present work represents an improvement over Ramírez & Meléndez (2005a), in particular the fact that the $T_{\rm eff}, \mathcal{F}_{Bol}, \theta_{\rm IRFM}$ values are a self-consistent and unique solution to each problem star, and given that the number of comparison stars has doubled since 2005 (note also that the $\theta_{\rm LD}$ values of some stars have been re-determined), it is likely that the good agreement found by Ramírez & Meléndez (2005a) was due to a conspiracy of photometric errors which propagated to both $T_{\rm eff}$ and $\mathcal{F}_{Bol}$ determinations and low number statistics. More measurements of stellar angular diameters via interferometry are clearly necessary, and therefore highly encouraged, to better constrain indirectly determined effective temperature scales. However, as this exercise has shown, many critical ingredients enter in the comparison with angular diameters. In particular bolometric corrections and effective temperatures should be determined as self-consistently as possible, also avoiding transformation between photometric systems. It gives us confidence that the zero point uncertainty from solar twins, angular diameters and HST spectrophotometry (next Section) returns in all cases independent and very consistent results.

While the angular diameter comparison does not extend below [Fe/H] $\simeq -1.0$, leaving our results for halo stars "un-tested" in this context, in the next Section we use HST spectrophotometry to gauge further insight on the topic.

4.2. HST spectrophotometry

For each star, we obtain a synthetic spectrum tailored at the effective temperature determined via IRFM (Section 2.2). Since the angular diameter is determined, each synthetic spectrum is absolutely calibrated (i.e. in units of erg cm^{-2} s^{-1} Å^{-1}), and can be used to further test our results. In fact, from F- to early K-type stars, all continuum characteristics approximately longward of the Paschen discontinuity depend almost exclusively on the effective temperature, relatively unaffected by spectral lines and NLTE effects as well as from the treatment of convection.

The CALSPEC[7] library contains composite stellar spectra measured by the STIS (0.3−1.0 μm) and NICMOS (1.0−2.5 μm) instruments on board of the HST and used as fundamental flux standard. Free of any atmospheric contamination the HST thus provides the best possible spectrophotometry to date, with 1−2% accuracy, extending from the far-UV to the near infrared. The absolute flux calibration is tied to the three hot, pure hydrogen white dwarfs, which constitute the HST primary calibrators, normalized to the absolute flux of Vega at 5556 Å (Bohlin 2007). Thus, except for the normalization at 5556 Å the absolute fluxes measured by STIS and NICMOS are entirely independent on possible issues regarding Vega's absolute calibration in the infrared and offer an alternative approach to the 2MASS calibration underlying our temperature scale.

[7] http://www.stsci.edu/hst/observatory/cdbs/calspec.html as of January 2009.

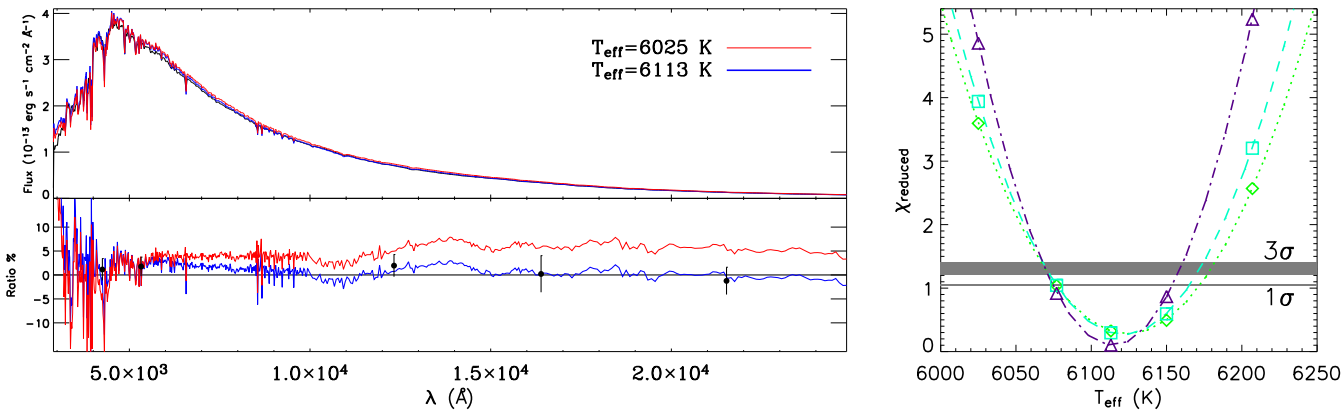

Fig. 9. Left upper panel: comparison between the observed HD209458 CALSPEC spectrum (black line) and the synthetic spectra derived for two different $T_{\rm eff}$, using our preferred absolute calibration (blue line) and increasing the infrared absolute calibration by 5% (red line). Left lower panel: ratio of synthetic to observed spectra. Full circles are the ratio between the fluxes obtained once the Vega calibration is used with the observed magnitudes and the fluxes obtained directly from the convolution of the CALSPEC spectrum with the appropriate filter transmission curve. Error bars take into account uncertainty in the Vega calibration and zero points, as well as in the observed magnitudes. Right panel: reduced χ^2 for various $T_{\rm eff}$ solutions corresponding to different adopted absolute calibrations. Our choice (Section 3.2) always lies very close to the minima obtained fitting a parabola to the data (lines of different style). Different symbols correspond to cut longward of 0.66 μm (diamonds), 0.82 μm (squares) and 1.46 μm (triangles) as explained in the text. The sigma levels have been computed using the incomplete gamma function for the number of degrees of freedom longward of our cuts.

Table 3. Stars with measured interferometric angular diameters.

HD	$\theta_{\rm LD}$ mas	Ref.[a]	$T_{\rm eff}^{\rm IRFM}$ K	[Fe/H] dex	$\theta_{\rm IRFM}$ mas
3651	0.790 ± 0.027	1	5234	0.15	0.756 ± 0.022
6582	0.973 ± 0.009	2	5403	−0.84	0.954 ± 0.021
9826	1.114 ± 0.009	1	6151	0.10	1.121 ± 0.023
10700	2.078 ± 0.031	3	5364	−0.53	2.089 ± 0.026
10780	0.763 ± 0.021	2	5317	0.01	0.806 ± 0.022
19994	0.788 ± 0.026	1	6020	0.18	0.746 ± 0.009
22049	2.148 ± 0.029	3	5056	−0.09	2.200 ± 0.032
23249	2.394 ± 0.029	3	5060	0.08	2.399 ± 0.059
26965	1.650 ± 0.060	3	5188	−0.27	1.482 ± 0.018
61421	5.443 ± 0.030	3	6626	0.00	5.326 ± 0.068
75732	0.854 ± 0.024	1	5282	0.38	0.718 ± 0.025
102870	1.450 ± 0.018	4	6100	0.13	1.426 ± 0.014
117176	1.009 ± 0.024	1	5540	−0.06	0.969 ± 0.021
120136	0.786 ± 0.016	1	6407	0.28	0.840 ± 0.019
121370	2.244 ± 0.019	3	6052	0.26	2.214 ± 0.043
128620	8.511 ± 0.020	3	5772	0.20	8.511 ± 0.079
128621	6.000 ± 0.021	5	5217	0.23	6.151 ± 0.234
131977	1.230 ± 0.030	3	4633	0.04	1.162 ± 0.054
150680	2.397 ± 0.044	3	5780	0.03	2.352 ± 0.055
161797	1.953 ± 0.039	3	5520	0.22	2.004 ± 0.050
185144	1.254 ± 0.012	2	5293	−0.21	1.261 ± 0.029
188512	2.180 ± 0.090	6	5164	−0.18	2.070 ± 0.049
190360	0.698 ± 0.019	1	5564	0.21	0.673 ± 0.017
198149	2.650 ± 0.040	3	4980	−0.16	2.720 ± 0.090
201091	1.775 ± 0.013	3	4429	−0.24	1.706 ± 0.070
209100	1.890 ± 0.020	3	4665	−0.06	1.825 ± 0.021
217014	0.748 ± 0.027	1	5754	0.17	0.698 ± 0.019

[a] 1.– Baines et al. (2008), 2.– Boyajian et al. (2008), 3.– Kervella & Fouqué (2008) (weighted average if more than one measurement was available), 4.– North et al. (2009), 5.– Bigot et al. (2006), 6.– Nordgren et al. (1999).

Two of the CALSPEC targets are late-type main-sequence dwarfs for which accurate photometry, $\log g$ and [Fe/H] are available: the exoplanet host star HD209458 (e.g. Charbonneau et al. 2000) and the fundamental SDSS standard BD +17 4708 (e.g. Fukugita et al. 1996; Smith et al. 2002). For each of these targets we computed $T_{\rm eff}$ and derived the corresponding physical flux using the absolute calibration presented in Section 3.2. For comparison, we also determined the effective temperatures and the corresponding fluxes when changing our adopted infrared absolute calibration by different amounts up to ±5%, which roughly correspond to ∓100 K in $T_{\rm eff}$. The agreement was quantified using χ^2 statistics between the observed ($\mathcal{F}$) and synthetic ($\tilde{\mathcal{F}}$) spectra at various $T_{\rm eff}$

$$\chi^2 = \sum_{\lambda} \frac{\left(\mathcal{F}_\lambda - \tilde{\mathcal{F}}_\lambda\right)^2}{\sigma_\lambda^2} \qquad (2)$$

where σ_λ^2 is the squared sum of the CALSPEC and our random errors, arising primarily from the photometry and to minor extent [Fe/H] and $\log g$. Angular diameters are needed to scale synthetic spectra into physical units: typical 1% internal accuracy in $\theta_{\rm IRFM}$ implies 2% errors in the derived flux. We decided to use random errors only because the purpose of the test is exactly to verify the range of values allowed once the zero point of the temperature scale is assumed.

Also, the tuning of the absolute calibration in the infrared affects the final $T_{\rm eff}$ but it does not modify in any manner the shape of the synthetic spectrum, which entirely depends on the Castelli & Kurucz (2004) grid interpolated at the proper $T_{\rm eff}$, $\log g$ and [Fe/H]. Notice that we are not searching for the synthetic spectrum which best matches the observation, rather we want to test the effective temperature we derive: while adjustments to [Fe/H] and $\log g$ could improve the agreement in the blue and visible part, the continuum characteristics are more sensitive to $T_{\rm eff}$.

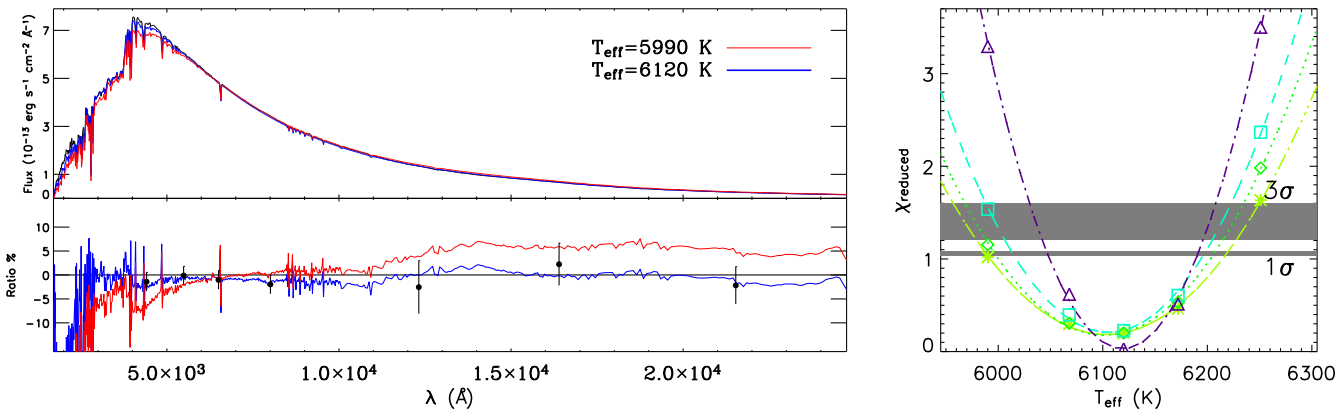

Fig. 10. Same as in figure 9 for BD +17 4708. The synthetic spectra have been reddened by $E(B-V) = 0.01$. Different symbols in the right panel correspond to cut longward of 0.50 μm (asterisks) 0.66 μm (diamonds), 0.82 μm (squares) and 1.46 μm (triangles). The maximum wavelength used for computing the reduced χ^2 has been 2 μm to avoid possible contribution from the cool companion.

4.2.1. HD209458

For this target we adopted the spectroscopic [Fe/H] = 0.03±0.02 and $\log g$ = 4.50 ± 0.04 measured from the high precision HARPS GTO sample (Sousa et al. 2008) and used Tycho2 and 2MASS photometry. We obtain $T_{\rm eff}$ = 6113 ± 49 K, $\mathcal{F}_{Bol}$ = $(2.335\pm0.025)\times10^{-8}$ erg cm^{-2} s^{-1} and $\theta = 0.224\pm0.004$ mas including both random and systematic errors. The latter result is in good agreement with the angular diameters 0.215 ± 0.009 mas obtained using the new *Hipparcos* parallaxes (van Leeuwen 2007) to convert the linear radius measured from exoplanet transit photometry with HST (Brown et al. 2001). Notice that ∼ 100 K cooler effective temperatures would imply values of θ larger by ∼ 3.5% in the IRFM.

The comparison between the observed and synthetic spectra at two different $T_{\rm eff}$ is shown in Figure 9: while they both succeed to capture the main observed features, the continuum of the cooler model is clearly off from the observation. We quantify the agreement between the HST spectrophotometry and the models at various $T_{\rm eff}$ applying χ^2 statistics longward of the Hα line (0.66 μm), the Paschen (0.82 μm) and the Brackett (1.46 μm) discontinuity. These cuts define the beginning of the continuum in a somewhat arbitrary manner, but they all return consistent results thus ensuring that our conclusion is not affected by their choice. The reduced χ^2 is lower than 1 in a roughly ±40 K interval effectively centered on our preferred solution. While reduced $\chi^2 < 1$ tells that the size of the errors is still too large to clearly favour a solution within that range, the large number of points used in the test sets low 1σ and 3σ levels, clearly ruling out solutions different by ±100 K.

4.2.2. BD +17 4708

This star is the only subdwarf with well measured absolute flux, thus making it an important benchmark for testing the temperature scale in the metal-poor regime. We adopt the spectroscopic parameters [Fe/H] = −1.74 ± 0.09, [α/Fe] = 0.4 and $\log g$ = 3.87 ± 0.08 from Ramírez et al. (2006) who also derived $T_{\rm eff}$ = 6141 ± 50 K, $\mathcal{F}_{Bol}$ = (4.89 ± 0.10) × 10^{-9} erg cm^{-2} s^{-1} and θ = 0.1016±0.0023 mas. We corrected for reddening $E(B-V) = 0.01$ the optical (Table 1) and infrared (2MASS) magnitudes, obtaining $T_{\rm eff} = 6120\pm112$ K, $\mathcal{F}_{Bol} = (4.80\pm0.04)\times10^{-9}$ erg cm^{-2} s^{-1} and θ = 0.101 ± 0.003 all in excellent agreement with the aforementioned analysis. Radial velocities show modulation consistent with the presence of a low mass companion which could influence infrared photometry (Latham et al. 1988). The flags associated with 2MASS indicate excellent quality and no artifact nor contamination in any band, pointing toward a negligible effect, if any. Nonetheless, since the percent contribution of a cool companion increases with increasing wavelength, as safety rule we decided not to use K_S in the IRFM though it would change the resulting $T_{\rm eff}$ by only 12 K. For our preferred $T_{\rm eff}$ = 6120 K, shortward of 2 μm there is an outstanding agreement with the CALSPEC observed spectrum, meaning that the solution found represents well the observation at all wavelengths. A moderate increase in the observed with respect to the synthetic flux seems to appear longward of 2 μm, which could be the signature of the cooler companion. On the contrary, cooler solutions overestimate the flux throughout the entire continuum.

Because of the metal-poor nature of this star, the continuum shows up already at bluer wavelengths. We compute the reduced χ^2 in different intervals, starting longward of 0.50 μm: as for the previous star, our solution substantially correspond to the minima of all parabolae, independently of the cut adopted. The random errors associated with this star are larger than in the case of HD209458, giving shallower minima and thus making it more difficult to discriminate between different solutions. However, differences up to ±100 K are clearly disfavoured (Figure 10).

Summarizing, CALSPEC data support our temperature scale which provide the best match to the observed spectrophotometry, in both metal-rich and -poor regimes. While differences larger than ±40 K are ruled out for HD209458, the observational errors for the metal-poor star allow bigger uncertainties. Nonetheless, we have determined the fundamental parameters of both stars with the same procedure and in both cases our solutions are located at the minimum χ^2: we regard such a result as a further indication that our $T_{\rm eff}$ scale is well calibrated over a wide metallicity range.

5. The new effective temperature scale

Our results should be compared with effective temperatures determined employing different methods. First, we focus on large studies which have targeted solar neighbourhood stars, where the vast number of objects imposes the use of fast and efficient techniques, relying on fitting the observed photometry or spectra to their synthetic counterpart. An extensive comparison between the effective temperatures determined from high resolution spectroscopy of solar neighbourhood stars and a version of the IRFM similar to that adopted here has been already carried

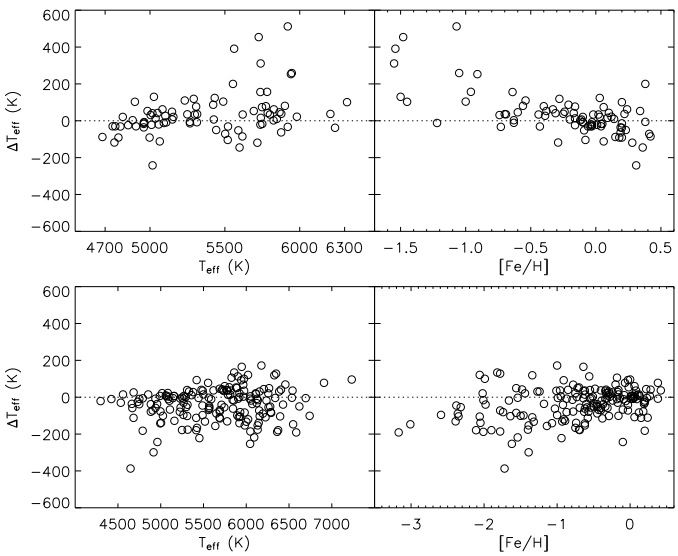

Fig. 11. Upper (lower) panels: comparison between the effective temperatures determined in this work and those obtained by Valenti & Fischer (2005) (Masana et al. 2006).$\Delta T_{\rm eff}$ are this − other works in all panels.

out in Sousa et al. (2008). For metal-poor stars we restrict the comparison to purely spectroscopic effective temperatures; their validation will be crucial for ongoing and future studies of halo stars which are strongly affected by reddening and often lacking photometry.

5.1. Solar Neighbourhood stars

5.1.1. Valenti & Fischer sample

Valenti & Fischer (2005) have presented a uniform catalogue of stellar properties for 1040 nearby F,G and K stars which have been observed by the Keck, Lick and AAT planet search programs. Fitting the observed spectra with synthetic ones, they have obtained effective temperatures, surface gravities and abundances for every star. For 84 objects in common, there is no obvious dependence as a function of $T_{\rm eff}$, except for a drift appearing below 5000 K. However, when $\Delta T_{\rm eff}$ is plotted as function of metallicity the trend becomes clear, with very significant discrepancies at the lowest metallicities (Figure 11).

5.1.2. Masana et al. sample

Masana et al. (2006) have derived stellar effective temperatures and bolometric corrections by fitting V and 2MASS IR photometry. They calibrate their scale by requiring a set of 50 solar analogs drawn from Cayrel de Strobel (1996) to have on average the same temperature as the Sun.

We have 176 stars in common: there is no obvious trend with effective temperatures, and for metallicities around solar there is an overall good agreement. This is not entirely unexpected considering that both studies have been calibrated to the Sun (though with different approaches): considering [Fe/H] > -1 the mean difference (IRFM − Masana) is $\Delta T_{\rm eff} = -21 \pm 6$ K ($\sigma = 71$ K). However, when focusing on metal-poor stars [Fe/H] < -1 there is a significantly increasing scatter and a trend resulting in our $T_{\rm eff}$ being cooler up to ~ 200 K at the lowest metallicities and with a mean difference of -95 ± 22 K ($\sigma = 157$ K).

5.2. Metal-poor, halo stars

5.2.1. Temperatures from fits to hydrogen line profiles

The wings of hydrogen lines are strongly sensitive to the effective temperature of the star and only mildly dependent on the other stellar parameters, other than being unaffected by reddening. Such approach is particularly effective with metal-poor stars, given the lack of severe line blending affecting the hydrogen lines. Thus, provided a proper continuum normalization is applied, which can be non-trivial in some cases (e.g. Barklem et al. 2002), these lines can be used to determine $T_{\rm eff}$. Although significant progress has been made in the last few years, the modeling of hydrogen lines (e.g., the Balmer line profiles) is still quite uncertain (Barklem et al. 2000; Barklem 2007). Nonetheless, the relative $T_{\rm eff}$ values derived in this manner can be very precise (e.g. Nissen et al. 2007).

We remark that there is no such thing as one Balmer line $T_{\rm eff}$ scale, but instead each study depends upon the adopted prescriptions: LTE vs. NLTE, broadening recipes, mixing-length parameter and even the details on how lines are fitted. Also, the thermal structure of the model atmosphere is crucial for the Balmer temperatures: as concerns 1D models, studies relying on OS- instead of ODF-model atmosphere determine hotter $T_{\rm eff}$ (Grupp 2004).

Aware of the complexity of the picture, in the upper panels of Figure 12 our IRFM effective temperatures are compared with those derived from fits to the Balmer lines in two different studies, which we regard as representative of the LTE and NLTE approach, respectively. Circles refer to the comparison with Fabbian et al. (2009) who used the Hβ lines. There is an obvious offset, the IRFM returning $T_{\rm eff}$ hotter by 84 ± 13 K ($\sigma = 66$ K), but the small scatter between these two sets further strengthen the conclusion that both techniques have high internal precision. A similar conclusion holds also from the comparison with the effective temperatures reported in Bergemann (2008, ,and references therein) who used both Hα and Hβ line profiles. In this case the difference (IRFM − H lines) is 21 ± 23 K ($\sigma = 72$ K) with a possible trend suggesting excellent agreement roughly below 6000 K (one star, HD25329 with $T_{\rm eff} = 4785$ K and $\Delta T_{\rm eff} = -15$ K is not shown in the upper left panel of Figure 12).

5.2.2. Excitation equilibrium temperatures

An important number of iron lines are present in the spectra of cool dwarfs, even the metal-poor ones. In an ideal case, the iron abundances determined from each of those lines should be consistent with each other. In practice, however, given an initial set of stellar parameters, the line-by-line abundances show trends with excitation potential (EP) and/or reduced equivalent width. By tuning the stellar parameters, these trends can be eliminated. The EP trend is particularly sensitive to $T_{\rm eff}$, given the strong dependence of the atomic level populations on temperature, and therefore $T_{\rm eff}$ determined by removing the abundance vs. EP trend are often referred to as "excitation equilibrium" temperatures. Because of its nature, this method of $T_{\rm eff}$ determination is highly model-dependent. Not only it does require realistic model atmospheres and spectrum synthesis, but also accurate atomic data and, ideally, a non-LTE treatment of the line formation. The advantage of such method is that it is independent of interstellar reddening and can be applied to stars with uncertain or unavailable photometry.

Recently, Hosford et al. (2009) have determined LTE excitation equilibrium temperatures for a sample of metal-poor stars.

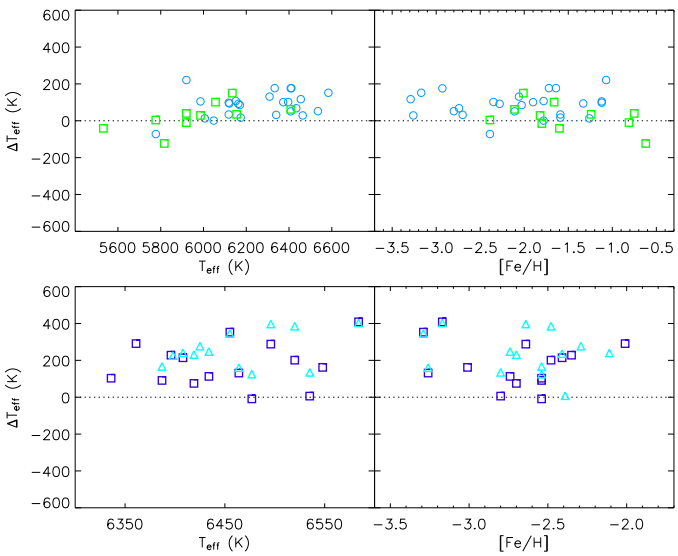

Fig. 12. Upper panels: comparison between the effective temperatures determined in this work and those obtained from the Hβ (Fabbian et al. 2009, circles) and Hα plus Hβ (Bergemann 2008, squares) line profiles. Lower panel: comparison with respect to the excitation equilibrium temperatures determined by Hosford et al. (2009). Two sets of data points are shown because Hosford et al. (2009) temperatures are sensitive to the uncertain $\log g$ values of metal-poor stars; squares (triangles) represents $T_{\rm eff}$ derived assuming the star to be on the main-sequence (subgiant branch). $\Delta T_{\rm eff}$ are this − other works in all panels.

The difference found between their temperatures and ours is illustrated in Figure 12 (HD140283 with $E(B-V) = 0.000$, $T_{\rm eff} = 5777$ K and $\Delta T_{\rm eff} = 8$ K is not shown in the lower left panel). Because the excitation temperatures are somewhat sensitive to $\log g$ and surface gravities of metal-poor stars are difficult to determine due to uncertain/unavailable parallaxes, they provide two sets of $T_{\rm eff}$ values, one assuming the star to be on the main-sequence (MS) and another one assuming the star to be on the subgiant branch (SGB). We remark that for HD140283 parallax and Balmer jump rule out the main-sequence stage; our fit (Mike Bessell) of the MILES fluxes using Munari et al. (2005) spectral library provide $T_{\rm eff} = 5812/5875$ K and $\log g = 3.75$ for $E(B-V) = 0.000/0.017$, respectively.

The IRFM temperatures are significantly hotter than the excitation temperatures by 177 ± 33 K ($\sigma = 122$ K) (for their MS temperatures) and 240 ± 32 K ($\sigma = 116$ K) (SGB). In particular, the large scatter suggests a decreased relative precision when applying excitation equilibrium to very metal-poor stars, so that the further investigation of non-LTE effects will be highly desirable (Hosford et al. in prep.).

5.3. The most metal-poor stars in the Galaxy

Despite theoretical uncertainties on the exact mass range under which the first stars formed, it is likely that the most metal-poor objects currently observed in the Milky Way halo are second generation stars. In case of dwarfs/subgiants, their abundance patterns carry direct information on the first stars ever formed in the Galaxy (e.g. Frebel et al. 2005) and/or on still poorly known long time-scale processes which might take place below the surface or deep into stellar interior (e.g. Venn & Lambert 2008; Korn et al. 2009).

Determining their effective temperature and evolutionary status (i.e. $\log g$) is crucial to derive reliable abundances and constrain different scenarios. At the same time, such a quest is in stark contrast with the many practical limitations associated with hyper-metal-poor stars: parallaxes are not available to help constrain their surface gravities and even when spectra with sufficient resolution and S/N are obtained, the model atmospheres used for the analysis are not yet fully tested at such low metallicities. Rigorous analyses should also take into account 3D (Frebel et al. 2008) and NLTE (Aoki et al. 2006) effects, which are expected to be considerable in this regime. Determining $T_{\rm eff}$ in a way mostly unaffected by the above limitations is not only desirable, but also necessary to put spectroscopic analyses on firmer grounds.

5.3.1. HE1327-2326

For this star the IRFM returns $T_{\rm eff} = 6250 \pm 60$ K in agreement within the errors with the spectroscopic value of 6120 ± 150 K obtained from the NLTE analysis of the Balmer lines (Korn et al. 2009), roughly with an offset of the same order of that discussed in Section 5.2.1. As we already pointed out, the IRFM depends only weakly on the adopted surface gravity: changing it by ±0.5 dex affects $T_{\rm eff}$ by approximately ±25 K. In our case, we used $\log g = 3.7$ as recently determined by Korn et al. (2009). The exact metallicity of HE1327-2326 is also uncertain: although it is well established that its [Fe/H] < -5.0, estimates range from −5.9 to −5.4 depending on the adopted stellar parameters and 1D/3D LTE/NLTE analysis performed (Aoki et al. 2006; Frebel et al. 2008). The IRFM is known to depend very little on the metallicity and we verified this being particularly true (at least in this $T_{\rm eff}$ regime) for the featureless spectra of this hyper-metal-poor star: increasing [Fe/H] by 1 dex in the IRFM affects the derived $T_{\rm eff}$ by less then 10 K. This conclusion supports the suggestion that for hyper-metal-poor stars colour–temperature calibration of normal very-metal-poor stars can be used instead (see discussion in Section 6).

When running the IRFM for this star we used the new grid of MARCS model atmosphere (Gustafsson et al. 2008) which extend down to [Fe/H] $= -5.0$ and this value was used in our implementation. Because of the weak metallicity dependence discussed above, very similar results are obtained if the Castelli & Kurucz (2004) grid (which stops to [M/H] $= -4.0$) is used instead. For the sake of ensuring our results do not depend too much on the adopted spectra library, we also checked that for stars with higher metallicities MARCS or ATLAS9 models return very similar results, with differences usually well within 10 K and at most of order 20 K (see also Casagrande et al. 2006).

We feel the major source of possible systematic error stems from reddening, which is very high for this star. We used $E(B-V) = 0.076$ based on both extinction maps and interstellar absorption lines (Aoki et al. 2006; Beers et al. 2007) but it should be kept in mind that a change of ±0.01mag. in $E(B-V)$ affects $T_{\rm eff}$ by ±50 K.

5.3.2. HE0233-0343

Though the exact metallicity of this star is still uncertain, it seems well secured as having [Fe/H] $\lesssim -4.0$ (García Pérez et al. 2008, García Pérez private communication). Its evolutionary status is also ambiguous, with spectroscopic estimates of $\log g$ varying from 3.5 to 4.5. Also in this case, the exact values of $\log g$ and [Fe/H] are not crucial for the IRFM and we checked

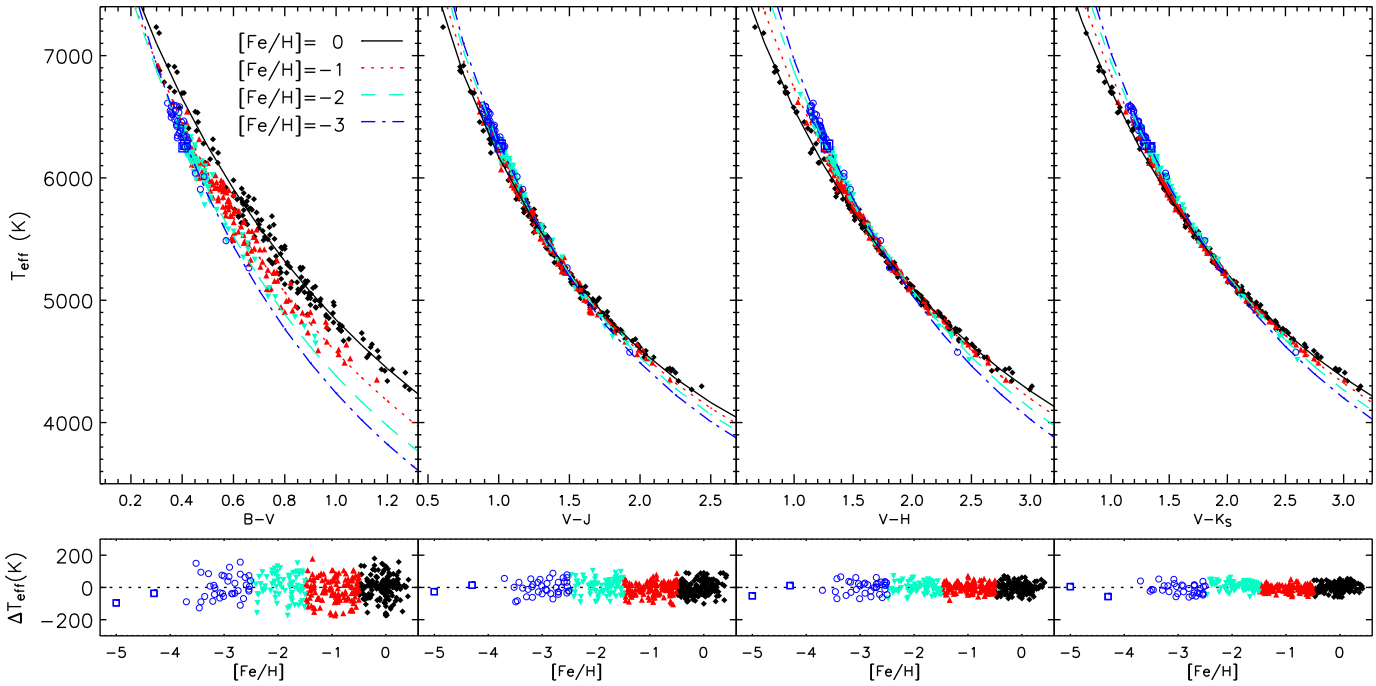

Fig. 14. Upper panels: empirical colour–temperature–metallicity calibrations in the metallicity bins $-0.5 < [\mathrm{Fe/H}] \leq 0.5$ (filled diamonds), $-1.5 < [\mathrm{Fe/H}] \leq -0.5$ (upward triangles), $-2.5 < [\mathrm{Fe/H}] \leq -1.5$ (downward triangles) and $[\mathrm{Fe/H}] \leq -2.5$ (open circles). Open squares are for the hyper metal-poor stars HE0233-0343 and HE1327-2326. Lower panels: residual of the fit as function of metallicity. For the two hyper-metal-poor stars, the residual is with respect to the fit at $[\mathrm{Fe/H}] = -3.5$.

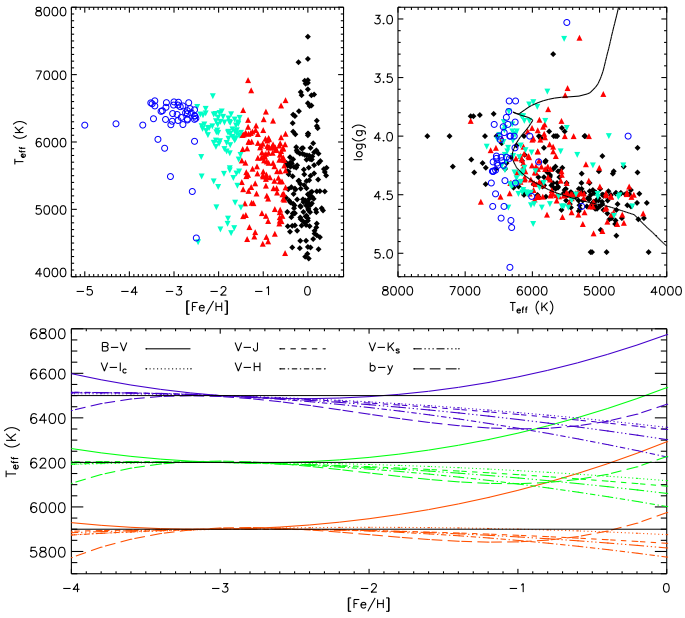

Fig. 13. Upper left panel: metallicities and effective temperatures of our sample. All stars have 2MASS and Johnson-Cousins photometry. Upper right panel: effective temperatures and gravities of our sample. Symbols for different metallicity bins are the same as in the left panel. Overplotted for reference is a 3 Gyr solar isochrone from Bertelli et al. (2008). Lower panel: metallicity sensitivity of our colour-temperature calibration in different bands for stars having $T_{\mathrm{eff}} = 6500$ K (top), 6200 K (middle) and 5900 K (lower) at $[\mathrm{Fe/H}] = -3.0$.

that changing them even considerably affects T_{eff} by an amount similar to that discussed for HE1327-2326. We adopt $[\mathrm{Fe/H}] = -4.0$ and $\log g = 4.0$ from which we derive $T_{\mathrm{eff}} = 6270 \pm 80$ K, without accounting for possible systematics arising from $E(B-V) = 0.025$ (Beers et al. 2007). As we point out in Section 6 there might be some issue with the R_C photometry for this star. Were we to exclude this band when running the IRFM, T_{eff} would increase by $25 - 35$ K depending on the surface gravity assumed. Spectroscopic T_{eff} estimates for this star are still uncertain, primarily because of its uncertain $\log g$. Were its subgiant status to be confirmed, our effective temperature would be in good agreement with the spectroscopic one (García Pérez et al. 2008).

6. Empirical calibrations

The effective temperatures and the bolometric luminosities derived via IRFM for our sample allow us to build calibrations relating those quantities to the measured colours and metallicities. As discussed in Section 2, to correctly account for reddening is crucial though fortunately, for the sake of deriving colour relations, reddening affects both the observed photometry and the derived fundamental stellar parameters, thus making such relations –built using dereddened colours– independent on the adopted $E(B-V)$ in first approximation.

In the following we give the functional form of these calibrations, together with the number of stars used, the standard deviation obtained in the fitting process and the range of applicability. The results presented here usually match Casagrande et al. (2006) within the limits of those calibrations, but extend over a wider range now and thus supersede the previous work. Though our sample has been assembled explicitly to cover a parameter space as large as possible in effective temperature and metallicity, the detection and observation of stars with $[\mathrm{Fe/H}] \lesssim -2.5$ is still strongly biased around $T_{\mathrm{eff}} \sim 6500$ K. Even if the formal range of applicability of the calibrations extend well below

[Fe/H] < -3, the number of known metal-poor stars considerably decreases as one moves away from the aforementioned $T_{\rm eff}$ (see Figure 13). In particular, for metallicities below -4, only two stars are currently known, a number clearly inadequate to give fits. Fortunately, at these temperatures calibrations at about -3.5 seem adequate for even more metal-poor stars, as we discuss further in Section 6.1 and 6.2. Nonetheless, we advocate particular caution when using these calibrations in poorly sampled regions of Figure 13. On the contrary for [Fe/H] $\gtrsim -2$, typical for most of the stellar population observed in the solar neighbourhood and Galactic star clusters, our calibrations are robust and can be readily used for a number of purposes.

The core of the present work is to accurately define the zero point of the temperature scale in many standard photometric systems; we caution however that in some cases real systems might not exactly reproduce standard systems, especially in the case of the faintest sources (Bessell 2005). Users of our calibrations should always keep this in mind: although the zero point of the $T_{\rm eff}$ scale is now well defined, in gathering photometry from heterogeneous sources there might be small zero point issues between different authors, and this observational uncertainty –if present– will introduce small systematic errors to our accurate empirical calibrations.

6.1. Colour–Temperature–Metallicity

To reproduce the observed $T_{\rm eff}$ versus colour relation and take into account the effects of metallicity, the usual fitting formula has been adopted (e.g. Alonso et al. 1996b; Ramírez & Meléndez 2005b; Casagrande et al. 2006; González Hernández & Bonifacio 2009)

$$\theta_{\rm eff} = a_0 + a_1 X + a_2 X^2 + a_3 X[{\rm Fe/H}] + a_4[{\rm Fe/H}] + a_5[{\rm Fe/H}]^2 \quad (3)$$

where $\theta_{\rm eff} = 5040/T_{\rm eff}$, X represents the colour and $a_i\,(i = 0,\ldots,5)$ are the coefficients of the fit obtained iteratively, discarding points departing more than 3σ.

The IRFM depends only very mildly on the adopted $\log g$ (Section 2.2) but certain colours could be more affected: for all indices we have checked the residual of our calibration and did not find any obvious trend with $\log g$. Nevertheless, a dependence on the gravity could be built into the calibrations, since $\log g$ decreases as one moves from cool dwarfs to hotter turn-off stars (Figure 13).

The coefficients for various colour indices are given with their range of applicability in Table 4 and a comparison between the polynomial fits and our sample of stars is shown in Figure 14. We remark that the functional form of Eq. (3) may return non-physical values when extrapolated to very low metallicities, as extensively discussed by Ryan et al. (1999) for the calibration of Alonso et al. (1996b) below [Fe/H] ~ -2.5. We have considerably increased the number of very metal-poor (turnoff) stars and our calibration behaves as one would expect, i.e. it shows a decreasing sensitivity on [Fe/H] when moving from -2 to -3, where the metallicity sensitivity vanishes in all bands (Figure 13). Moving to [Fe/H] $= -4$ (or lower), the diverging behaviour in Figure 13 reflects the form of the fitting function and the values of the coefficients rather than the characteristics of metal-poor turnoff stars. In Figure 14 the two hyper metal-poor stars (represented by open squares) clearly follow the same trend of other iron deficient stars with similar effective temperatures. Using Eq. (3) at a fixed [Fe/H] $= -3.5$ recovers their IRFM $T_{\rm eff}$ within the typical accuracy of the calibration. This is always true for HE1327-2326, and also for HE0233-0343 except when using the R_C index, possibly indicating a photometric issue in this band for the latter star. This comparison thus warrants the applicability of our calibrations for hyper-metal-poor stars if [Fe/H] $= -3.5$ is assumed and a typical $T_{\rm eff} \sim 6200$ K is obtained. How well this holds at other effective temperatures is still unknown.

The calibration presented here applies till late K-type dwarfs. Those interested in M dwarfs, can instead refer to Casagrande et al. (2008): though in that work the zero point has not been constrained using solar twins, the absolute calibration adopted was similar to that used here, resulting in effective temperatures approximately on the same scale. Nonetheless, if a link between the two scales is needed, we advise users to a careful case-by-case study, also considering that the calibration for M dwarfs has a different functional form and does not include any metallicity term.

6.1.1. Strömgren calibration

The Strömgren index $b-y$ deserves a separate discussion. It is often used as a $T_{\rm eff}$ indicator, but because of its very nature has a strong sensitivity on the metallicity and a proper functional form is not trivial. Alonso et al. (1996b) excluded the coolest dwarfs, where the dependence of $b-y$ upon $T_{\rm eff}$ possibly flattens out. Yet, for the most metal poor stars that calibration diverges to unphysical values, as discussed in Ryan et al. (1999).

For $b-y$ we have verified that a calibration of the form of Eq. (3) has strong residuals as function of both colour and metallicity and used polynomial fits to correct such trends, i.e. $T_{\rm eff} = 5040/\theta_{\rm eff} + P([{\rm Fe/H}], b-y)$. To this purpose, we have increased the sample with more than 1000 stars from the GCS catalogue (Nordström et al. 2004) all having Strömgren photometry, spectroscopic metallicities from an updated version of the Cayrel catalogue (Meléndez, in prep.) and for which the IRFM could be applied directly using Tycho2 and 2MASS (Casagrande et al. in prep.).

We checked that a third order polynomial in both colour and metallicity was enough; the calibration before and after adopting such a correction is shown in Figure 15 and the coefficients, given in the form $P([{\rm Fe/H}], b-y) = \sum_{i=0}^{3} M_i[{\rm Fe/H}]^i + \sum_{i=0}^{3} C_i(b-y)^i$ are $M_0 = -1.9$, $M_1 = 130.4$, $M_2 = 125.7$, $M_3 = 27.4$, $C_0 = -1003.7$, $C_1 = 7325.9$, $C_2 = -17207.4$, $C_3 = 12977.7$. Notice that the form of these corrections can lead to unphysical values if extrapolated and should never be applied outside of the colour and [Fe/H] ranges of Figure 15.

6.2. Colour–Flux–Metallicity

We adopt the same definition of Casagrande et al. (2006) to define the bolometric correction in a given ζ band, where

$$BC_\zeta = m_{\rm Bol} - m_\zeta \quad (4)$$

and the zero point of the $m_{\rm bol}$ scale is fixed by choosing $M_{{\rm Bol},\odot} = 4.74$. Empirical bolometric corrections in various bands can thus be readily computed using Eq. (4) and dereddening the observed magnitudes given in Table 8.

A complementary way of deriving stellar integrated flux via photometric indices is given in the form of Casagrande et al. (2006)

$$\mathcal{F}_{\rm Bol}({\rm Earth}) = 10^{-0.4\,{\rm m}_\zeta}\Big({\rm b}_0 + {\rm b}_1{\rm X} + {\rm b}_2{\rm X}^2 + {\rm b}_3{\rm X}^3 + b_4 X[{\rm Fe/H}] + b_5[{\rm Fe/H}] + b_6[{\rm Fe/H}]^2\Big). \quad (5)$$

Table 4. Coefficients and range of applicability of the colour–temperature–metallicity relations. The photometric systems are Johnson-Cousins $BV(RI)_C$, 2MASS JHK_S, Tycho2 $(BV)_T$ and Strömgren by. For the latter, additional corrections as function of [Fe/H] and $(b-y)$ apply, as discussed in Section 6.1.1. For some indices the calibrations are given down to [Fe/H] = −5.0, meaning that the effective temperatures of such a metal-poor star can be recovered using [Fe/H] = −3.5 in Eq. (3). Notice that only two hyper metal-poor stars are currently known and caution should be used, as discussed in the text. Especially for metal-poor stars, please refer to Figure 13 to check that the calibration is not extrapolated outside its [Fe/H] range.

Colour	[Fe/H] range	Colour range	a_0	a_1	a_2	a_3	a_4	a_5	N	$\sigma(T_{\rm eff})$
$B-V$	[−5.0, 0.4]	[0.18, 1.29]	0.5665	0.4809	−0.0060	−0.0613	−0.0042	−0.0055	400	73
$V-R_C$	[−5.0, 0.3]	[0.24, 0.80]	0.4386	1.4614	−0.7014	−0.0807	0.0142	−0.0015	201	62
$(R-I)_C$	[−5.0, 0.3]	[0.23, 0.68]	0.3296	1.9716	−1.0225	−0.0298	0.0329	0.0035	211	82
$V-I_C$	[−5.0, 0.3]	[0.46, 1.47]	0.4033	0.8171	−0.1987	−0.0409	0.0319	0.0012	208	59
$V-J$	[−5.0, 0.4]	[0.61, 2.44]	0.4669	0.3849	−0.0350	−0.0140	0.0225	0.0011	401	42
$V-H$	[−5.0, 0.4]	[0.67, 3.01]	0.5251	0.2553	−0.0119	−0.0187	0.0410	0.0025	401	33
$V-K_S$	[−5.0, 0.4]	[0.78, 3.15]	0.5057	0.2600	−0.0146	−0.0131	0.0288	0.0016	401	25
$J-K_S$	[−5.0, 0.4]	[0.07, 0.80]	0.6393	0.6104	0.0920	−0.0330	0.0291	0.0020	412	132
$(B-V)_T$	[−2.7, 0.4]	[0.19, 1.49]	0.5839	0.4000	−0.0067	−0.0282	−0.0346	−0.0087	251	79
V_T-J	[−2.7, 0.4]	[0.77, 2.56]	0.4525	0.3797	−0.0357	−0.0082	0.0123	−0.0009	272	43
V_T-H	[−2.7, 0.4]	[0.77, 3.16]	0.5286	0.2354	−0.0073	−0.0182	0.0401	0.0021	263	26
V_T-K_S	[−2.4, 0.4]	[0.99, 3.29]	0.4892	0.2634	−0.0165	−0.0121	0.0249	−0.0001	258	18
$b-y$	[−3.7, 0.5]	[0.18, 0.72]	0.5796	0.4812	0.5747	−0.0633	0.0042	−0.0055	1120	62

N is the number of stars employed for the fit after the 3σ clipping and $\sigma(T_{\rm eff})$ is the standard deviation (in Kelvin) of the proposed calibrations. Notice that the standard deviation does not account for the uncertainty in the zero point of the temperature scale, which is of order 15 − 20 K (Section 3.2 and 4.1).

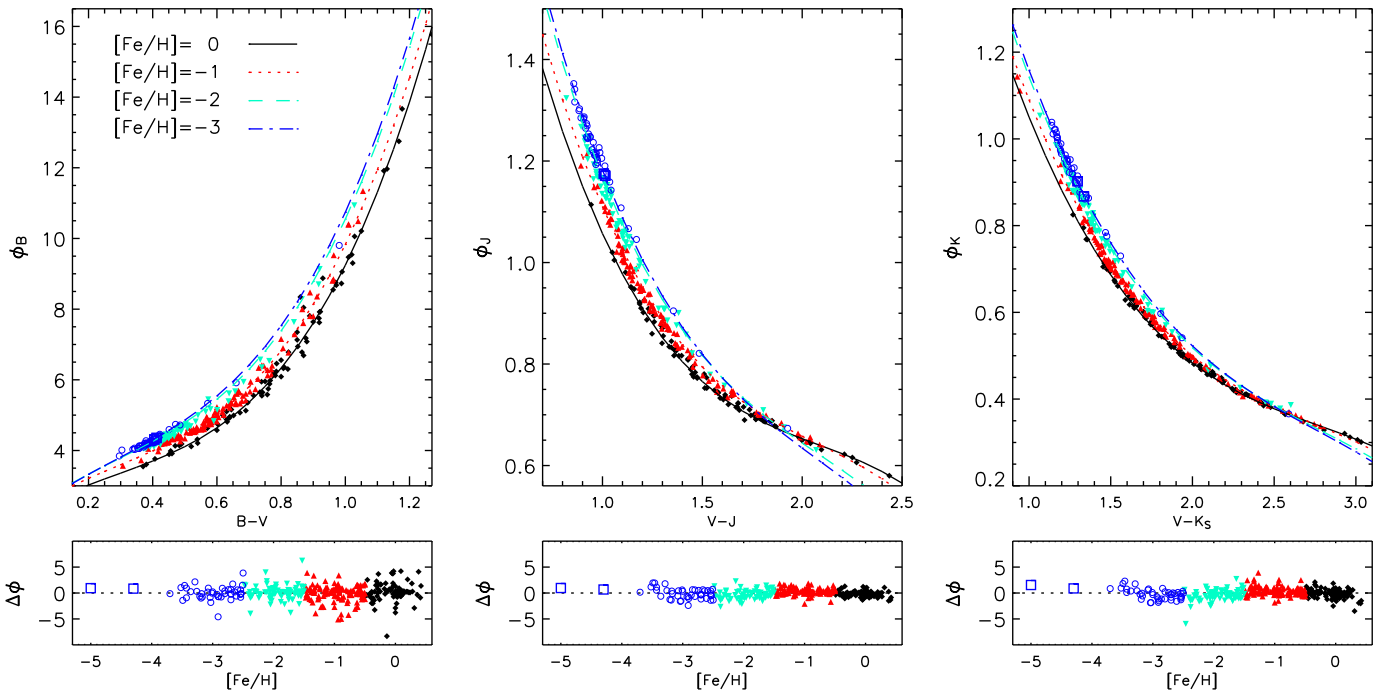

Fig. 16. Same as Figure 14, but for the colour–flux–metallicity calibrations. The reduced flux in different bands $\phi_\zeta = \mathcal{F}_{\rm Bol}({\rm Earth})\,10^{0.4\,{\rm m}_\zeta}$ is plotted as function of different colour indices in units of $10^{-0.5}{\rm erg\,cm^{-2}\,s^{-1}}$.

As for the temperature calibrations, also in this case the fluxes of the two hyper metal-poor stars can be recovered adopting [Fe/H] = −3.5 in Eq. (5), though we caution that the license of this approach for considerably bluer or redder indices is still unknown.

6.3. Colour-Angular diameters

Limb-darkened angular diameters can be readily derived from the basic definition involving effective temperatures and bolometric fluxes, using the calibrations given in Sections 6.1 and 6.2. Nonetheless, very tight and simple relations exist in the J band and in Table 6 we give them in the form of Casagrande et al. (2006)

$$\theta = c_0 + c_1\sqrt{\phi(m_J, X)} \quad (6)$$

where

$$\phi(m_J, X) = 10^{-0.4\,m_J}X \quad (7)$$

for a given colour index X. These relations show remarkably small scatter and no metallicity dependence, thus proving ideal

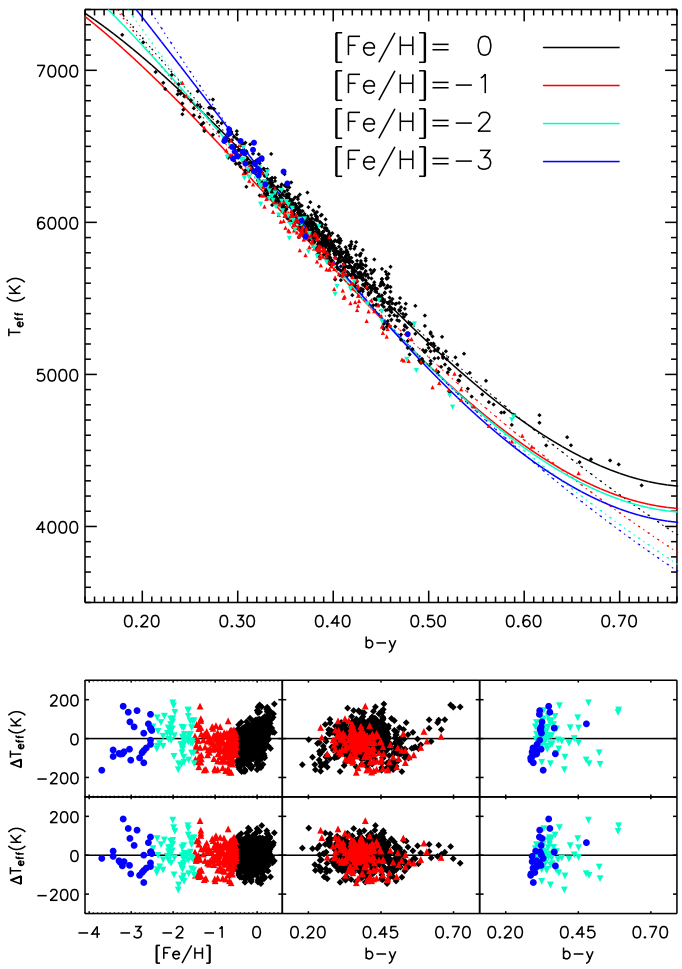

Fig. 15. Upper panel: empirical colour-temperature-metallicity calibration in $b-y$ before (dotted) and after (continuous lines) the polynomial correction. Central and lower panels: residuals before and after the polynomial corrections.

to build a network of small calibrators for interferometric measurements, for characterizing extrasolar planet transits or microlensing events.

6.4. The colours of the Sun

The interpolation of Eq. (3) at $T_{\rm eff} = 5777$ K and [Fe/H] = 0 returns the colours of the Sun, which are given in Table 7. For the Tycho2 and 2MASS system, those can be readily compared with the averaged ones from the twins of Section 3.1: not unexpectedly there is good agreement, all but one within few millimag, which usually (at maximum) correspond to few (20) K in $T_{\rm eff}$. We have also checked that fitting our twins as function of $T_{\rm eff}$ and [Fe/H] returns colours almost identical to their average, further confirming that our sample of twins is homogeneously distributed in temperature and metallicity around the colours of the Sun inferred from our scale.

In recent years, there has been considerable work in order to determine the colours of the Sun (e.g. Sekiguchi & Fukugita 2000; Ramírez & Meléndez 2005b; Holmberg et al. 2006; Pasquini et al. 2008). One of the most extensive analysis is that of Holmberg et al. (2006): the remarkably good agreement we have in the optical colours can be understood from the dependence of these indices on both $T_{\rm eff}$ and [Fe/H]. The approximately 100 K cooler effective temperature scale adopted by Holmberg et al. (2006) favours bluer colours, which are grossly compensated to the red by the underestimation of $\sim$ 0.1 dex in the GCS photometric metallicities with respect to spectroscopic ones selected to be consistent with our temperature scale (Holmberg et al. 2009). Our $B-V = 0.641$ is also in very good agreement with the $B-V = 0.649 \pm 0.016$ found studying solar twins in M67 (Pasquini et al. 2008). For this cluster, using our colour-temperature relation to compare $V-K_S$ photometry with theoretical isochrones shows remarkably good agreement (Vandenberg, private communication).

Infrared indices derived inverting Eq. (3) depend almost exclusively on the adopted $T_{\rm eff}$ scale, which is responsible for our much redder colours than those of Holmberg et al. (2006). Our $V-J$, H and K_S are in good agreement with those reported in Rieke et al. (2008) and obtained from solar-type stars or computed convolving various solar spectra with the appropriate filter curves and using their revised absolute physical calibration.

The empirical colours in Table 7 are also in agreement with the synthetic ones, computed using the same zero points and absolute calibration for Vega used in the IRFM to derive our $T_{\rm eff}$ scale. Therefore, the uncertainty in the zero points used to generate synthetic colours is at the smallest level possible, yet of the order of 0.01 mag. (Section 3.2), allowing us to address the reliability of the models at this level of precision. While using a theoretical spectra of Vega may (partly) compensate model inaccuracies in the process of setting the zero points, the approach adopted here allows us to focus on the quality of the solar synthetic spectra. The agreement is remarkable, on the order of 0.01 mag. and never exceeding 0.02, which is also of the same size of the difference between those synthetic models.

7. Conclusions

The primary goal of this work has been to provide a new absolute effective temperature scale. An unprecedented accuracy of few tens of Kelvin in the zero point of our scale has been achieved using a sample of solar twins. For these stars the high degree of resemblance to the Sun has been determined entirely model independently, without any prior assumption on their physical parameters, most importantly $T_{\rm eff}$. Notice that by calibrating our results via solar twins we are entirely unaffected from possible issues and uncertainties related to Vega. Nonetheless, we regard as comforting that our findings are in close agreement with the latest absolute fluxes (Cohen et al. 2003; Bohlin 2007; Rieke et al. 2008). We further took advantage of such a promising situation by fine-tuning the adopted fluxes so as to improve the consistency of the effective temperatures determined from each band used in the IRFM. This methodology gives us confidence that the stellar parameters we determined are well calibrated not only around the solar value, but over a wide range in $T_{\rm eff}$ and [Fe/H]. Notice that the IRFM is little model dependent and certainly not at the solar value because of our calibration procedure. Small spurious trends arising from the adopted library at different temperatures and metallicities can not be entirely ruled out, but should be small. Though the zero point of our new $T_{\rm eff}$ scale is entirely set by solar twins, it agrees within few degrees with independent verifications conducted via interferometric angular diameters and HST spectrophotometry in the metal-poor and -rich regimes.

In the process of establishing the zero point of the effective temperature scale via IRFM, we nailed down the differences with respect to other implementations of the same technique. We have used two independent IRFM versions to study the dis-

crepancies among various temperature scales that appeared in literature over the years and proved that the absolute calibration of the photometric systems used was responsible for explaining most of the differences. At solar temperatures and metallicities the long-standing dichotomy between photometric and spectroscopic $T_{\rm eff}$ is easily explained once it is understood that the IRFM can in principle accommodate any temperature scale since its zero point depends on the absolute calibration of the photometry adopted. The main goal of the present paper has been exactly to tackle this issue using the best constraint available to date.

The improved bolometric fluxes determined for metal-poor stars have also been used to put on firmer ground the temperature scale in this rather unexplored regime. For metallicities typical of halo stars our $T_{\rm eff}$ scale is roughly 100 K hotter than those determined from the Balmer lines and 200 K hotter than those obtained from the excitation equilibrium. While spectroscopic effective temperature determinations have considerable model dependence and are degenerate with other stellar parameters (namely $\log g$ and [Fe/H]), the IRFM offers a powerful alternative, free from any of the above limitations. However, relying on the photometry, the IRFM is influenced by reddening, which becomes a considerable source of uncertainty when targeting objects outside of the local bubble. For our sample of metal-poor stars we have been cautious in determining reddening as best we could. Our improved determination of $E(B-V)$ also explain the remaining discrepancies with other $T_{\rm eff}$ scales. We think the effective temperatures determined for our sample of stars will serve to better calibrate spectroscopic $T_{\rm eff}$ determinations. This will be particularly relevant when large spectroscopic surveys targeting different stellar populations in the Galaxy start operating: support from the existing or forthcoming photometric surveys will be possible only if reddening will be determined on a star-by-star basis. We feel this will not be possible in many cases and stellar parameters will have to rely on spectroscopy only.

Based on our sample of dwarfs and subgiants, a set of homogeneously calibrated colours versus temperatures, bolometric fluxes and angular diameters have also been determined. A number of problems of interest to stellar and Galactic Chemical evolution depend on the assumption made in these relations and our results will permit those problems to be tackled with greater confidence.

Acknowledgements. We thank Ana García-Pérez for preliminary results on HE0233-0343 and interesting discussion on excitation temperatures in metal-poor stars. We are also indebted to Maria Bergemann and Andreas Korn for many insights on determining effective temperatures from Balmer lines. Martin Cohen is acknowledged for useful correspondence on the absolute calibration and Gerard van Belle for enlightening discussions on interferometry at various times. Don Vandenberg is kindly acknowledged for useful correspondence and for a preliminary comparison of our temperature scale with M67. We thank an anonymous referee for relevant comments and suggestions that helped to strength the presentation and clarify the results. JM is supported by a Ciência 2007 contract (FCT/MCTES/Portugal and POPH/FSE/EC) and acknowledges financial support from PTDC/CTE-AST/65971/2006 (FCT/Portugal). This research has made use of the General Catalogue of Photometric data operated at the University of Lausanne and the SIMBAD database, operated at CDS, Strasbourg, France. This publication makes use of data products from the Two Micron All Sky Survey, which is a joint project of the University of Massachusetts and the Infrared Processing and Analysis Center/California Institute of Technology, funded by the National Aeronautics and Space Administration and the National Science Foundation.

References

Allende Prieto, C., Asplund, M., García López, R. J., & Lambert, D. L. 2002, ApJ, 567, 544
Alonso, A., Arribas, S., & Martinez-Roger, C. 1994a, A&A, 282, 684
Alonso, A., Arribas, S., & Martinez-Roger, C. 1994b, A&AS, 107, 365
Alonso, A., Arribas, S., & Martinez-Roger, C. 1995, A&A, 297, 197
Alonso, A., Arribas, S., & Martinez-Roger, C. 1996a, A&AS, 117, 227
Alonso, A., Arribas, S., & Martinez-Roger, C. 1996b, A&A, 313, 873
Aoki, W., Barklem, P. S., Beers, T. C., et al. 2009, ApJ, 698, 1803
Aoki, W., Frebel, A., Christlieb, N., et al. 2006, ApJ, 639, 897
Asplund, M. 2005, ARA&A, 43, 481
Asplund, M. & García Pérez, A. E. 2001, A&A, 372, 601
Baines, E. K., McAlister, H. A., ten Brummelaar, T. A., et al. 2008, ApJ, 680, 728
Barklem, P. S. 2007, A&A, 466, 327
Barklem, P. S., Piskunov, N., & O'Mara, B. J. 2000, A&AS, 142, 467
Barklem, P. S., Stempels, H. C., Allende Prieto, C., et al. 2002, A&A, 385, 951
Beers, T. C., Flynn, C., Rossi, S., et al. 2007, ApJS, 168, 128
Bell, R. A. & Gustafsson, B. 1989, MNRAS, 236, 653
Bergemann, M. 2008, Physica Scripta Volume T, 133, 014013
Bertelli, G., Girardi, L., Marigo, P., & Nasi, E. 2008, A&A, 484, 815
Bessell, M. S. 2000, PASP, 112, 961
Bessell, M. S. 2005, ARA&A, 43, 293
Bessell, M. S. & Brett, J. M. 1988, PASP, 100, 1134
Bessell, M. S., Castelli, F., & Plez, B. 1998, A&A, 333, 231
Biazzo, K., Frasca, A., Catalano, S., & Marilli, E. 2007, Astronomische Nachrichten, 328, 938
Bigot, L., Kervella, P., Thévenin, F., & Ségransan, D. 2006, A&A, 446, 635
Blackwell, D. E., Petford, A. D., & Shallis, M. J. 1980, A&A, 82, 249
Blackwell, D. E. & Shallis, M. J. 1977, MNRAS, 180, 177
Blackwell, D. E., Shallis, M. J., & Selby, M. J. 1979, MNRAS, 188, 847
Bohlin, R. C. 2007, in Astronomical Society of the Pacific Conference Series, Vol. 364, The Future of Photometric, Spectrophotometric and Polarimetric Standardization, ed. C. Sterken, 315–+
Bohlin, R. C. & Gilliland, R. L. 2004, AJ, 127, 3508
Bonifacio, P., Molaro, P., Sivarani, T., et al. 2007, A&A, 462, 851
Boyajian, T. S., McAlister, H. A., Baines, E. K., et al. 2008, ApJ, 683, 424
Brown, T. M., Charbonneau, D., Gilliland, R. L., Noyes, R. W., & Burrows, A. 2001, ApJ, 552, 699
Caccin, B., Penza, V., & Gomez, M. T. 2002, A&A, 386, 286
Campins, H., Rieke, G. H., & Lebofsky, M. J. 1985, AJ, 90, 896
Cardelli, J. A., Clayton, G. C., & Mathis, J. S. 1989, ApJ, 345, 245
Casagrande, L. 2008, Physica Scripta Volume T, 133, 014020
Casagrande, L. 2009, Memorie della Societa Astronomica Italiana, 80, 727
Casagrande, L., Flynn, C., & Bessell, M. 2008, MNRAS, 389, 585
Casagrande, L., Portinari, L., & Flynn, C. 2006, MNRAS, 373, 13
Castelli, F. & Kurucz, R. L. 1994, A&A, 281, 817
Castelli, F. & Kurucz, R. L. 2004, astro-ph/0405087
Cayrel de Strobel, G. 1996, A&A Rev., 7, 243
Cayrel de Strobel, G. & Bentolila, C. 1989, A&A, 211, 324
Cayrel de Strobel, G., Soubiran, C., & Ralite, N. 2001, A&A, 373, 159
Charbonneau, D., Brown, T. M., Latham, D. W., & Mayor, M. 2000, ApJ, 529, L45
Cohen, M., Wheaton, W. A., & Megeath, S. T. 2003, AJ, 126, 1090
di Benedetto, G. P. & Rabbia, Y. 1987, A&A, 188, 114
Edvardsson, B. 2008, Physica Scripta Volume T, 133, 014011
Fabbian, D., Nissen, P. E., Asplund, M., Pettini, M., & Akerman, C. 2009, A&A, 500, 1143
Frebel, A., Aoki, W., Christlieb, N., et al. 2005, Nature, 434, 871
Frebel, A., Collet, R., Eriksson, K., Christlieb, N., & Aoki, W. 2008, ApJ, 684, 588
Fuhrmann, K. 2008, MNRAS, 384, 173
Fukugita, M., Ichikawa, T., Gunn, J. E., et al. 1996, AJ, 111, 1748
García Pérez, A. E., Christlieb, N., Ryan, S. G., et al. 2008, Physica Scripta Volume T, 133, 014036
González Hernández, J. I. & Bonifacio, P. 2009, A&A, 497, 497
Gray, D. F. 1994, PASP, 106, 1248
Gray, D. F. & Johanson, H. L. 1991, PASP, 103, 439
Gray, R. O. 2007, in Astronomical Society of the Pacific Conference Series, Vol. 364, The Future of Photometric, Spectrophotometric and Polarimetric Standardization, ed. C. Sterken, 305–+
Grupp, F. 2004, A&A, 426, 309
Gustafsson, B., Edvardsson, B., Eriksson, K., et al. 2008, A&A, 486, 951
Hanbury Brown, R., Davis, J., & Allen, L. R. 1974, MNRAS, 167, 121
Høg, E., Fabricius, C., Makarov, V. V., et al. 2000, A&A, 355, L27
Holmberg, J., Flynn, C., & Portinari, L. 2006, MNRAS, 367, 449
Holmberg, J., Nordström, B., & Andersen, J. 2009, A&A, 501, 941
Hosford, A., Ryan, S. G., García Pérez, A. E., Norris, J. E., & Olive, K. A. 2009, A&A, 493, 601
Hutter, D. J., Johnston, K. J., Mozurkewich, D., et al. 1989, ApJ, 340, 1103
Johnson, H. L. 1965, Communications of the Lunar and Planetary Laboratory, 3, 73

Kervella, P. & Fouqué, P. 2008, A&A, 491, 855
Korn, A. J., Richard, O., Mashonkina, L., et al. 2009, ApJ, 698, 410
Kovtyukh, V. V., Soubiran, C., Belik, S. I., & Gorlova, N. I. 2003, A&A, 411, 559
Kurucz, R. L. 1993, ATLAS9 Stellar Atmosphere Programs and 2 km/s grid. Kurucz CD-ROM No. 13. Cambridge, Mass.: Smithsonian Astrophysical Observatory, 1993., 13
Lallement, R., Welsh, B. Y., Vergely, J. L., Crifo, F., & Sfeir, D. 2003, A&A, 411, 447
Latham, D. W., Mazeh, T., Carney, B. W., et al. 1988, AJ, 96, 567
Leroy, J. L. 1993, A&A, 274, 203
Ludwig, H., Behara, N. T., Steffen, M., & Bonifacio, P. 2009, A&A, 502, L1
Maíz-Apellániz, J. 2007, in Astronomical Society of the Pacific Conference Series, Vol. 364, The Future of Photometric, Spectrophotometric and Polarimetric Standardization, ed. C. Sterken, 227–+
Masana, E., Jordi, C., & Ribas, I. 2006, A&A, 450, 735
McCall, M. L. 2004, AJ, 128, 2144
Meléndez, J., Asplund, M., Gustafsson, B., & Yong, D. 2009a, ApJ, 704, L66
Meléndez, J., Casagrande, L., Ramírez, I., Asplund, M., & Schuster, W. I. 2009b, A&A, submitted
Meléndez, J., Dodds-Eden, K., & Robles, J. A. 2006a, ApJ, 641, L133
Meléndez, J. & Ramírez, I. 2004, ApJ, 615, L33
Meléndez, J. & Ramírez, I. 2007, ApJ, 669, L89
Meléndez, J., Ramírez, I., Casagrande, L., et al. 2009c, astro-ph/0910.5845
Meléndez, J., Shchukina, N. G., Vasiljeva, I. E., & Ramírez, I. 2006b, ApJ, 642, 1082
Mermilliod, J.-C., Mermilliod, M., & Hauck, B. 1997, A&AS, 124, 349
Mozurkewich, D., Johnston, K. J., Simon, R. S., et al. 1991, AJ, 101, 2207
Munari, U., Sordo, R., Castelli, F., & Zwitter, T. 2005, A&A, 442, 1127
Nissen, P. E., Akerman, C., Asplund, M., et al. 2007, A&A, 469, 319
Nordgren, T. E., Germain, M. E., Benson, J. A., et al. 1999, AJ, 118, 3032
Nordström, B., Mayor, M., Andersen, J., et al. 2004, A&A, 418, 989
North, J. R., Davis, J., Robertson, J. G., et al. 2009, MNRAS, 393, 245
O'Donnell, J. E. 1994, ApJ, 422, 158
Pasquini, L., Biazzo, K., Bonifacio, P., Randich, S., & Bedin, L. R. 2008, A&A, 489, 677
Pereira, T., Asplund, M., Trampedach, R., & Collet, R. 2009, A&A, submitted
Porto de Mello, G. F. & da Silva, L. 1997, ApJ, 482, L89+
Ramírez, I., Allende Prieto, C., Redfield, S., & Lambert, D. L. 2006, A&A, 459, 613
Ramírez, I. & Meléndez, J. 2005a, ApJ, 626, 446
Ramírez, I. & Meléndez, J. 2005b, ApJ, 626, 465
Ramírez, I., Meléndez, J., & Asplund, M. 2009, A&A, 508, L17
Ridgway, S. T., Joyce, R. R., White, N. M., & Wing, R. F. 1980, ApJ, 235, 126
Rieke, G. H., Blaylock, M., Decin, L., et al. 2008, AJ, 135, 2245
Ryan, S. G., Norris, J. E., & Beers, T. C. 1999, ApJ, 523, 654
Schuster, W. J. & Nissen, P. E. 1989, A&A, 221, 65
Sekiguchi, M. & Fukugita, M. 2000, AJ, 120, 1072
Skrutskie, M. F., Cutri, R. M., Stiening, R., et al. 2006, AJ, 131, 1163
Smith, J. A., Tucker, D. L., Kent, S., et al. 2002, AJ, 123, 2121
Sousa, S. G., Santos, N. C., Mayor, M., et al. 2008, A&A, 487, 373
Takeda, Y. & Tajitsu, A. 2009, PASJ, 61, 471
Valenti, J. A. & Fischer, D. A. 2005, ApJS, 159, 141
van Belle, G. T. & von Braun, K. 2009, ApJ, 694, 1085
van Leeuwen, F. 2007, A&A, 474, 653
VandenBerg, D. A. & Clem, J. L. 2003, AJ, 126, 778
Venn, K. A. & Lambert, D. L. 2008, ApJ, 677, 572
White, N. M. & Feierman, B. H. 1987, AJ, 94, 751

Table 5. Coefficients and range of applicability of the flux calibrations for various $\phi_\zeta = \mathcal{F}_{\rm Bol}({\rm Earth})\,10^{0.4\,{\rm m}_\zeta}$.

ϕ_ζ	Colour	[Fe/H] range	Colour range	b_0	b_1	b_2	b_3	b_4	b_5	b_6	N	σ(%)
B_T	$(B-V)_T$	[−2.7, 0.4]	[0.19, 1.43]	2.1904	5.7106	−6.7110	7.4160	−0.6704	−0.1501	−0.0720	260	3.1
B_T	V_T-J	[−2.7, 0.4]	[0.51, 2.56]	1.8160	3.2833	−2.3210	1.7358	1.2140	−1.0830	0.0343	261	4.2
B_T	V_T-H	[−2.7, 0.4]	[0.53, 3.16]	1.7597	3.1896	−1.8419	0.9465	0.9826	−0.9055	0.0809	255	4.0
B_T	V_T-K_S	[−2.7, 0.4]	[0.59, 3.29]	1.7202	3.0146	−1.6377	0.8033	0.8591	−0.8644	0.0669	262	3.9
V_T	$(B-V)_T$	[−2.7, 0.4]	[0.19, 1.43]	2.7098	−0.2765	0.1523	0.8122	−0.2261	−0.1789	−0.0413	253	2.7
V_T	V_T-J	[−2.7, 0.4]	[0.62, 2.53]	2.1815	0.9268	−0.7701	0.4029	0.1047	−0.2609	−0.0048	249	0.7
V_T	V_T-H	[−2.7, 0.4]	[0.68, 3.16]	2.1800	0.8514	−0.5793	0.2235	0.0936	−0.2458	0.0019	261	0.9
V_T	V_T-K_S	[−2.7, 0.4]	[0.59, 3.29]	2.2565	0.6787	−0.4536	0.1800	0.0785	−0.2407	−0.0011	256	0.9
B	$B-V$	[−5.0, 0.4]	[0.18, 1.22]	1.9571	6.9680	−11.0277	11.4450	−0.4975	−0.1276	−0.0432	331	2.3
B	$V-R_C$	[−5.0, 0.3]	[0.24, 0.79]	2.0002	6.6483	−4.6407	25.3881	0.9547	−0.3756	−0.0067	186	1.9
B	$(R-I)_C$	[−5.0, 0.3]	[0.23, 0.68]	9.8257	−57.0297	152.2749	−77.6378	4.3253	−1.1377	0.0411	202	3.2
B	$V-I_C$	[−5.0, 0.3]	[0.46, 1.47]	4.3948	−6.0713	9.6862	0.2327	0.9298	−0.5392	0.0089	196	1.6
B	$V-J$	[−5.0, 0.4]	[0.50, 2.44]	1.6664	3.5465	−2.5257	1.5310	0.4259	−0.4354	0.0047	332	2.8
B	$V-H$	[−5.0, 0.4]	[0.52, 2.84]	1.6852	3.2925	−1.9206	0.8026	0.2172	−0.1301	0.0346	328	2.9
B	$V-K_S$	[−5.0, 0.4]	[0.57, 3.03]	1.5185	3.3566	−1.8830	0.7301	0.2887	−0.2929	0.0240	363	2.8
V	$B-V$	[−5.0, 0.4]	[0.30, 1.03]	1.2581	5.8828	−9.9287	6.8432	0.2290	−0.3935	−0.0420	241	1.9
V	$V-R_C$	[−5.0, 0.3]	[0.24, 0.79]	2.6659	−1.6396	3.9243	2.9911	0.0978	−0.2339	−0.0252	177	0.7
V	$(R-I)_C$	[−5.0, 0.3]	[0.25, 0.68]	4.9994	−20.1727	49.0418	−27.5918	0.9465	−0.4491	−0.0166	197	1.5
V	$V-I_C$	[−5.0, 0.3]	[0.48, 1.47]	3.4468	−3.8760	4.5692	−0.7285	0.1832	−0.2991	−0.0231	184	0.8
V	$V-J$	[−5.0, 0.4]	[0.73, 2.21]	1.8195	1.5562	−1.3322	0.5627	0.1249	−0.3112	−0.0213	314	0.8
V	$V-H$	[−5.0, 0.4]	[0.67, 3.01]	2.0139	1.0845	−0.8071	0.2761	0.0567	−0.2147	−0.0124	369	0.9
V	$V-K_S$	[−5.0, 0.4]	[0.93, 3.15]	1.7662	1.4154	−0.9302	0.2726	0.0692	−0.2506	−0.0160	316	0.9
R_C	$B-V$	[−5.0, 0.3]	[0.35, 1.29]	2.5759	−1.8536	1.3042	0.1015	−0.0130	−0.1229	−0.0142	179	0.8
R_C	$V-R_C$	[−5.0, 0.3]	[0.24, 0.79]	2.7031	−4.2859	6.9274	−2.1959	0.1482	−0.1968	−0.0186	180	0.7
R_C	$(R-I)_C$	[−5.0, 0.3]	[0.23, 0.68]	3.2131	−8.5410	17.3691	−9.1350	0.4602	−0.3054	−0.0171	203	1.0
R_C	$V-I_C$	[−5.0, 0.3]	[0.48, 1.47]	2.9759	−3.2013	2.9454	−0.6516	0.1331	−0.2408	−0.0187	185	0.7
R_C	$V-J$	[−5.0, 0.3]	[0.86, 2.36]	2.5806	−1.0234	0.4055	0.0107	0.0874	−0.2508	−0.0181	184	0.7
R_C	$V-H$	[−5.0, 0.3]	[0.93, 2.99]	2.5007	−0.6801	0.1842	0.0176	0.0746	−0.2604	−0.0185	196	0.7
R_C	$V-K_S$	[−5.0, 0.3]	[1.00, 3.13]	2.5606	−0.7448	0.2212	0.0049	0.0665	−0.2509	−0.0184	193	0.7
I_C	$B-V$	[−5.0, 0.3]	[0.35, 1.29]	2.6765	−3.8643	3.7834	−1.2273	0.0145	−0.0358	−0.0015	200	1.0
I_C	$V-R_C$	[−5.0, 0.3]	[0.24, 0.79]	2.6963	−6.8081	11.3579	−6.1859	0.1798	−0.1418	−0.0112	191	1.1
I_C	$(R-I)_C$	[−5.0, 0.3]	[0.27, 0.68]	3.1500	−10.0132	18.2682	−10.8668	0.3653	−0.2329	−0.0123	177	0.9
I_C	$V-I_C$	[−5.0, 0.3]	[0.48, 1.47]	3.0203	−4.5225	4.0375	−1.1781	0.1371	−0.1866	−0.0122	197	0.8
I_C	$V-J$	[−5.0, 0.3]	[0.86, 2.36]	2.7912	−2.2548	1.1687	−0.1986	0.0817	−0.1908	−0.0118	186	1.1
I_C	$V-H$	[−5.0, 0.3]	[0.93, 2.99]	2.7888	−1.8271	0.7688	−0.1061	0.0734	−0.2132	−0.0138	187	1.0
I_C	$V-K_S$	[−5.0, 0.3]	[1.00, 3.13]	2.7797	−1.7014	0.6710	−0.0868	0.0603	−0.1891	−0.0123	193	0.9
J	$B-V$	[−5.0, 0.4]	[0.30, 1.29]	2.2253	−3.5932	2.9303	−0.8741	0.0199	0.0132	0.0057	346	3.4
J	$V-R_C$	[−5.0, 0.3]	[0.24, 0.79]	2.5765	−8.1969	12.1713	−6.3037	0.1393	−0.0769	−0.0048	186	2.9
J	$(R-I)_C$	[−5.0, 0.3]	[0.27, 0.68]	2.9723	−10.6481	16.3430	−8.5334	0.2971	−0.1854	−0.0095	195	3.0
J	$V-I_C$	[−5.0, 0.3]	[0.52, 1.47]	2.8966	−5.1154	4.0119	−1.0879	0.1059	−0.1232	−0.0066	192	2.6
J	$V-J$	[−5.0, 0.4]	[0.82, 2.44]	2.7915	−2.8096	1.2799	−0.2049	0.0479	−0.1059	−0.0054	308	0.8
J	$V-H$	[−5.0, 0.4]	[0.88, 2.99]	2.5885	−2.0262	0.7430	−0.0963	0.0587	−0.1577	−0.0092	303	1.9
J	$V-K_S$	[−5.0, 0.4]	[0.93, 3.13]	2.5578	−1.8710	0.6433	−0.0785	0.0457	−0.1326	−0.0078	314	1.7
H	$B-V$	[−5.0, 0.4]	[0.18, 1.29]	2.1337	−3.6473	2.6261	−0.6782	−0.0780	0.1274	0.0179	331	4.6
H	$V-R_C$	[−5.0, 0.3]	[0.24, 0.79]	2.5341	−8.8850	12.8801	−6.5281	0.0339	−0.0012	0.0022	184	3.6
H	$(R-I)_C$	[−5.0, 0.3]	[0.23, 0.68]	2.9097	−11.1909	16.5901	−8.3344	0.1844	−0.1169	−0.0047	192	3.6
H	$V-I_C$	[−5.0, 0.3]	[0.48, 1.47]	2.8833	−5.5447	4.2495	−1.1267	0.0504	−0.0512	−0.0009	195	3.1
H	$V-J$	[−5.0, 0.4]	[0.50, 2.44]	2.5764	−2.6119	1.0580	−0.1490	0.0033	−0.0098	0.0031	353	2.8
H	$V-H$	[−5.0, 0.4]	[0.88, 3.01]	2.4574	−2.0093	0.6768	−0.0808	0.0246	−0.0665	−0.0016	344	1.0
H	$V-K_S$	[−5.0, 0.4]	[0.57, 3.15]	2.3732	−1.7778	0.5485	−0.0599	0.0140	−0.0407	0.0005	363	2.2
K_S	$B-V$	[−5.0, 0.4]	[0.30, 1.29]	2.1537	−3.9640	3.0680	−0.8653	−0.0586	0.1098	0.0163	353	4.9
K_S	$V-R_C$	[−5.0, 0.3]	[0.24, 0.76]	2.5709	−9.5441	14.4103	−7.6430	0.0585	−0.0186	0.0006	190	3.8
K_S	$(R-I)_C$	[−5.0, 0.3]	[0.25, 0.68]	2.8803	−11.4591	17.4060	−9.0419	0.2418	−0.1469	−0.0066	199	3.6
K_S	$V-I_C$	[−5.0, 0.3]	[0.48, 1.47]	2.7928	−5.4377	4.1682	−1.1105	0.0661	−0.0690	−0.0019	201	3.2
K_S	$V-J$	[−5.0, 0.4]	[0.50, 2.36]	2.6548	−2.8832	1.2411	−0.1878	0.0146	−0.0315	0.0013	328	2.9
K_S	$V-H$	[−5.0, 0.4]	[0.88, 2.99]	2.4939	−2.1600	0.7593	−0.0946	0.0342	−0.0879	−0.0029	317	2.5
K_S	$V-K_S$	[−5.0, 0.4]	[0.93, 3.03]	2.5097	−2.0732	0.6972	−0.0836	0.0229	−0.0641	−0.0017	328	1.1

N is the number of stars employed for the fit after the 3 sigma clipping and σ(%) is the standard deviation of the final calibrations in percent. The coefficients of the calibrations b_i are given in units of $10^{-0.5}$erg cm^{-2} s^{-1}.

Table 6. Coefficients and range of applicability of the angular diameter calibrations.

Colour	Colour range	c_0	c_1	N	σ(%)
$V-J$	[0.73, 2.44]	0.00015	4.65293	394	2.2
$V-H$	[0.88, 3.01]	0.00004	4.15613	389	1.8
$V-K_S$	[0.93, 3.15]	0.00020	4.05037	394	1.9
V_T-J	[0.72, 2.56]	0.00218	4.44568	270	2.1
V_T-H	[0.87, 3.14]	0.00227	3.98945	255	1.5
V_T-K_S	[0.92, 3.27]	0.00286	3.88433	268	1.5

N is the number of stars employed for the fit after the 3σ clipping and σ(%) is the standard deviation of the calibrations.

Table 7. The colours of the Sun. For the indices obtained inverting our $T_{\rm eff}$ scale, random errors are from the dispersion of the fits in Table 4. The uncertainty on the zero point of our $T_{\rm eff}$ scale is of order 15 K (Section 3.2), which usually implies systematic errors considerably smaller than the random ones. The only exception is for optical-infrared indices which are very sensitive to $T_{\rm eff}$ and show small intrinsic scatter, of the order of the aforementioned zero point uncertainty. Also shown for comparison are the averaged colours and standard deviation of the solar twins, as well as the synthetic colours computed from the ATLAS9 (Castelli & Kurucz 2004) and MARCS (Gustafsson et al. 2008) models.

	$T_{\rm eff}$ scale (rand. + syst. errors)	MARCS	ATLAS9	Twins
$B-V$	0.641 ± 0.024 ± 0.004	0.622	0.645	
$V-R_C$	0.359 ± 0.010 ± 0.003	0.357	0.358	
$(R-I)_C$	0.333 ± 0.010 ± 0.002	0.347	0.349	
$V-I_C$	0.690 ± 0.016 ± 0.004	0.704	0.707	
$V-J$	1.180 ± 0.021 ± 0.007	1.171	1.180	
$V-H$	1.460 ± 0.023 ± 0.010	1.458	1.479	
$V-K_S$	1.544 ± 0.018 ± 0.010	1.543	1.553	
$J-K_S$	0.362 ± 0.029 ± 0.003	0.372	0.373	
$(B-V)_T$	0.730 ± 0.031 ± 0.006	0.723	0.750	0.735 ± 0.024[a]
V_T-J	1.254 ± 0.022 ± 0.008	1.240	1.250	1.254 ± 0.041[a]
V_T-H	1.534 ± 0.019 ± 0.011	1.527	1.550	1.549 ± 0.048[a]
V_T-K_S	1.619 ± 0.013 ± 0.011	1.612	1.623	1.623 ± 0.040[a]
$b-y$	0.409 ± 0.010 ± 0.002			0.409 ± 0.003[b]

[a] Average and standard deviation of the colours in Table 2.
[b] From Meléndez et al. in prep., fitting solar twin colours as a function of $T_{\rm eff}$ and [Fe/H].

Appendix A: Comparing the TCS and 2MASS absolute calibration

The absolute calibration of Alonso et al. (1994a) was obtained applying the IRFM to a sample of stars for which direct measurements of angular diameters were available. Because of the difficulties involved in achieving milliarcsecond resolution, that sample was almost entirely composed of giants with angular diameters measured via Lunar Occultations and Michelson Interferometry ($T_{\rm eff} < 5000$ K) or Intensity Interferometry ($T_{\rm eff} > 6000$ K). One of the intriguing results of that analysis was the impossibility of setting the same zero point of the absolute calibration using angular diameters measured by Lunar Occultations (White & Feierman 1987; Ridgway et al. 1980) and Michelson Interferometry (Hutter et al. 1989; di Benedetto & Rabbia 1987; Mozurkewich et al. 1991) with those measured by Intensity Interferometry (Hanbury Brown et al. 1974). The absolute calibration (in the Johnson system) proposed by Alonso et al. (1994a) is a weighted average from their table 10 and it is interesting to notice that the one derived from Intensity Interferometry alone is 4.8 (J) 1.3 (H) and 4.0 (K) percent lower than the averaged, proposed one. As we have discuss throughout the paper[8], lower infrared fluxes support higher $T_{\rm eff}$ (in this case, the average difference in Johnson system would be 3.4% supporting $T_{\rm eff}$ approximately hotter by 70 K), so it is not surprising our effective temperature scale provides good agreement with interferometric measurements despite being considerably hotter than most of the previous IRFM analyses.

To gauge a further insight into the problem, here we directly compare the TCS (given in Alonso et al. 1994b) and 2MASS absolute calibration. Such an exercise, however is not straightforward since the absolute calibration in different photometric system is obtained using different filter transmission curves and therefore is associated to different effective wavelengths. In addition, for the sake of the IRFM, in any given band ζ, it is the composite effect of Vega's magnitudes and fluxes which matters, i.e. $\mathcal{F}_\zeta 10^{0.4{\rm m}_\zeta}$. Therefore, for a meaningful comparison we need to refer everything to a common wavelength, the 2MASS one being the natural choice in this case. This is done in Table A.1 by computing $\mathcal{F}_{\rm eff}$ i.e the composite effect of magnitudes and fluxes shifted to the 2MASS $\lambda_{\rm eff}$ in the case of TCS (Figure A.1).

The 2MASS absolute calibration is on the average lower than the TCS by 4.6% (a value qualitatively in agreement with the difference in the Johnson system discussed above), thus returning $T_{\rm eff}$ on average hotter by ~ 90 K, and explaining the bulk of the differences discussed in Section 2.3 when comparing the sample stars directly. Similar conclusions can be drawn when comparing with the absolute fluxes and magnitudes of Vega used in table 1 of González Hernández & Bonifacio (2009). In this case the photometric system is the same (2MASS) and one can directly compare $\mathcal{F}_{\rm eff}$: the difference is -3.3% (J), $+1.3\%$ (H) and -2.8% (K_S) thus giving an average of -1.6% which correspond to ~ 30 K, again in line with the differences discussed in Section 2.5.

[8] We have verified using our IRFM implementation that a 1% increase in infrared fluxes correspond to a decrease of 20 K in $T_{\rm eff}$.

Table A.1. Characteristic parameters of the 2MASS and TCS photometric systems. Wavelengths are in Å and the Vega's monochromatic absolute fluxes in erg cm^{-2} s^{-1} Å^{-1}.

	2MASS	TCS	Δ(%)
$\lambda_{\rm eff}$	12285	12790	
m_J	−0.001	−0.013	
$\mathcal{F}_J$	3.079	2.912	
$\mathcal{F}_{\rm eff}$	3.076	3.303	−6.9%
$\lambda_{\rm eff}$	16385	16483	
m_H	+0.019	−0.005	
$\mathcal{F}_H$	1.150	1.192	
$\mathcal{F}_{\rm eff}$	1.170	1.211	−3.4%
$\lambda_{\rm eff}$	21521	21869	
m_K	−0.017	−0.029	
$\mathcal{F}_K$	0.430	0.426	
$\mathcal{F}_{\rm eff}$	0.423	0.439	−3.6%

2MASS effective wavelengths ($\lambda_{\rm eff}$), magnitudes and fluxes are from Casagrande et al. (2006), where the latter has been modified by $-1.6, +1.5$ and $+0.3$ percent in J, H and K_S band respectively as described in Section 3.2. The TCS values are from Alonso et al. (1994b). For the TCS system $\mathcal{F}_{\rm eff}$ has been computed by shifting the value at the 2MASS effective wavelength (Figure A.1). Δ(%) is the percent decrease of the TCS $\mathcal{F}_{\rm eff}$ needed to match the 2MASS values.

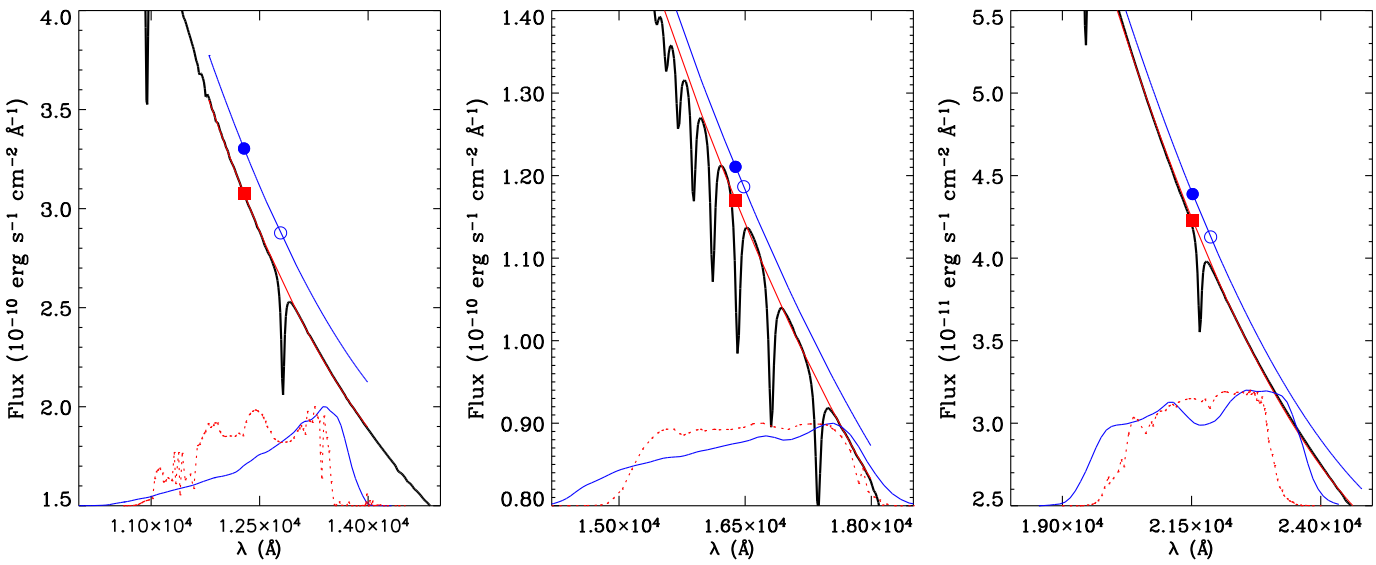

Fig. A.1. Comparison between $\mathcal{F}_{\rm eff}$ in 2MASS (filled squares) and the TCS before (open circles) and after (filled circles) correcting for the same $\lambda_{\rm eff}$. The correction has been done shifting the TCS values along the continuum of Vega, obtained by fitting a second order polynomial to the observed spectral energy distribution (from Bohlin 2007). Overplotted for comparison are the 2MASS (dotted lines) and TCS (continuous lines) filter transmission curves.

Table 8. Sample stars[a].

name	$\log g$	[Fe/H]	m_{Bol}	$T_{\rm eff}$	θ	B	V	R_C	I_C	J	H	K_S	$E(B-V)$
BD+000444	4.70	−0.01	8.802	4340 ± 74	0.254 ± 0.009	10.732	9.532	8.796	8.149	7.260	6.692	6.500	0.000
BD+002058	4.19	−1.16	10.020	6245 ± 58	0.070 ± 0.001	10.652	10.199	9.890	9.570	9.165	8.899	8.842	0.017
BD+004470	4.61	−1.53	10.351	6358 ± 61	0.058 ± 0.001	11.040	10.450	—	—	9.495	9.266	9.207	0.000
BD+012831	4.50	−1.27	10.677	5331 ± 50	0.071 ± 0.001	11.549	10.882	—	—	9.455	9.063	8.993	0.000
BD+013597	4.04	−1.87	10.809	6289 ± 63	0.048 ± 0.001	11.544	11.089	—	—	10.005	9.718	9.665	0.045
BD+023375	4.12	−2.24	9.699	6102 ± 88	0.085 ± 0.003	10.414	9.944	9.635	9.297	8.799	8.537	8.498	0.022
BD+024651	3.79	−1.78	9.980	6349 ± 67	0.069 ± 0.002	10.646	10.204	—	—	9.193	8.902	8.831	0.038
BD+030443	4.50	−0.93	9.417	4591 ± 66	0.171 ± 0.005	10.890	9.960	—	—	7.940	7.428	7.295	0.000
BD+030740	3.97	−2.70	9.584	6419 ± 83	0.081 ± 0.002	10.168	9.808	—	—	8.795	8.532	8.516	0.022
BD+040415	4.50	−0.63	9.435	4833 ± 50	0.153 ± 0.003	10.737	9.825	9.270	8.783	8.045	7.553	7.449	0.000
BD+053640	4.56	−1.22	10.154	5092 ± 57	0.099 ± 0.002	11.160	10.430	—	—	8.854	8.450	8.341	0.000
BD+054481	4.50	−0.98	9.975	5727 ± 65	0.085 ± 0.002	10.747	10.130	—	—	8.884	8.581	8.537	0.000
BD+072634	4.50	−0.66	9.595	5469 ± 64	0.111 ± 0.003	10.420	9.780	—	—	8.407	8.095	7.980	0.000
BD+074841	4.09	−1.39	10.260	6133 ± 61	0.065 ± 0.001	10.840	10.380	—	—	9.334	9.054	9.017	0.000
BD+083095	4.13	−0.78	9.855	5690 ± 58	0.091 ± 0.002	10.586	9.996	—	—	8.750	8.410	8.375	0.000
BD+090352	4.32	−2.05	9.970	6145 ± 98	0.074 ± 0.002	10.616	10.174	—	—	9.012	8.829	8.749	0.012
BD+092190	4.03	−2.54	10.971	6477 ± 75	0.042 ± 0.001	11.533	11.147	—	—	10.193	9.932	9.907	0.015
BD+092879	4.99	−0.05	10.239	4895 ± 41	0.103 ± 0.002	11.588	10.600	10.034	9.563	8.864	8.368	8.272	0.000
BD+095076	4.50	−0.08	9.340	5360 ± 49	0.130 ± 0.002	10.280	9.514	—	—	8.118	7.748	7.627	0.000
BD+100449	4.40	−1.75	10.581	5832 ± 60	0.062 ± 0.001	11.265	10.757	10.417	10.067	9.573	9.287	9.180	0.000
BD+110299	4.50	−0.87	10.474	5929 ± 55	0.063 ± 0.001	11.160	10.600	—	—	9.491	9.174	9.124	0.000
BD+110468	4.58	−1.55	10.582	5739 ± 50	0.064 ± 0.001	11.312	10.774	—	—	9.549	9.229	9.135	0.004
BD+112021	4.50	0.09	9.453	5262 ± 56	0.128 ± 0.003	10.414	9.632	9.192	8.792	8.190	7.805	7.689	0.000
BD+114725	3.59	−0.85	9.384	5476 ± 45	0.122 ± 0.002	10.193	9.548	—	—	8.223	7.856	7.757	0.000
BD+132567	4.00	−1.18	9.642	5386 ± 57	0.112 ± 0.002	10.481	9.828	9.438	9.038	8.431	8.051	8.002	0.000
BD+132698	3.98	−0.94	9.245	5824 ± 54	0.115 ± 0.002	9.956	9.376	—	—	8.187	7.900	7.844	0.000
BD+133683	3.93	−2.38	10.060	5488 ± 62	0.089 ± 0.002	11.217	10.566	10.100	9.640	9.005	8.591	8.527	0.080
BD+141947	4.50	−0.42	9.952	5131 ± 51	0.107 ± 0.002	10.980	10.180	—	—	8.659	8.200	8.137	0.000
BD+150028	4.39	−0.72	9.633	5891 ± 50	0.094 ± 0.002	10.302	9.743	—	—	8.593	8.313	8.245	0.000
BD+174708	3.87	−1.74	9.312	6120 ± 112	0.101 ± 0.003	9.922	9.476	9.183	8.854	8.435	8.108	8.075	0.010
BD+183423	4.17	−0.88	9.679	6059 ± 58	0.087 ± 0.002	10.266	9.783	—	—	8.682	8.448	8.384	0.000
BD+191730	4.40	−2.21	10.568	6210 ± 65	0.055 ± 0.001	11.178	10.736	10.436	10.136	9.692	9.414	9.396	0.000
BD+192646	4.50	−0.75	9.732	5640 ± 58	0.098 ± 0.002	10.527	9.887	—	—	8.619	8.268	8.231	0.000
BD+202030	4.00	−2.64	10.958	6496 ± 65	0.042 ± 0.001	11.580	11.200	—	—	10.220	9.980	9.937	0.024
BD+202594	4.49	−0.87	9.874	6041 ± 52	0.080 ± 0.002	10.479	9.992	—	—	8.894	8.642	8.576	0.000
BD+202972	4.00	−0.36	10.340	5681 ± 46	0.073 ± 0.001	11.070	10.450	—	—	9.220	8.890	8.826	0.000
BD+212244	4.50	−1.01	9.794	5504 ± 58	0.100 ± 0.002	10.560	9.960	—	—	8.665	8.261	8.192	0.000
BD+224454	4.49	−0.50	9.301	5326 ± 62	0.134 ± 0.003	10.270	9.500	—	—	8.048	7.707	7.611	0.000
BD+241676	3.84	−2.54	10.610	6387 ± 92	0.051 ± 0.002	11.171	10.814	—	—	9.811	9.545	9.541	0.013
BD+244460	4.38	−0.89	9.223	5160 ± 62	0.148 ± 0.004	10.235	9.463	9.018	8.609	7.931	7.513	7.461	0.000
BD+251981	3.87	−1.34	9.259	6918 ± 88	0.081 ± 0.002	9.627	9.320	—	—	8.592	8.438	8.392	0.000
BD+262251	4.18	−0.95	10.254	6049 ± 46	0.067 ± 0.001	10.846	10.370	—	—	9.290	9.022	8.963	0.000
BD+262606	4.18	−2.36	9.534	6194 ± 56	0.089 ± 0.002	10.157	9.732	—	—	8.676	8.394	8.352	0.005
BD+262621	4.00	−2.54	10.822	6336 ± 72	0.047 ± 0.001	11.428	11.023	—	—	9.994	9.749	9.731	0.009

BD+263578	3.88	−2.29	9.188	6425 ± 104	0.097 ± 0.003	9.749	9.360	—	—	8.351	8.179	8.144	0.008
BD+282137	3.99	−2.02	10.742	6257 ± 66	0.050 ± 0.001	11.303	10.898	—	—	9.861	9.621	9.560	0.006
BD+290366	4.28	−0.98	8.636	5810 ± 46	0.153 ± 0.003	9.342	8.765	—	—	7.572	7.280	7.216	0.000
BD+292091	4.58	−1.99	10.063	5974 ± 44	0.075 ± 0.001	10.740	10.240	—	—	9.104	8.805	8.739	0.004
BD+300338	4.50	−1.03	10.158	5845 ± 52	0.075 ± 0.001	10.842	10.282	—	—	9.129	8.801	8.755	0.000
BD+302130	3.30	−0.40	9.165	5690 ± 63	0.125 ± 0.003	9.910	9.290	—	—	8.031	7.772	7.677	0.000
BD+302512	4.57	−0.06	7.722	4297 ± 88	0.426 ± 0.018	9.840	8.571	—	—	6.135	5.559	5.425	0.000
BD+334737	4.50	−0.03	8.881	5420 ± 45	0.157 ± 0.003	9.840	9.040	—	—	7.658	7.316	7.218	0.000
BD+342476	3.95	−2.07	9.872	6416 ± 70	0.071 ± 0.002	10.446	10.047	—	—	9.077	8.850	8.811	0.006
BD+353659	4.50	−1.64	10.086	6023 ± 60	0.073 ± 0.002	10.761	10.243	—	—	9.124	8.871	8.798	0.000
BD+361650	4.50	−0.77	10.128	5314 ± 43	0.092 ± 0.002	11.000	10.340	—	—	8.904	8.526	8.418	0.000
BD+362165	4.40	−1.34	9.646	6328 ± 60	0.081 ± 0.002	10.194	9.766	—	—	8.791	8.552	8.498	0.000
BD+381451	4.50	−0.37	10.022	5330 ± 53	0.096 ± 0.002	10.961	10.222	—	—	8.794	8.418	8.328	0.000
BD+384955	4.60	−2.59	10.761	5265 ± 65	0.070 ± 0.002	11.684	11.024	—	—	9.540	9.217	9.088	0.000
BD+413306	4.43	−0.62	8.584	4995 ± 52	0.212 ± 0.005	9.676	8.870	8.399	7.957	7.244	6.772	6.703	0.000
BD+422667	4.26	−1.40	9.729	6133 ± 68	0.083 ± 0.002	10.328	9.854	—	—	8.822	8.517	8.491	0.000
BD+423607	4.59	−2.06	9.889	6021 ± 46	0.080 ± 0.001	10.620	10.110	—	—	8.973	8.670	8.587	0.018
BD+441910	3.96	−2.14	10.760	6232 ± 61	0.050 ± 0.001	11.350	10.930	—	—	9.911	9.642	9.599	0.000
BD+511696	4.50	−1.48	9.757	5726 ± 55	0.094 ± 0.002	10.484	9.916	9.562	9.201	8.678	8.375	8.306	0.000
BD+592723	4.32	−1.69	10.222	6187 ± 80	0.065 ± 0.002	10.941	10.491	—	—	9.380	9.059	9.056	0.034
BD+660268	4.55	−2.11	9.678	5415 ± 47	0.109 ± 0.002	10.563	9.906	—	—	8.535	8.165	8.069	0.000
BD+710031	4.05	−1.98	9.988	6430 ± 74	0.067 ± 0.002	10.608	10.205	—	—	9.233	8.947	8.904	0.027
BD+800245	3.17	−1.88	9.820	5527 ± 62	0.098 ± 0.002	10.563	10.022	9.662	9.262	8.711	8.333	8.261	0.000
BD-012457	4.50	−0.89	9.217	4525 ± 47	0.193 ± 0.004	10.854	9.799	—	—	7.759	7.155	7.054	0.000
BD-01306	4.67	−0.96	8.961	5782 ± 58	0.133 ± 0.003	9.667	9.084	8.743	8.388	7.899	7.589	7.520	0.000
BD-032525	4.14	−1.97	9.499	6012 ± 55	0.096 ± 0.002	10.152	9.671	—	—	8.561	8.276	8.205	0.000
BD-043208	3.99	−2.29	9.790	6492 ± 89	0.072 ± 0.002	10.375	9.977	9.709	9.417	9.064	8.798	8.739	0.009
BD-044778	4.50	−0.57	10.190	4903 ± 65	0.105 ± 0.003	11.410	10.510	—	—	8.863	8.307	8.202	0.000
BD-093102	4.50	−0.75	10.315	5424 ± 60	0.081 ± 0.002	11.184	10.503	10.103	9.723	9.124	8.768	8.699	0.000
BD-100388	3.98	−2.32	10.171	6260 ± 61	0.065 ± 0.001	10.780	10.350	—	—	9.317	9.060	8.997	0.009
BD-114126	4.30	0.20	9.985	4789 ± 44	0.121 ± 0.002	11.406	10.383	9.798	9.316	8.578	8.065	7.948	0.000
BD-133442	3.92	−2.74	10.085	6434 ± 80	0.064 ± 0.002	10.655	10.266	9.994	9.704	9.293	9.034	9.018	0.011
BS16023-0046	4.50	−2.91	14.040	6548 ± 75	0.010 ± 0.001	14.548	14.170	—	—	13.241	13.016	12.964	0.004
BS16545-0089	3.90	−3.49	14.255	6568 ± 83	0.009 ± 0.001	14.768	14.450	—	—	13.516	13.267	13.202	0.023
BS16968-0061	3.88	−3.07	13.086	6256 ± 64	0.017 ± 0.001	13.690	13.260	—	—	12.214	11.929	11.866	0.019
BS17570-0063	4.72	−2.91	14.194	6319 ± 80	0.010 ± 0.001	14.840	14.510	—	—	13.468	13.172	13.073	0.026
CD-2417504	4.21	−3.29	11.866	6455 ± 62	0.028 ± 0.001	12.510	12.092	11.840	11.530	11.121	10.874	10.807	0.020
CD-3018140	4.13	−1.90	9.753	6373 ± 74	0.076 ± 0.002	10.365	9.946	9.663	9.353	8.955	8.693	8.655	0.012
CD-3301173	4.29	−3.01	10.774	6548 ± 68	0.045 ± 0.001	11.300	10.940	10.690	10.410	10.008	9.790	9.745	0.007
CD-333337	4.03	−1.32	8.969	6001 ± 64	0.123 ± 0.003	9.581	9.109	8.814	8.490	8.007	7.715	7.666	0.007
CD-350360	4.53	−1.15	10.034	5235 ± 58	0.099 ± 0.002	11.024	10.266	9.824	9.389	8.820	8.362	8.281	0.000
CD-3514849	4.22	−2.35	10.401	6396 ± 65	0.056 ± 0.001	10.969	10.565	10.290	9.980	9.590	9.355	9.293	0.002
CD-4106367	4.50	−0.32	9.533	5228 ± 56	0.125 ± 0.003	10.523	9.738	9.301	8.893	8.286	7.880	7.757	0.000
CD-4214278	4.39	−2.03	9.981	6170 ± 63	0.073 ± 0.002	10.680	10.220	9.890	9.560	9.132	8.825	8.770	0.020
CD-4802445	4.25	−1.93	10.362	6453 ± 66	0.056 ± 0.001	10.935	10.541	10.280	9.980	9.586	9.335	9.288	0.015
CD-7101234	4.29	−2.41	10.207	6408 ± 69	0.061 ± 0.001	10.850	10.440	10.160	9.840	9.461	9.183	9.114	0.020
CS22166-0030	4.00	−3.36	13.371	6039 ± 59	0.016 ± 0.001	14.090	13.620	—	—	12.484	12.149	12.099	0.019

CS22177-0009	4.60	−3.03	13.917	6422 ± 75	0.011 ± 0.001	14.671	14.270	—	—	13.222	12.986	12.953	0.023
CS22876-0032	4.40	−3.70	12.630	6251 ± 56	0.021 ± 0.001	13.250	12.840	12.560	12.250	11.802	11.555	11.485	0.001
CS22884-0108	4.22	−3.21	13.917	5907 ± 52	0.013 ± 0.001	14.744	14.240	—	—	12.996	12.679	12.588	0.033
CS22888-0031	5.12	−3.19	14.669	6334 ± 89	0.008 ± 0.001	15.313	14.900	—	—	13.897	13.579	13.583	0.007
CS22948-0093	4.40	−3.43	15.107	6611 ± 114	0.006 ± 0.001	15.536	15.180	—	—	14.290	13.985	14.005	0.013
CS22953-0037	4.23	−2.86	13.486	6524 ± 98	0.013 ± 0.001	14.007	13.640	—	—	12.683	12.444	12.461	0.008
CS22965-0054	3.90	−2.84	14.648	6364 ± 86	0.008 ± 0.001	15.566	15.069	—	—	13.861	13.583	13.449	0.110
CS22966-0011	4.78	−3.04	14.431	6308 ± 110	0.009 ± 0.001	14.977	14.555	—	—	13.543	13.231	13.279	0.000
CS29518-0020	4.70	−2.70	13.888	6465 ± 84	0.011 ± 0.001	14.418	14.003	—	—	13.060	12.763	12.745	0.009
CS29518-0043	4.25	−3.18	14.291	6515 ± 96	0.009 ± 0.001	14.937	14.566	—	—	13.643	13.355	13.372	0.008
CS29527-0015	4.17	−3.43	14.048	6535 ± 82	0.010 ± 0.001	14.660	14.260	—	—	13.298	13.080	13.048	0.014
CS31061-0032	4.25	−2.61	13.722	6431 ± 82	0.012 ± 0.001	14.283	13.874	13.581	13.290	12.871	12.617	12.610	0.015
G004-037	4.19	−2.70	11.064	6340 ± 62	0.042 ± 0.001	11.883	11.415	—	—	10.324	10.032	9.974	0.053
G008-050	4.50	−1.20	12.081	4597 ± 59	0.050 ± 0.001	13.640	12.630	—	—	10.640	10.100	9.998	0.000
G009-031	4.46	−0.92	10.672	5711 ± 52	0.062 ± 0.001	11.430	10.830	—	—	9.595	9.302	9.200	0.000
G009-036	4.35	−1.04	11.811	5766 ± 51	0.036 ± 0.001	12.520	11.950	—	—	10.745	10.426	10.378	0.000
G011-044	4.43	−2.06	10.887	6309 ± 64	0.046 ± 0.001	11.510	11.070	10.770	10.450	10.032	9.807	9.740	0.006
G012-023	4.50	−1.13	13.160	5533 ± 49	0.021 ± 0.001	14.021	13.382	—	—	12.068	11.715	11.644	0.000
G014-039	4.50	−1.96	12.414	4702 ± 50	0.041 ± 0.001	13.778	12.861	—	—	11.056	10.530	10.413	0.000
G014-045	4.43	−1.36	10.309	4559 ± 60	0.115 ± 0.003	11.852	10.842	10.221	9.673	8.863	8.307	8.172	0.000
G015-023	4.50	−1.33	10.723	5274 ± 56	0.071 ± 0.002	11.665	10.960	—	—	9.513	9.092	9.037	0.000
G015-024	4.50	−1.40	11.287	5693 ± 49	0.047 ± 0.001	12.005	11.435	11.085	10.725	10.206	9.891	9.794	0.000
G018-054	3.93	−1.33	10.489	6005 ± 57	0.061 ± 0.001	11.182	10.697	10.370	10.030	9.557	9.236	9.178	0.028
G021-006	4.57	0.00	11.627	4442 ± 51	0.066 ± 0.002	13.380	12.348	—	—	10.137	9.528	9.417	0.000
G021-022	4.28	−0.88	10.625	5918 ± 51	0.059 ± 0.001	11.265	10.738	10.398	10.058	9.597	9.304	9.252	0.000
G023-020	4.50	−1.58	11.379	5350 ± 60	0.051 ± 0.001	12.234	11.596	—	—	10.147	9.803	9.720	0.000
G024-003	4.27	−1.59	10.270	6118 ± 59	0.065 ± 0.001	10.928	10.457	—	—	9.353	9.101	9.020	0.014
G039-036	4.00	−2.50	11.600	4575 ± 80	0.063 ± 0.002	13.420	12.360	—	—	10.247	9.761	9.538	0.084
G044-030	4.50	−0.93	11.109	5483 ± 57	0.055 ± 0.001	11.940	11.296	10.896	10.506	9.970	9.580	9.518	0.000
G046-005	4.83	−1.41	11.037	5089 ± 52	0.066 ± 0.001	12.055	11.315	—	—	9.737	9.343	9.233	0.000
G046-031	4.31	−0.78	10.743	5965 ± 55	0.055 ± 0.001	11.388	10.854	10.534	10.204	9.747	9.489	9.393	0.000
G053-041	4.25	−1.26	10.920	6006 ± 49	0.050 ± 0.001	11.520	11.040	—	—	9.932	9.658	9.595	0.000
G055-017	4.50	−1.48	12.972	5405 ± 53	0.024 ± 0.001	13.865	13.195	—	—	11.821	11.429	11.368	0.000
G056-022	4.50	−0.89	13.207	4827 ± 50	0.027 ± 0.001	14.477	13.611	—	—	11.840	11.322	11.250	0.000
G059-024	4.36	−2.38	11.796	6235 ± 70	0.031 ± 0.001	12.437	12.013	—	—	10.970	10.662	10.642	0.011
G060-048	4.30	−1.74	11.140	5953 ± 66	0.046 ± 0.001	11.808	11.321	11.001	10.651	10.217	9.871	9.826	0.000
G062-040	4.50	−2.05	13.284	5030 ± 57	0.024 ± 0.001	14.308	13.573	—	—	11.962	11.554	11.461	0.000
G063-026	4.30	−1.47	12.033	6104 ± 57	0.029 ± 0.001	12.638	12.189	—	—	11.109	10.855	10.793	0.000
G064-012	4.18	−3.26	11.255	6464 ± 61	0.037 ± 0.001	11.838	11.453	11.186	10.893	10.509	10.268	10.208	0.003
G064-037	4.22	−3.17	10.900	6584 ± 72	0.042 ± 0.001	11.493	11.123	10.860	10.560	10.188	9.956	9.923	0.012
G065-022	4.25	−1.63	11.309	5099 ± 58	0.058 ± 0.001	12.313	11.573	—	—	10.034	9.641	9.477	0.000
G066-018	4.50	−0.35	12.648	4755 ± 51	0.036 ± 0.001	13.960	13.100	—	—	11.251	10.701	10.629	0.000
G075-031	4.39	−1.00	10.366	6177 ± 59	0.061 ± 0.001	10.990	10.528	10.180	9.860	9.473	9.195	9.131	0.008
G086-039	4.00	−1.79	11.170	4862 ± 48	0.068 ± 0.001	12.380	11.540	—	—	9.818	9.348	9.247	0.000
G088-010	4.00	−2.70	11.532	6327 ± 61	0.034 ± 0.001	12.310	11.870	—	—	10.759	10.460	10.405	0.060
G089-014	4.50	−1.69	10.234	6076 ± 56	0.067 ± 0.001	10.866	10.400	10.090	9.740	9.316	9.024	8.970	0.000
G090-036	4.13	−1.75	12.500	5579 ± 47	0.028 ± 0.001	13.270	12.690	—	—	11.382	11.046	10.962	0.000

G092-049	4.60	−2.46	11.695	4512 ± 97	0.062 ± 0.003	13.283	12.255	—	—	10.185	9.774	9.653	0.000
G098-056	4.50	−1.24	11.179	5603 ± 59	0.051 ± 0.001	11.990	11.360	—	—	10.068	9.719	9.677	0.000
G115-049	4.75	−2.11	11.364	5988 ± 49	0.041 ± 0.001	12.110	11.600	—	—	10.456	10.144	10.090	0.011
G115-058	4.40	−1.61	11.934	6245 ± 52	0.029 ± 0.001	12.550	12.100	—	—	11.086	10.833	10.779	0.000
G126-063	4.50	−1.36	12.032	5905 ± 59	0.031 ± 0.001	12.715	12.148	11.808	11.458	11.026	10.707	10.626	0.000
G128-036	4.50	−0.94	11.369	4904 ± 49	0.061 ± 0.001	12.520	11.720	—	—	10.066	9.536	9.429	0.000
G130-036	4.25	−1.72	10.782	4647 ± 51	0.089 ± 0.002	12.200	11.280	—	—	9.372	8.859	8.743	0.000
G130-065	4.50	−2.24	11.431	6207 ± 53	0.037 ± 0.001	12.050	11.620	—	—	10.582	10.302	10.256	0.000
G152-035	4.50	−1.75	11.930	5610 ± 53	0.036 ± 0.001	12.685	12.120	—	—	10.814	10.493	10.419	0.000
G161-082	4.50	−1.38	11.792	5493 ± 57	0.040 ± 0.001	12.588	11.988	11.608	11.208	10.630	10.300	10.222	0.000
G161-084	4.75	−1.31	11.784	4737 ± 38	0.054 ± 0.001	13.090	12.200	—	—	10.381	9.864	9.734	0.000
G167-011	4.50	−0.14	14.149	4759 ± 54	0.018 ± 0.001	15.565	14.635	—	—	12.773	12.254	12.169	0.000
G178-030	4.50	0.00	13.125	4831 ± 45	0.028 ± 0.001	14.390	13.520	—	—	11.728	11.242	11.108	0.000
G178-041	4.50	−2.54	12.422	6010 ± 53	0.025 ± 0.001	13.145	12.660	—	—	11.530	11.238	11.184	0.000
G180-058	4.16	−2.01	11.078	5332 ± 57	0.059 ± 0.001	12.002	11.319	10.884	10.468	9.901	9.507	9.397	0.000
G192-043	4.50	−1.45	10.058	6474 ± 65	0.064 ± 0.001	10.754	10.324	—	—	9.301	9.054	9.001	0.045
G195-034	4.30	−1.79	11.663	6139 ± 58	0.034 ± 0.001	12.260	11.794	—	—	10.750	10.457	10.405	0.000
G196-047	4.69	−1.38	12.444	5552 ± 73	0.029 ± 0.001	13.191	12.588	—	—	11.282	10.987	10.831	0.000
G197-008	4.40	−0.39	11.974	5632 ± 54	0.035 ± 0.001	12.740	12.110	—	—	10.850	10.495	10.455	0.000
G201-005	3.79	−2.51	11.331	6351 ± 87	0.037 ± 0.001	11.917	11.507	—	—	10.528	10.244	10.247	0.005
G206-034	4.18	−2.53	11.139	6385 ± 64	0.040 ± 0.001	11.809	11.388	—	—	10.358	10.085	10.044	0.029
G255-032	4.61	−1.82	11.406	5859 ± 54	0.042 ± 0.001	12.129	11.645	—	—	10.439	10.118	10.070	0.010
HD10002	4.45	0.20	7.970	5267 ± 56	0.253 ± 0.006	9.000	8.140	7.690	7.300	6.684	6.336	6.211	0.000
HD102200	4.20	−1.24	8.609	6155 ± 67	0.138 ± 0.003	9.189	8.739	8.449	8.141	7.688	7.449	7.383	0.005
HD102634	4.18	0.20	6.138	6316 ± 102	0.409 ± 0.014	6.665	6.145	—	—	5.212	5.081	4.921	0.000
HD103072	4.60	−0.30	8.118	5060 ± 50	0.256 ± 0.005	9.250	8.400	7.899	7.473	6.785	6.358	6.268	0.000
HD104636	4.00	0.14	8.222	6705 ± 73	0.139 ± 0.003	8.590	8.220	—	—	7.420	7.294	7.226	0.000
HD105601	4.00	0.00	7.405	7233 ± 99	0.174 ± 0.005	7.681	7.382	—	—	6.776	6.713	6.665	0.000
HD105671	4.50	0.20	7.914	4616 ± 49	0.338 ± 0.008	9.575	8.440	7.780	7.235	6.441	5.913	5.763	0.000
HD105755	3.92	−0.79	8.463	5840 ± 52	0.164 ± 0.003	9.110	8.590	—	—	7.414	7.126	7.062	0.000
HD105837	4.54	−0.51	7.437	5966 ± 56	0.252 ± 0.005	8.088	7.528	7.202	6.878	6.421	6.143	6.097	0.000
HD106038	4.36	−1.33	10.016	6121 ± 61	0.073 ± 0.002	10.627	10.153	9.857	9.529	9.107	8.834	8.761	0.003
HD106156	4.58	0.23	7.785	5442 ± 51	0.258 ± 0.005	8.718	7.918	7.492	7.127	6.571	6.226	6.125	0.000
HD106516	4.40	−0.78	6.023	6317 ± 117	0.431 ± 0.016	6.570	6.104	5.818	5.533	5.132	5.004	4.839	0.000
HD107213	4.08	0.20	6.347	6236 ± 84	0.381 ± 0.011	6.897	6.377	—	—	5.364	5.220	5.131	0.000
HD107906	4.00	0.00	8.732	5224 ± 47	0.181 ± 0.003	9.737	8.930	—	—	7.456	7.072	6.968	0.000
HD108177	4.41	−1.64	9.487	6333 ± 68	0.087 ± 0.002	10.082	9.647	9.362	9.052	8.673	8.404	8.354	0.003
HD10853	4.74	−0.74	8.405	4638 ± 72	0.267 ± 0.008	9.950	8.910	8.285	7.748	6.929	6.437	6.319	0.000
HD108564	4.67	−1.18	8.967	4662 ± 49	0.204 ± 0.004	10.414	9.450	8.853	8.318	7.554	6.994	6.896	0.000
HD108754	4.53	−0.58	8.858	5415 ± 44	0.159 ± 0.003	9.735	9.032	—	—	7.660	7.295	7.201	0.000
HD109200	4.47	−0.24	6.913	5147 ± 66	0.431 ± 0.011	7.991	7.143	6.663	6.247	5.626	5.231	5.067	0.000
HD11020	4.62	−0.28	8.787	5292 ± 52	0.172 ± 0.004	9.790	8.980	8.537	8.132	7.553	7.133	7.056	0.000
HD110621	4.08	−1.59	9.753	6174 ± 94	0.081 ± 0.003	10.385	9.932	9.628	9.313	8.852	8.543	8.566	0.013
HD11130	4.65	−0.57	7.865	5223 ± 45	0.270 ± 0.005	8.828	8.070	7.640	7.237	6.599	6.195	6.108	0.000
HD112099	4.56	0.09	8.002	5089 ± 55	0.267 ± 0.006	9.102	8.250	7.770	7.345	6.661	6.267	6.151	0.000
HD112758	4.53	−0.49	7.311	5174 ± 51	0.355 ± 0.007	8.335	7.549	7.099	6.669	6.040	5.597	5.529	0.000
HD113101	4.55	0.06	8.833	5498 ± 50	0.156 ± 0.003	9.710	8.976	—	—	7.631	7.309	7.223	0.000

HD11373	4.63	−0.45	8.042	4749 ± 57	0.301 ± 0.007	9.503	8.483	7.876	7.387	6.614	6.105	6.017	0.000
HD114094	4.45	−0.24	9.551	5654 ± 55	0.106 ± 0.002	10.364	9.668	9.283	8.922	8.431	8.090	8.016	0.000
HD114606	4.28	−0.48	8.616	5689 ± 68	0.161 ± 0.004	9.363	8.743	8.383	8.013	7.534	7.219	7.088	0.000
HD114762	4.13	−0.73	7.181	5920 ± 57	0.288 ± 0.006	7.833	7.283	6.967	6.629	6.145	5.888	5.813	0.000
HD115589	4.55	0.31	9.497	5017 ± 80	0.138 ± 0.005	10.700	9.800	—	—	8.089	7.731	7.623	0.000
HD116064	4.44	−1.87	8.674	5895 ± 58	0.146 ± 0.003	9.282	8.833	8.520	8.189	7.698	7.372	7.306	0.000
HD117126	4.34	−0.03	7.347	5737 ± 54	0.284 ± 0.006	8.080	7.440	—	—	6.254	5.950	5.845	0.000
HD118981	4.50	−0.26	8.116	5923 ± 60	0.187 ± 0.004	8.780	8.210	—	—	7.095	6.789	6.750	0.000
HD119173	4.46	−0.62	8.733	5982 ± 55	0.138 ± 0.003	9.380	8.828	8.503	8.176	7.730	7.460	7.390	0.000
HD120467	4.50	0.24	7.449	4408 ± 48	0.459 ± 0.010	9.440	8.170	7.415	6.775	5.919	5.323	5.160	0.000
HD120559	4.57	−0.94	7.811	5452 ± 52	0.254 ± 0.005	8.630	7.971	7.595	7.216	6.633	6.271	6.195	0.000
HD120780	4.50	−0.17	7.088	5050 ± 50	0.413 ± 0.008	8.270	7.370	6.875	6.395	5.782	5.318	5.190	0.000
HD122196	3.71	−1.82	8.593	5986 ± 63	0.147 ± 0.003	9.212	8.753	8.444	8.112	7.629	7.361	7.275	0.004
HD123710	4.26	−0.55	8.095	5770 ± 54	0.199 ± 0.004	8.800	8.210	—	—	6.999	6.703	6.650	0.000
HD124106	4.58	−0.10	7.690	5108 ± 53	0.306 ± 0.007	8.807	7.938	7.458	7.032	6.360	5.949	5.861	0.000
HD126053	4.40	−0.38	6.166	5693 ± 93	0.497 ± 0.017	6.905	6.269	5.904	5.554	5.053	4.814	4.644	0.000
HD12661	4.35	0.36	7.386	5598 ± 71	0.293 ± 0.008	8.240	7.500	—	—	6.182	5.896	5.861	0.000
HD126681	4.55	−1.14	9.154	5638 ± 50	0.128 ± 0.002	9.897	9.296	8.937	8.569	8.044	7.709	7.631	0.000
HD127506	4.70	−0.40	8.228	4668 ± 83	0.286 ± 0.010	9.731	8.702	8.078	7.577	6.756	6.308	6.135	0.000
HD128429	4.06	−0.20	6.173	6457 ± 70	0.385 ± 0.009	6.662	6.200	—	—	5.335	5.115	5.053	0.000
HD129518	4.44	−0.34	8.754	6280 ± 73	0.124 ± 0.003	9.292	8.809	8.521	8.234	7.866	7.623	7.540	0.000
HD130307	4.62	−0.16	7.484	5037 ± 49	0.346 ± 0.007	8.657	7.761	7.261	6.826	6.151	5.688	5.615	0.000
HD130322	4.48	0.03	7.897	5432 ± 58	0.246 ± 0.005	8.832	8.046	7.623	7.242	6.712	6.315	6.234	0.000
HD130871	4.71	−0.16	8.698	4854 ± 48	0.213 ± 0.004	10.045	9.073	8.520	8.043	7.313	6.802	6.723	0.000
HD130930	4.45	0.01	8.410	4991 ± 54	0.230 ± 0.005	9.643	8.707	8.188	7.741	7.038	6.598	6.514	0.000
HD130992	4.32	−0.06	7.404	4802 ± 47	0.395 ± 0.008	8.818	7.804	7.221	6.735	5.990	5.493	5.385	0.000
HD131653	4.65	−0.63	9.345	5416 ± 61	0.127 ± 0.003	10.238	9.518	—	—	8.154	7.802	7.680	0.000
HD13201	4.28	−0.33	6.354	6406 ± 60	0.360 ± 0.008	6.835	6.410	—	—	5.485	5.294	5.217	0.000
HD132142	4.50	−0.54	7.543	5232 ± 52	0.312 ± 0.006	8.539	7.770	7.321	6.904	6.268	5.893	5.798	0.000
HD132475	3.87	−1.51	8.321	5808 ± 57	0.177 ± 0.004	9.100	8.563	8.216	7.855	7.327	6.996	6.912	0.030
HD13403	4.00	−0.31	6.867	5630 ± 62	0.368 ± 0.009	7.647	7.000	—	—	5.727	5.374	5.347	0.000
HD134169	3.95	−0.81	7.559	5920 ± 76	0.242 ± 0.006	8.193	7.663	7.342	7.011	6.553	6.287	6.160	0.000
HD134439	4.52	−1.50	8.853	5026 ± 91	0.185 ± 0.007	9.881	9.118	8.661	8.220	7.526	7.176	6.978	0.000
HD134440	4.61	−1.45	9.097	4899 ± 48	0.174 ± 0.004	10.289	9.420	8.923	8.445	7.761	7.275	7.147	0.000
HD1368	4.37	−0.91	8.784	6022 ± 65	0.133 ± 0.003	9.420	8.890	—	—	7.797	7.552	7.463	0.000
HD136834	4.17	0.19	7.974	4958 ± 53	0.285 ± 0.006	9.273	8.281	7.733	7.295	6.596	6.175	6.038	0.000
HD13783	4.30	−0.62	8.155	5566 ± 56	0.208 ± 0.004	8.969	8.297	—	—	7.043	6.658	6.585	0.000
HD138290	4.20	−0.07	6.555	6909 ± 79	0.282 ± 0.007	6.930	6.560	—	—	5.833	5.721	5.664	0.000
HD139798	4.23	−0.16	5.726	6741 ± 90	0.434 ± 0.013	6.113	5.761	—	—	4.929	4.834	4.754	0.000
HD140283	3.62	−2.39	7.018	5777 ± 55	0.326 ± 0.007	7.692	7.205	6.876	6.522	6.014	5.696	5.588	0.000
HD142709	4.60	−0.17	7.495	4533 ± 51	0.425 ± 0.010	9.180	8.060	7.390	6.825	6.032	5.452	5.284	0.000
HD144061	4.43	−0.26	7.137	5620 ± 60	0.326 ± 0.007	7.916	7.262	—	—	6.023	5.645	5.606	0.000
HD144515	3.64	−1.03	7.963	4944 ± 41	0.288 ± 0.005	9.060	8.275	—	—	6.628	6.151	6.026	0.000
HD144579	4.75	−0.69	6.471	5249 ± 69	0.508 ± 0.014	7.394	6.660	6.258	5.872	5.182	4.824	4.755	0.000
HD144628	4.50	−0.33	6.850	5083 ± 46	0.455 ± 0.009	7.970	7.110	6.630	6.185	5.546	5.102	4.981	0.000
HD144872	4.65	−0.64	8.177	4790 ± 59	0.278 ± 0.007	9.543	8.580	8.012	7.542	6.756	6.288	6.162	0.000
HD145417	4.62	−1.39	7.221	4916 ± 46	0.410 ± 0.008	8.360	7.530	7.050	6.590	5.888	5.395	5.293	0.000

HD1461	4.35	0.24	6.389	5827 ± 88	0.428 ± 0.013	7.133	6.453	6.083	5.743	5.329	5.041	4.897	0.000
HD147776	4.72	−0.29	8.037	4762 ± 44	0.300 ± 0.006	9.390	8.420	7.882	7.400	6.619	6.108	6.000	0.000
HD148816	4.13	−0.75	7.173	5920 ± 54	0.289 ± 0.006	7.820	7.283	6.950	6.623	6.159	5.862	5.809	0.000
HD149414	4.60	−1.26	9.335	5098 ± 51	0.144 ± 0.003	10.353	9.607	9.160	8.707	8.055	7.637	7.517	0.000
HD150177	3.96	−0.60	6.289	6070 ± 69	0.413 ± 0.010	6.856	6.370	—	—	5.353	5.064	4.977	0.000
HD150682	3.81	0.00	5.931	6576 ± 85	0.415 ± 0.012	6.324	5.934	—	—	5.141	4.938	4.859	0.000
HD154363	4.66	−0.51	7.036	4351 ± 84	0.570 ± 0.022	8.892	7.733	7.008	6.377	5.522	4.942	4.726	0.000
HD154577	4.73	−0.63	7.057	4884 ± 41	0.448 ± 0.008	8.285	7.395	6.880	6.415	5.694	5.204	5.091	0.000
HD157089	4.07	−0.59	6.864	5743 ± 64	0.354 ± 0.008	7.549	6.968	6.638	6.303	5.754	5.477	5.416	0.000
HD157948	4.00	−0.55	7.856	5158 ± 58	0.278 ± 0.006	8.855	8.095	—	—	6.542	6.165	6.075	0.000
HD158809	3.87	−0.69	7.993	5567 ± 49	0.224 ± 0.004	8.804	8.145	—	—	6.854	6.518	6.435	0.000
HD159222	4.30	0.10	6.456	5786 ± 50	0.421 ± 0.008	7.178	6.541	—	—	5.342	5.076	4.998	0.000
HD159868	3.96	−0.08	7.112	5519 ± 63	0.342 ± 0.008	7.967	7.245	6.852	6.481	5.941	5.567	5.535	0.000
HD16031	4.17	−1.74	9.622	6286 ± 64	0.083 ± 0.002	10.197	9.770	9.484	9.184	8.790	8.516	8.457	0.003
HD160617	3.73	−1.78	8.578	6048 ± 65	0.145 ± 0.003	9.188	8.740	8.431	8.108	7.628	7.365	7.311	0.005
HD160693	4.21	−0.56	8.264	5901 ± 51	0.176 ± 0.003	8.957	8.375	—	—	7.226	6.957	6.896	0.000
HD161848	4.59	−0.39	8.662	5102 ± 64	0.196 ± 0.005	9.735	8.912	8.438	8.014	7.337	6.959	6.822	0.000
HD163810	3.65	−1.34	9.428	5512 ± 61	0.118 ± 0.003	10.272	9.660	9.280	8.897	8.313	7.972	7.843	0.020
HD16623	4.26	−0.60	8.652	5865 ± 77	0.149 ± 0.004	9.360	8.760	8.425	8.090	7.622	7.299	7.276	0.000
HD166913	4.31	−1.56	8.078	6267 ± 62	0.170 ± 0.004	8.665	8.216	7.926	7.614	7.200	6.947	6.920	0.000
HD167858	4.26	−0.21	6.613	7184 ± 104	0.254 ± 0.008	6.930	6.620	—	—	6.031	5.878	5.835	0.000
HD168009	4.21	−0.02	6.205	5801 ± 50	0.470 ± 0.009	6.930	6.295	—	—	5.120	4.836	4.756	0.000
HD170493	4.49	0.15	7.564	4682 ± 91	0.386 ± 0.015	9.142	8.036	7.405	6.900	6.069	5.643	5.484	0.000
HD171620	4.15	−0.50	7.477	6122 ± 72	0.235 ± 0.006	8.067	7.567	—	—	6.496	6.267	6.241	0.000
HD17190	4.40	−0.11	7.684	5149 ± 66	0.302 ± 0.008	8.705	7.878	7.460	7.056	6.367	6.000	5.874	0.000
HD172323	4.35	−0.11	7.991	5910 ± 57	0.199 ± 0.004	8.641	8.074	—	—	6.932	6.693	6.598	0.000
HD173417	3.82	0.00	5.715	6782 ± 111	0.431 ± 0.015	6.050	5.720	—	—	4.903	4.842	4.776	0.000
HD175617	4.63	−0.46	9.949	5567 ± 55	0.091 ± 0.002	10.809	10.095	—	—	8.796	8.447	8.395	0.000
HD178428	4.26	0.14	5.974	5656 ± 70	0.550 ± 0.014	6.783	6.074	—	—	4.812	4.562	4.430	0.000
HD179626	4.02	−1.12	8.998	5986 ± 60	0.122 ± 0.003	9.710	9.188	8.849	8.502	8.046	7.748	7.680	0.018
HD179949	4.43	0.22	6.225	6205 ± 104	0.407 ± 0.014	6.780	6.240	5.933	5.645	5.296	5.101	4.936	0.000
HD181234	4.27	0.38	8.327	5554 ± 89	0.193 ± 0.006	9.400	8.400	—	—	7.152	6.871	6.689	0.000
HD181743	4.48	−1.78	9.516	6151 ± 56	0.091 ± 0.002	10.140	9.683	9.375	9.062	8.624	8.348	8.274	0.007
HD182807	4.21	−0.33	6.102	6154 ± 100	0.438 ± 0.015	6.694	6.185	—	—	5.080	4.931	4.858	0.000
HD1835	4.43	0.14	6.324	5847 ± 94	0.438 ± 0.015	7.048	6.389	6.029	5.699	5.253	5.035	4.861	0.000
HD183735	4.56	−1.27	9.832	6767 ± 173	0.065 ± 0.003	10.870	9.900	—	—	9.027	9.006	8.956	0.000
HD184400	4.00	0.04	8.496	6534 ± 98	0.129 ± 0.004	8.975	8.515	—	—	7.612	7.497	7.460	0.000
HD184499	4.01	−0.62	6.515	5812 ± 48	0.406 ± 0.007	7.211	6.628	—	—	5.452	5.166	5.079	0.000
HD18632	4.60	0.18	7.715	4997 ± 79	0.316 ± 0.010	8.938	8.020	7.491	7.052	6.323	5.951	5.841	0.000
HD186427	4.37	0.06	6.120	5748 ± 56	0.498 ± 0.010	6.877	6.215	—	—	4.993	4.695	4.651	0.000
HD188031	4.16	−1.72	9.937	6411 ± 89	0.069 ± 0.002	10.557	10.130	9.841	9.546	9.163	8.864	8.857	0.016
HD188262	4.50	−1.65	7.283	4721 ± 63	0.432 ± 0.012	8.490	7.740	—	—	5.861	5.413	5.259	0.000
HD188510	4.60	−1.54	8.674	5562 ± 52	0.164 ± 0.003	9.452	8.851	8.486	8.100	7.570	7.221	7.125	0.000
HD189558	3.77	−1.12	7.603	5765 ± 57	0.250 ± 0.005	8.299	7.740	7.392	7.034	6.533	6.214	6.164	0.000
HD190007	4.26	0.15	6.939	4640 ± 51	0.524 ± 0.012	8.600	7.460	6.790	6.255	5.476	4.956	4.796	0.000
HD190404	4.27	−0.74	6.981	5004 ± 54	0.442 ± 0.010	8.092	7.276	—	—	5.671	5.172	5.113	0.000
HD192263	4.58	0.05	7.484	4958 ± 56	0.357 ± 0.008	8.730	7.790	—	—	6.115	5.685	5.537	0.000

HD192961	4.31	−0.35	8.055	4435 ± 86	0.343 ± 0.014	9.894	8.717	8.004	7.411	6.524	5.999	5.785	0.000
HD193901	4.52	−1.07	8.512	5920 ± 52	0.156 ± 0.003	9.183	8.644	8.307	7.964	7.500	7.219	7.144	0.002
HD19445	4.46	−2.01	7.861	6135 ± 60	0.196 ± 0.004	8.503	8.026	7.737	7.394	6.948	6.696	6.640	0.000
HD194598	4.37	−1.12	8.247	6118 ± 57	0.165 ± 0.003	8.844	8.356	8.055	7.739	7.326	7.039	6.982	0.000
HD196310	4.31	−0.05	7.983	6865 ± 90	0.148 ± 0.004	8.360	7.980	—	—	7.245	7.146	7.046	0.000
HD197076	4.42	−0.12	6.360	5825 ± 110	0.434 ± 0.017	7.060	6.446	—	—	5.252	5.085	4.921	0.000
HD198802	3.96	0.04	6.295	5750 ± 53	0.459 ± 0.009	7.040	6.373	6.013	5.663	5.199	4.904	4.803	0.000
HD199289	4.40	−1.01	8.173	5975 ± 59	0.179 ± 0.004	8.803	8.287	7.972	7.643	7.178	6.920	6.841	0.000
HD199611	3.83	0.00	5.822	6877 ± 82	0.399 ± 0.011	6.130	5.818	—	—	5.092	4.963	4.923	0.000
HD200077	4.00	−0.14	6.496	5903 ± 54	0.397 ± 0.008	7.134	6.578	—	—	5.450	5.158	5.119	0.000
HD200580	3.90	−0.62	7.205	5817 ± 56	0.295 ± 0.006	7.864	7.324	—	—	6.135	5.842	5.790	0.000
HD200779	4.10	0.06	7.571	4434 ± 66	0.429 ± 0.013	9.490	8.270	7.530	6.905	6.040	5.485	5.306	0.000
HD201889	4.09	−0.88	7.907	5691 ± 53	0.223 ± 0.004	8.643	8.055	—	—	6.808	6.484	6.435	0.000
HD201891	4.31	−1.05	7.269	5947 ± 62	0.274 ± 0.006	7.908	7.390	7.081	6.737	6.254	5.993	5.935	0.000
HD202575	4.85	0.04	7.473	4750 ± 44	0.391 ± 0.007	8.917	7.897	7.295	6.796	6.066	5.527	5.391	0.000
HD202751	4.70	−0.10	7.760	4818 ± 38	0.333 ± 0.005	9.150	8.160	7.580	7.085	6.369	5.854	5.739	0.000
HD204155	4.03	−0.70	8.380	5881 ± 66	0.168 ± 0.004	9.068	8.495	—	—	7.360	7.032	7.011	0.000
HD211476	4.40	−0.24	6.948	5853 ± 51	0.328 ± 0.006	7.639	7.039	—	—	5.880	5.585	5.542	0.000
HD21197	4.59	0.27	7.310	4587 ± 60	0.452 ± 0.012	9.030	7.868	7.184	6.619	5.827	5.306	5.124	0.000
HD213042	4.58	0.19	7.199	4732 ± 59	0.447 ± 0.012	8.740	7.640	7.014	6.512	5.769	5.285	5.115	0.000
HD213657	3.90	−1.96	9.511	6299 ± 72	0.087 ± 0.002	10.063	9.646	9.368	9.068	8.672	8.406	8.346	0.002
HD214749	4.50	0.12	7.247	4559 ± 78	0.471 ± 0.016	8.940	7.810	7.125	6.560	5.773	5.261	5.039	0.000
HD215152	4.55	−0.17	7.744	4880 ± 54	0.327 ± 0.007	9.057	8.096	7.545	7.090	6.353	5.895	5.775	0.000
HD215257	4.26	−0.64	7.317	5947 ± 50	0.268 ± 0.005	7.926	7.421	—	—	6.309	6.021	5.951	0.000
HD21543	4.28	−0.53	8.113	5731 ± 64	0.200 ± 0.005	8.858	8.237	—	—	7.001	6.743	6.647	0.000
HD215500	4.40	−0.34	7.334	5491 ± 59	0.312 ± 0.007	8.197	7.480	7.078	6.709	6.135	5.798	5.732	0.000
HD215664	3.83	0.00	5.857	6918 ± 126	0.388 ± 0.015	6.195	5.849	—	—	5.098	5.074	4.977	0.000
HD215801	3.83	−2.28	9.871	6163 ± 77	0.077 ± 0.002	10.471	10.038	9.732	9.418	9.016	8.695	8.642	0.001
HD216259	4.81	−0.63	7.981	4958 ± 56	0.284 ± 0.007	9.136	8.294	7.791	7.350	6.615	6.182	6.076	0.000
HD216777	4.17	−0.53	7.909	5651 ± 73	0.226 ± 0.006	8.651	8.011	7.661	7.306	6.816	6.492	6.353	0.000
HD218502	3.96	−1.76	8.121	6298 ± 66	0.165 ± 0.004	8.676	8.256	7.976	7.676	7.265	7.020	6.972	0.000
HD219538	4.50	−0.04	7.812	5058 ± 58	0.295 ± 0.007	8.944	8.051	7.589	7.180	6.469	6.047	5.961	0.000
HD219617	3.83	−1.50	8.022	6136 ± 68	0.182 ± 0.004	8.621	8.153	7.845	7.525	7.082	6.860	6.771	0.001
HD220339	4.53	−0.31	7.508	5016 ± 57	0.345 ± 0.008	8.670	7.780	7.285	6.835	6.201	5.740	5.591	0.000
HD221239	4.56	−0.46	8.048	4962 ± 72	0.275 ± 0.008	9.231	8.331	7.855	7.415	6.660	6.256	6.145	0.000
HD221503	4.99	0.02	7.791	4270 ± 61	0.418 ± 0.012	9.887	8.601	7.806	7.131	6.236	5.607	5.473	0.000
HD222335	4.45	−0.16	6.991	5308 ± 65	0.391 ± 0.010	7.990	7.180	6.730	6.330	5.786	5.332	5.265	0.000
HD222589	4.00	0.02	8.534	5215 ± 84	0.199 ± 0.006	9.516	8.739	—	—	7.227	6.921	6.766	0.000
HD222766	4.00	−0.93	9.965	5517 ± 80	0.092 ± 0.003	10.802	10.124	9.734	9.354	8.867	8.502	8.353	0.000
HD224817	4.40	−0.55	8.298	5906 ± 63	0.173 ± 0.004	8.950	8.400	—	—	7.270	7.017	6.904	0.000
HD22502	4.50	0.00	9.683	6125 ± 94	0.085 ± 0.003	10.220	9.730	—	—	8.671	8.516	8.380	0.000
HD225023	4.00	0.00	7.533	7563 ± 115	0.150 ± 0.005	7.700	7.520	—	—	7.021	7.002	6.946	0.000
HD225261	4.59	−0.44	7.647	5299 ± 51	0.290 ± 0.006	8.578	7.826	7.405	7.025	6.398	6.027	5.932	0.000
HD22879	4.41	−0.91	6.569	5941 ± 72	0.379 ± 0.009	7.229	6.679	6.354	6.017	5.588	5.301	5.179	0.000
HD229274	4.50	−0.94	8.868	5352 ± 67	0.162 ± 0.004	9.700	9.085	—	—	7.622	7.288	7.213	0.000
HD230409	4.40	−1.00	9.895	5489 ± 59	0.096 ± 0.002	10.760	10.070	9.670	9.280	8.734	8.349	8.316	0.000
HD233511	4.32	−1.64	9.536	6157 ± 64	0.090 ± 0.002	10.170	9.710	9.406	9.099	8.617	8.386	8.329	0.008

HD237287	4.55	0.00	8.058	5052 ± 64	0.264 ± 0.007	9.235	8.332	—	—	6.702	6.319	6.201	0.000
HD241596	4.50	−1.01	9.239	4490 ± 58	0.194 ± 0.005	10.881	9.848	—	—	7.761	7.205	7.065	0.000
HD24289	3.75	−2.06	9.726	5927 ± 59	0.089 ± 0.002	10.477	9.960	9.620	9.250	8.778	8.454	8.399	0.015
HD24331	4.51	−0.31	8.292	4939 ± 45	0.248 ± 0.005	9.541	8.619	8.096	7.632	6.940	6.478	6.355	0.000
HD250792	4.33	−1.00	9.146	5562 ± 57	0.132 ± 0.003	9.931	9.312	—	—	8.001	7.695	7.583	0.000
HD25329	4.68	−1.80	8.159	4785 ± 62	0.281 ± 0.007	9.395	8.519	8.024	7.546	6.768	6.297	6.195	0.000
HD25665	4.51	−0.03	7.395	4906 ± 63	0.380 ± 0.010	8.630	7.757	7.190	6.747	5.989	5.539	5.457	0.000
HD25673	4.60	−0.53	9.282	5143 ± 105	0.145 ± 0.006	10.355	9.532	9.065	8.622	7.959	7.653	7.461	0.000
HD263175	4.67	−0.59	8.411	4825 ± 43	0.246 ± 0.005	9.770	8.810	8.240	7.750	7.021	6.524	6.417	0.000
HD26767	4.50	0.03	7.978	5798 ± 63	0.208 ± 0.005	8.699	8.060	7.703	7.366	6.856	6.607	6.534	0.000
HD26911	4.27	0.08	6.326	6693 ± 76	0.334 ± 0.008	6.729	6.329	6.088	5.868	5.514	5.401	5.326	0.000
HD27561	4.41	−0.14	6.587	6695 ± 81	0.296 ± 0.008	7.017	6.610	6.365	6.131	5.784	5.666	5.595	0.000
HD277559	4.50	−0.99	9.560	6338 ± 70	0.084 ± 0.002	10.080	9.660	—	—	8.702	8.441	8.421	0.000
HD27848	4.28	0.08	6.945	6541 ± 88	0.263 ± 0.008	7.409	6.958	6.691	6.441	6.059	5.935	5.892	0.000
HD28185	4.44	0.24	7.715	5687 ± 56	0.244 ± 0.005	8.550	7.800	—	—	6.578	6.289	6.185	0.000
HD284248	4.42	−1.56	9.007	6291 ± 61	0.110 ± 0.002	9.650	9.208	8.927	8.608	8.165	7.927	7.871	0.020
HD28462	4.55	0.06	8.886	5250 ± 45	0.167 ± 0.003	9.946	9.083	—	—	7.619	7.211	7.139	0.000
HD285805	4.46	−0.04	9.727	4534 ± 65	0.152 ± 0.005	11.487	10.320	—	—	8.224	7.689	7.515	0.000
HD28635	4.00	0.01	7.730	6124 ± 86	0.209 ± 0.006	8.316	7.777	7.465	7.165	6.733	6.572	6.455	0.000
HD28805	4.50	0.14	8.518	5534 ± 57	0.178 ± 0.004	9.399	8.657	8.244	7.874	7.323	7.017	6.941	0.000
HD28878	4.99	−0.06	9.160	5133 ± 53	0.154 ± 0.003	10.279	9.399	—	—	7.839	7.420	7.351	0.000
HD28946	4.55	−0.03	7.783	5313 ± 52	0.271 ± 0.005	8.704	7.940	7.548	7.148	6.524	6.159	6.070	0.000
HD28977	4.99	−0.04	9.400	5112 ± 55	0.139 ± 0.003	10.594	9.675	9.146	8.708	8.061	7.670	7.553	0.000
HD28992	4.50	0.06	7.831	5913 ± 83	0.214 ± 0.006	8.530	7.898	7.556	7.226	6.745	6.552	6.445	0.000
HD29159	4.60	0.09	9.170	5189 ± 57	0.150 ± 0.003	10.247	9.382	—	—	7.860	7.505	7.373	0.000
HD291763	4.50	−0.34	9.764	4938 ± 51	0.126 ± 0.003	10.920	10.070	—	—	8.423	7.944	7.801	0.000
HD298986	4.31	−1.34	9.943	6225 ± 68	0.073 ± 0.002	10.506	10.062	9.774	9.470	9.040	8.780	8.742	0.004
HD29907	4.60	−1.60	9.646	5532 ± 53	0.106 ± 0.002	10.473	9.837	—	—	8.512	8.192	8.090	0.000
HD30501	4.54	0.13	7.351	5156 ± 44	0.351 ± 0.006	8.460	7.580	7.100	6.675	6.059	5.642	5.525	0.000
HD31128	4.48	−1.54	8.993	6093 ± 68	0.118 ± 0.003	9.624	9.135	8.826	8.501	8.032	7.800	7.738	0.000
HD34328	4.50	−1.66	9.252	6056 ± 67	0.106 ± 0.002	9.903	9.416	9.106	8.773	8.316	8.046	7.998	0.000
HD345957	3.86	−1.46	8.735	5895 ± 58	0.142 ± 0.003	9.390	8.880	—	—	7.711	7.444	7.364	0.000
HD349063	4.00	−0.45	9.196	5650 ± 48	0.125 ± 0.002	9.976	9.331	—	—	8.075	7.741	7.690	0.000
HD3567	4.17	−1.17	9.105	6178 ± 65	0.109 ± 0.002	9.695	9.240	8.941	8.631	8.218	7.933	7.889	0.004
HD3628	4.10	−0.18	7.249	5828 ± 53	0.288 ± 0.006	7.967	7.337	—	—	6.192	5.896	5.806	0.000
HD3765	4.30	0.01	7.055	5010 ± 51	0.426 ± 0.009	8.300	7.360	6.820	6.380	5.694	5.272	5.164	0.000
HD37792	4.10	−0.60	7.639	6542 ± 82	0.191 ± 0.005	8.116	7.697	7.448	7.180	6.830	6.681	6.573	0.000
HD39715	4.75	−0.04	8.402	4768 ± 43	0.253 ± 0.005	9.840	8.830	8.225	7.730	6.992	6.466	6.352	0.000
HD4203	4.30	0.42	8.579	5617 ± 59	0.168 ± 0.004	9.444	8.687	—	—	7.389	7.115	7.047	0.000
HD4256	4.80	0.34	7.673	4983 ± 45	0.324 ± 0.006	8.980	7.990	7.430	6.970	6.306	5.868	5.741	0.000
HD4307	4.01	−0.25	6.054	5877 ± 83	0.491 ± 0.014	6.741	6.139	—	—	4.995	4.774	4.622	0.000
HD4308	4.31	−0.40	6.449	5774 ± 80	0.424 ± 0.012	7.210	6.560	6.187	5.835	5.366	5.101	4.945	0.000
HD45281	4.50	0.00	8.713	6099 ± 64	0.134 ± 0.003	9.240	8.770	—	—	7.721	7.461	7.413	0.000
HD45282	3.16	−1.45	7.802	5299 ± 87	0.270 ± 0.009	8.672	8.010	7.610	7.196	6.591	6.270	6.089	0.000
HD4747	4.48	−0.21	6.995	5422 ± 70	0.374 ± 0.010	7.945	7.155	6.735	6.335	5.813	5.433	5.305	0.000
HD51219	4.30	−0.09	7.298	5590 ± 55	0.306 ± 0.006	8.109	7.410	7.033	6.676	6.146	5.833	5.721	0.000
HD5133	4.50	−0.10	6.862	4961 ± 65	0.475 ± 0.013	8.120	7.180	6.640	6.180	5.537	5.049	4.894	0.000

HD53545	4.23	−0.29	8.010	6385 ± 75	0.169 ± 0.004	8.503	8.047	7.779	7.508	7.156	6.903	6.865	0.000
HD53927	4.66	−0.37	8.009	4884 ± 44	0.289 ± 0.005	9.240	8.351	7.822	7.372	6.645	6.137	6.057	0.000
HD57901	4.47	0.00	7.857	4868 ± 50	0.312 ± 0.007	9.186	8.224	7.660	7.208	6.456	5.976	5.886	0.000
HD59374	4.42	−0.88	8.373	5839 ± 54	0.171 ± 0.003	9.026	8.485	8.161	7.835	7.326	7.031	6.982	0.000
HD59392	3.87	−1.62	9.592	6045 ± 79	0.091 ± 0.002	10.217	9.761	9.457	9.142	8.633	8.403	8.338	0.006
HD59468	4.44	0.02	6.625	5619 ± 73	0.413 ± 0.011	7.420	6.720	6.343	5.988	5.515	5.154	5.042	0.000
HD59747	4.62	0.06	7.435	5065 ± 53	0.350 ± 0.008	8.572	7.695	7.202	6.786	6.090	5.662	5.589	0.000
HD60298	4.22	−0.07	7.263	5809 ± 54	0.288 ± 0.006	8.006	7.354	—	—	6.168	5.900	5.832	0.000
HD64090	4.61	−1.67	8.113	5465 ± 56	0.220 ± 0.005	8.951	8.295	7.935	7.536	6.956	6.611	6.537	0.000
HD64606	4.24	−0.92	7.197	5203 ± 60	0.370 ± 0.009	8.140	7.412	6.994	6.561	5.972	5.498	5.425	0.000
HD65486	4.50	−0.24	7.930	4683 ± 35	0.326 ± 0.005	9.450	8.400	7.795	7.265	6.506	5.944	5.833	0.000
HD65583	4.67	−0.70	6.784	5315 ± 52	0.429 ± 0.009	7.707	6.994	—	—	5.539	5.170	5.095	0.000
HD67199	4.53	0.03	6.941	5156 ± 47	0.424 ± 0.008	8.055	7.166	6.686	6.270	5.647	5.234	5.115	0.000
HD68017	4.46	−0.43	6.664	5521 ± 55	0.420 ± 0.009	7.504	6.822	—	—	5.477	5.152	5.090	0.000
HD73524	4.41	0.12	6.483	5981 ± 65	0.389 ± 0.009	7.130	6.530	6.200	5.890	5.462	5.210	5.103	0.000
HD74000	4.10	−2.01	9.493	6361 ± 98	0.086 ± 0.003	10.071	9.656	9.381	9.080	8.716	8.400	8.390	0.003
HD78429	4.33	0.09	7.219	5740 ± 54	0.301 ± 0.006	7.978	7.306	6.937	6.594	6.113	5.809	5.734	0.000
HD80218	4.16	−0.28	6.562	6114 ± 64	0.359 ± 0.008	7.110	6.640	—	—	5.571	5.342	5.306	0.000
HD80606	4.45	0.41	8.930	5502 ± 50	0.149 ± 0.003	9.820	9.060	—	—	7.702	7.400	7.316	0.000
HD82516	4.46	0.01	8.242	5100 ± 66	0.238 ± 0.006	9.412	8.502	8.006	7.566	6.922	6.539	6.386	0.000
HD84937	3.93	−2.11	8.154	6408 ± 66	0.157 ± 0.004	8.702	8.306	8.047	7.759	7.359	7.121	7.062	0.005
HD85091	3.93	−0.43	7.483	5561 ± 65	0.284 ± 0.007	8.232	7.628	—	—	6.334	6.021	5.878	0.000
HD85512	4.71	−0.18	7.007	4423 ± 126	0.559 ± 0.032	8.860	7.670	6.950	6.328	5.451	4.998	4.717	0.000
HD8638	4.38	−0.50	8.156	5578 ± 58	0.207 ± 0.004	8.990	8.300	7.915	7.550	7.003	6.675	6.617	0.000
HD87007	4.40	0.27	8.624	5270 ± 49	0.187 ± 0.004	9.623	8.802	8.357	7.966	7.354	6.971	6.886	0.000
HD88725	4.37	−0.64	7.633	5737 ± 52	0.249 ± 0.005	8.358	7.753	—	—	6.543	6.242	6.153	0.000
HD89813	4.51	−0.17	7.612	5379 ± 53	0.286 ± 0.006	8.553	7.769	7.346	6.963	6.399	6.032	5.911	0.000
HD90508	4.35	−0.33	6.319	5743 ± 70	0.455 ± 0.012	7.049	6.445	—	—	5.195	4.895	4.874	0.000
HD90663	4.63	−0.29	8.203	4943 ± 41	0.258 ± 0.004	9.450	8.530	7.989	7.550	6.851	6.386	6.265	0.000
HD92786	4.64	−0.29	7.835	5309 ± 60	0.265 ± 0.006	8.770	8.020	7.593	7.208	6.572	6.227	6.133	0.000
HD92788	4.42	0.28	7.229	5717 ± 64	0.302 ± 0.007	8.000	7.310	—	—	6.131	5.798	5.721	0.000
HD94028	4.36	−1.44	8.064	6110 ± 66	0.180 ± 0.004	8.640	8.202	7.917	7.585	7.130	6.854	6.832	0.000
HD9562	4.02	0.19	5.704	5876 ± 71	0.577 ± 0.015	6.397	5.757	5.407	5.087	4.627	4.391	4.258	0.000
HD97320	4.23	−1.28	8.047	6134 ± 55	0.180 ± 0.004	8.642	8.161	7.866	7.554	7.137	6.868	6.790	0.000
HD97916	4.02	−0.94	9.126	6451 ± 69	0.099 ± 0.002	9.628	9.211	—	—	8.319	8.104	8.018	0.000
HD98281	4.61	−0.20	7.123	5426 ± 56	0.352 ± 0.008	8.022	7.275	6.862	6.487	5.914	5.575	5.457	0.000
HD99109	4.32	0.38	8.912	5266 ± 46	0.164 ± 0.003	9.970	9.100	—	—	7.626	7.259	7.162	0.000
HD99747	4.12	−0.50	5.799	6621 ± 76	0.435 ± 0.011	6.221	5.857	—	—	4.997	4.825	4.797	0.000
HE0024-2523	4.30	−2.67	14.791	6583 ± 99	0.007 ± 0.001	15.321	14.913	—	—	14.038	13.748	13.749	0.006
HE0130-2303	4.60	−2.90	14.497	6590 ± 134	0.008 ± 0.001	15.141	14.760	14.505	14.207	13.895	13.550	13.589	0.004
HE0131-2740	3.03	−3.08	14.412	5487 ± 61	0.012 ± 0.001	15.214	14.630	14.240	13.836	13.246	12.865	12.788	0.013
HE0148-2611	4.30	−3.00	14.238	6595 ± 91	0.009 ± 0.001	14.824	14.453	—	—	13.559	13.298	13.303	0.004
HE0218-2738	4.30	−3.52	14.792	6581 ± 81	0.007 ± 0.001	15.277	14.883	—	—	13.968	13.762	13.699	0.004
HE0233-0343	4.00	−4.30	15.337	6270 ± 80	0.006 ± 0.001	15.867	15.430	15.171	14.818	14.359	14.077	14.063	0.025
HE1148-0037	3.70	−3.46	13.446	6345 ± 74	0.014 ± 0.001	14.018	13.614	—	—	12.610	12.318	12.272	0.022
HE1327-2326	3.70	−5.00	13.090	6250 ± 60	0.017 ± 0.001	14.016	13.535	13.211	12.854	12.357	12.068	11.986	0.076
HE2133-1426	4.10	−2.80	15.345	6259 ± 97	0.006 ± 0.001	15.935	15.486	15.191	14.845	14.380	14.139	14.111	0.028

LP635-14	4.03	−2.48	10.994	6520 ± 70	0.041 ± 0.001	11.760	11.330	11.050	10.740	10.285	10.041	9.997	0.060
LP815-43	4.19	−2.80	10.688	6535 ± 68	0.047 ± 0.001	11.290	10.910	10.650	10.350	9.964	9.709	9.650	0.024
LP831-70	4.38	−2.93	11.413	6408 ± 67	0.035 ± 0.001	12.020	11.620	11.350	11.040	10.654	10.379	10.344	0.005

[a] Sample stars used and derived fundamental physical parameters via IRFM. Apparent bolometric magnitudes (m_{Bol}) have been computed according to Casagrande et al. (2006), where the absolute bolometric magnitude of the Sun $M_{Bol,\odot} = 4.74$. For each star m_{Bol} is obtained using its bolometric flux and effective temperature and therefore it is already corrected for reddening, if present. Notice however that the observed magnitudes given here are not: before computing bolometric corrections, the observed magnitudes should be corrected using the corresponding $E(B-V)$ given here. Errors have been computed as described in the text, without accounting for the uncertainty in $E(B-V)$: changing it by ±0.01 would affect $T_{\rm eff}$ by approximately ±50 K.